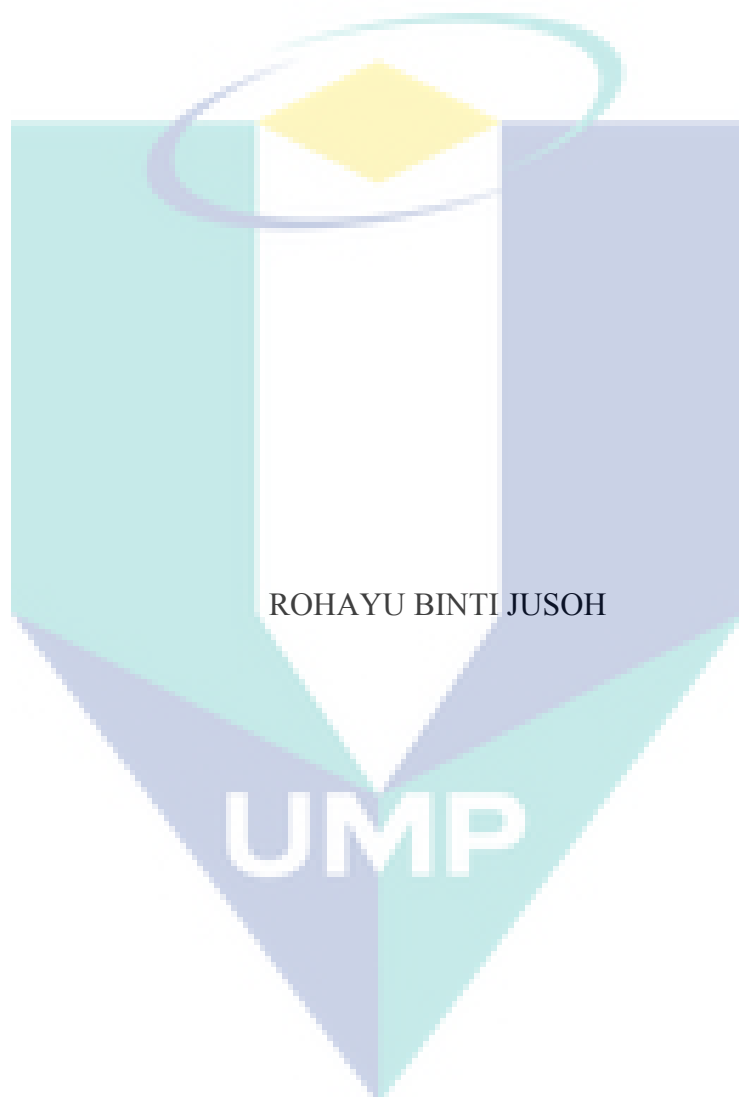


MESOSTRUCTURED SILICA NANOPARTICLES SUPPORTED
ELECTROSYNTHESIZED GOETHITE IN CATIONIC SURFACTANT FOR
PHOTODEGRADATION OF 2-CHLOROPHENOL



UNIVERSITI TEKNOLOGI MALAYSIA

DECLARATION OF THESIS / UNDERGRADUATE PROJECT PAPER AND COPYRIGHT

Author's full name : ROHAYU BINTI JUSOH

Date of birth : 3rd DECEMBER 1989

Title : MESOSTRUCTURED SILICA NANOPARTICLES SUPPORTED
ELECTROSYNTHESIZED GOETHITE IN CATIONIC SURFACTANT
FOR PHOTODEGRADATION OF 2-CHLOROPHENOL

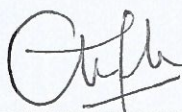
Academic Session: 2014/2015(2)

I declare that this thesis is classified as :

- CONFIDENTIAL** [Contains confidential information under the Official Secret Act 1972]*
- RESTRICTED** [Contains restricted information as specified by the organization where research was done]*
- OPEN ACCESS** I agree that my thesis to be published as online open access (full text)

I acknowledged that Universiti Teknologi Malaysia reserves the right as follows:

1. The thesis is the property of Universiti Teknologi Malaysia.
2. The Library of Universiti Teknologi Malaysia has the right to make copies for the purpose of research only.
3. The Library has the right to make copies of the thesis for academic exchange.



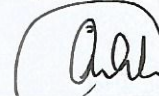
SIGNATURE

891203-06-5114

(NEW IC NO. /PASSPORT NO.)

Date : 25th MAY 2015

Certified by :



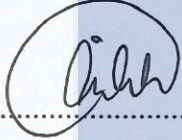
SIGNATURE OF SUPERVISOR

ASSOC PROF DR AISHAH ABDUL JALIL
NAME OF SUPERVISOR

Date : 25th MAY 2015

NOTES : * If the thesis is CONFIDENTIAL or RESTRICTED, please attach with the letter from the organization with period and reasons for confidentiality or restriction.

“We hereby declare that we have read this thesis and in our opinion this thesis is sufficient in terms of scope and quality for the award of the degree of Doctor of Philosophy (Chemical Engineering)”

Signature : 

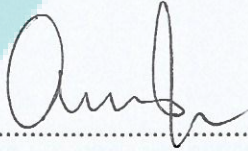
Name of Supervisor I : Assoc. Prof. Dr Aishah Abdul Jalil

Date : 25th May 2015

Signature : 

Name of Supervisor II : Prof. Dr Sugeng Triwahyono

Date : 25th May 2015

Signature : 

Name of Supervisor III : Prof. Dr Ani Idris

Date : 25th May 2015

BAHAGIAN A – Pengesahan Kerjasama*

Adalah disahkan bahawa projek penyelidikan tesis ini telah dilaksanakan melalui kerjasama antara _____ dengan _____

Disahkan oleh:

Tandatangan : Tarikh :

Nama :

Jawatan :
(Cop rasmi)

** Jika penyediaan tesis/projek melibatkan kerjasama.*

BAHAGIAN B – Untuk Kegunaan Pejabat Sekolah Pengajian Siswazah

Tesis ini telah diperiksa dan diakui oleh:

Nama dan Alamat Pemeriksa Luar : Prof. Dr. Bassim H. Hameed
School of Chemical Engineering,
University of Science Malaysia,
14300 Nibong Tebal
Penang,
Pulau Pinang.

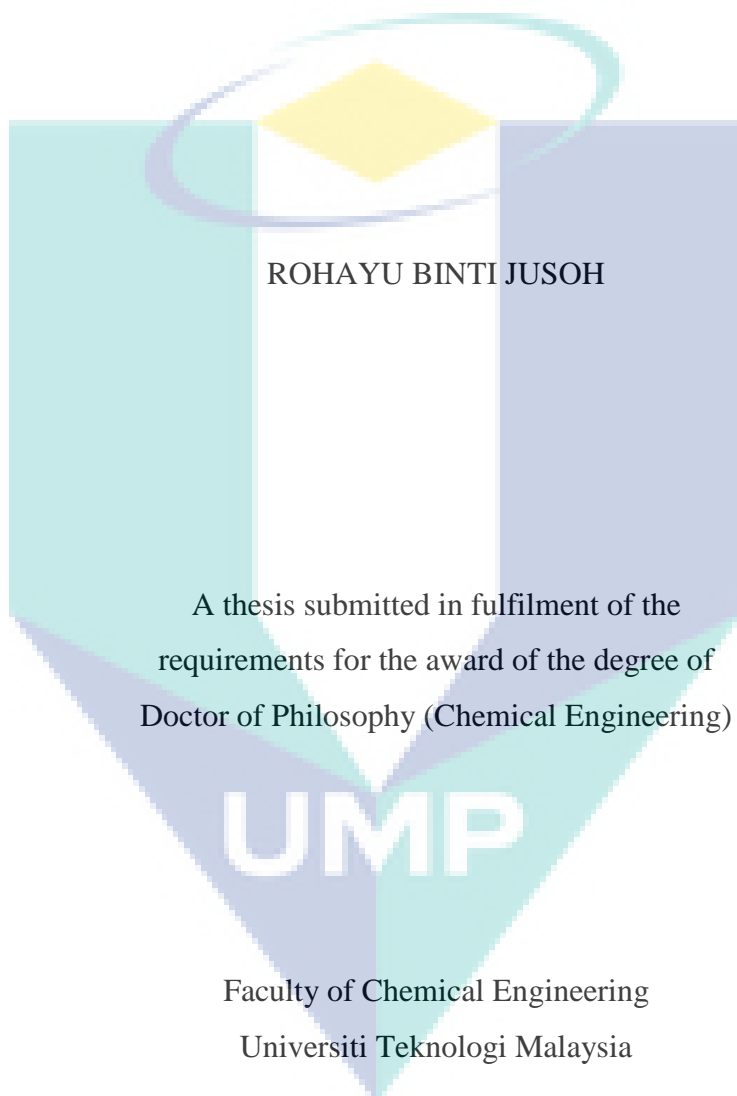
Nama dan Alamat Pemeriksa Dalam : Prof. Dr. Mustaffa bin Shamsuddin
Faculty of Science,
UTM Johor Bahru

Disahkan oleh Timbalan Pendaftar di Sekolah Pengajian Siswazah:

Tandatangan : Tarikh :

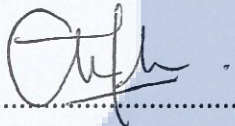
Nama : ASRAM BIN SULAIMAN @ SAIM
.....

MESOSTRUCTURED SILICA NANOPARTICLES SUPPORTED
ELECTROSYNTHESIZED GOETHITE IN CATIONIC SURFACTANT FOR
PHOTODEGRADATION OF 2-CHLOROPHENOL



MAY 2015

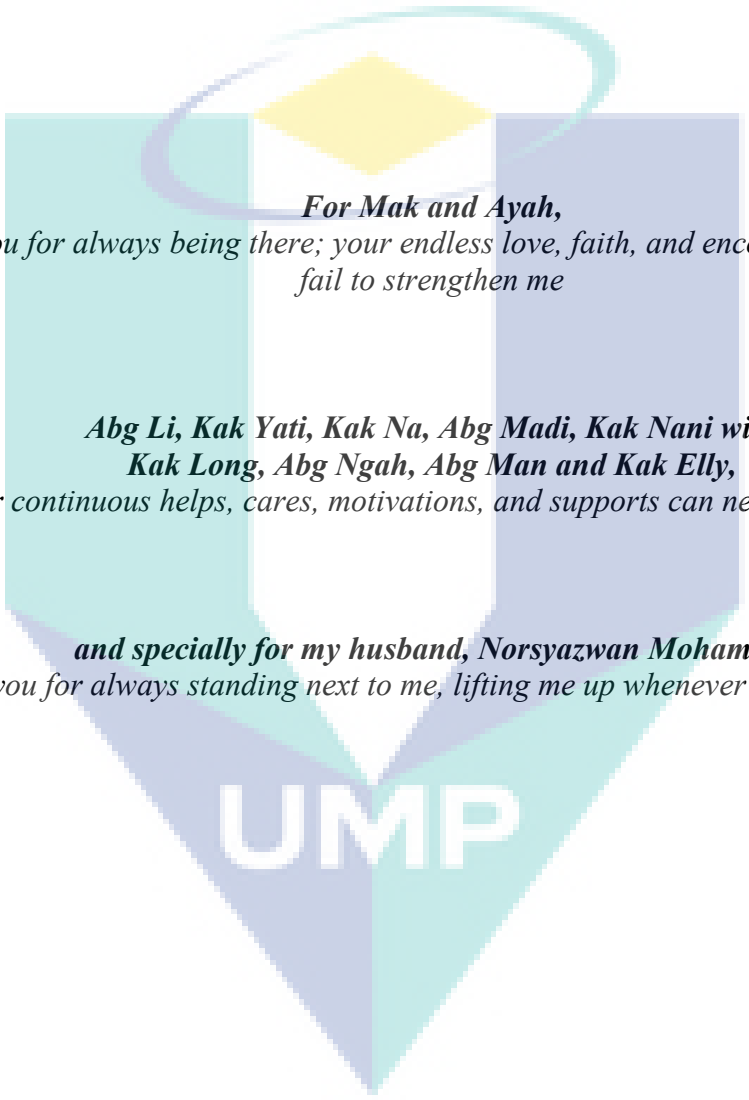
I declare that this report entitled "*Mesostructured Silica Nanoparticles Supported Electrosynthesized Goethite in Cationic Surfactant for Photodegradation of 2-Chlorophenol*" is the result of my own research except as cited in the references. The report has not been accepted for any degree and is not concurrently submitted in candidature of any other degree.

Signature : 

Name : ROHAYU BINTI JUSOH

Date : 25th May 2015

UMP



For Mak and Ayah,
Thank you for always being there; your endless love, faith, and encouragement never fail to strengthen me

***Abg Li, Kak Yati, Kak Na, Abg Madi, Kak Nani with
Kak Long, Abg Ngah, Abg Man and Kak Elly,***
Your continuous helps, cares, motivations, and supports can never be repaid

and specially for my husband, Norsyazwan Mohamed,
Thank you for always standing next to me, lifting me up whenever I couldn't reach

ACKNOWLEDGEMENT

Alhamdulillah, all praise to Allah. Peace and blessing to Prophet Muhammad S.A.W, his families and all muslims. Endless thanks and gratefulness to my supervisors; Assoc. Prof. Dr. Aishah Abdul Jalil, Prof. Dr. Sugeng Triwahyono and Prof. Dr. Ani Idris for the never ending advises and helps during the study. Their patience, criticism and ideas throughout this study are greatly appreciated. Without their continuous support, this thesis would not be completely finished.

A million thanks and appreciation goes to all the Green Technology and Advanced Materials research group members for giving me a helping hand in the process of doing this research. A lot of appreciation also goes to the staffs of Chemical Reaction Engineering Laboratory at Faculty of Chemical Engineering and Ibnu Sina Institute for their valuable help and aiding me in technical works throughout this study. My appreciation also goes to Yang di-Pertuan Agong for the King's Scholarship Award and Universiti Malaysia Pahang (UMP) for Fellowship Scheme that were financially helpful in finishing this study.

Last but not least, I would like to extend my deepest gratitude and appreciation to my family and my close friends for their continuous support and endless attention. Thank you for everything.

ABSTRACT

2-chlorophenol (2-CP) which had been widely used in industry and daily life is a priority toxic pollutant that has caused considerable damage to the aquatic ecosystem and human health. Due to this reason, continuing study on efficient catalyst for degradation of this recalcitrant pollutant has been conducted in these recent years. In this study, goethite (α -FeOOH) was synthesized by an electrochemical method in a cationic surfactant solution and subsequent impregnation with mesostructured silica nanoparticles (MSN) gave α -FeOOH/MSN. The catalysts were characterized using X-ray diffraction (XRD), transmission electron microscopy (TEM), Fourier transform-infrared (FT-IR), ^{29}Si magnetic angle spin nuclear magnetic resonance (^{29}Si MAS NMR), nitrogen physisorption analysis, electron spin resonance (ESR), and X-ray photoelectron spectroscopy (XPS). The results indicate that the cationic surfactant was retained around α -FeOOH surface with a free swinging alkane tail pointing outward from the catalyst. The performance of the catalysts were tested on the photodegradation of the 2-CP in a batch reactor under visible light irradiation. The results showed that the α -FeOOH were able to inhibit electron-hole recombination to give complete degradation of 50 mg L^{-1} 2-CP at pH 5 when using 0.03 g L^{-1} catalyst and 0.156 mM of H_2O_2 . In contrast, it was found that by introducing the α -FeOOH to the MSN support, sequential silica removal in the MSN framework and isomorphous substitution of Fe ion was occurred, which able to effectively degrade the 2-CP with degradation percentage of 92.2, 79.3, 73.1, and 14.2%, with the loading of α -FeOOH in the following order: $10 \text{ wt\%} > 15 \text{ wt\%} > 5 \text{ wt\%} > \text{MSN}$, respectively. Beside the retainment of the cationic surfactant structure on the catalysts, the MSN was also elucidated to play an important role as an electron acceptor that enhanced the electron-hole separation. Response surface methodology (RSM) analysis for the α -FeOOH and α -FeOOH/MSN catalysts showed good significance of model with low probability values (<0.0001) and a high coefficient of determination (R^2). The kinetic studies of both catalysts illustrated that surface reaction was the controlling step of the process. Reusability study showed that both catalysts were still stable after more than 4 subsequent reactions. The upscaling study using 10-fold upscale system indicate superior performance of the catalysts with almost complete degradation of 2-CP. The employment of the catalysts on degradation of various pollutants such as phenol, cationic dye and anionic dye has also showed remarkable performance, suggesting the potential use of the catalysts for various applications. Significantly, the synthesis method of these catalysts could be a great advantage in the future development of nanotechnology.

ABSTRAK

2-klorofenol (2-CP) yang telah digunakan secara meluas dalam industri dan kehidupan seharian adalah pencemar toksik utama yang telah menyebabkan kerosakan besar kepada ekosistem akuatik dan kesihatan manusia. Oleh itu, kajian berterusan mengenai pemangkin yang berkesan untuk penurunan pencemar tegar ini telah dijalankan pada tahun-tahun kebelakangan ini. Dalam kajian ini, goethite (α -FeOOH) telah disintesis oleh kaedah elektrokimia dalam larutan surfaktan kationik dan penyahtepuan seterusnya dengan nanopartikel silika meso-struktur (MSN) memberi α -FeOOH/MSN. Pemangkin tersebut telah dicirikan menggunakan pembelauan sinar-X (XRD), mikroskopi transmisi elektron (TEM), spektroskopi inframerah transformasi Fourier (FT-IR), ^{29}Si putaran sudut ajaib resonans magnet nuklear (MAS ^{29}Si NMR), analisis penjerapan nitrogen, resonans elektron spin (ESR), dan spektroskopi fotoelektron sinar-X (XPS). Keputusan menunjukkan bahawa surfaktan kationik dikekalkan di seluruh permukaan α -FeOOH dengan ekor alkana berayun bebas menunjuk ke luar pemangkin. Prestasi pemangkin diuji dengan penurunan 2-CP dalam reaktor kelompok di bawah sinaran cahaya tampak. Hasil kajian menunjukkan bahawa α -FeOOH dapat menghalang penggabungan semula elektron-lubang untuk memberi penurunan lengkap 50 mg L^{-1} 2-CP pada pH 5 apabila menggunakan 0.03 g L^{-1} pemangkin dan $0.156 \text{ mM H}_2\text{O}_2$. Sebaliknya, telah ditemui bahawa dengan memperkenalkan α -FeOOH itu kepada sokongan MSN, penyingkiran silika berurutan dalam rangka kerja MSN dan penukargantian isomorf ion Fe telah berlaku, yang berkesan menurunkan 2-CP dengan peratusan penurunan 92.2, 79.3, 73.1 dan 14.2%, dengan pemuatan α -FeOOH mengikut susunan yang berikut: 10% berat > 15% berat > 5% berat > MSN, masing-masing. Selain pengekaln struktur surfaktan kationik pada pemangkin, MSN juga memainkan peranan penting sebagai penerima elektron yang meningkatkan pemisahan elektron-lubang. Analisis kaedah permukaan respon (RSM) untuk α -FeOOH dan α -FeOOH/MSN menunjukkan penemuan baik dengan nilai kebarangkalian yang rendah (<0.0001) dan pekali penentu yang tinggi (R^2). Kajian kinetik kedua-dua pemangkin menunjukkan bahawa tindak balas permukaan adalah langkah kawalan proses. Kajian kebolegunaan semula menunjukkan bahawa kedua-dua pemangkin masih stabil selepas lebih dari 4 tindak balas. Kajian penskalaan menggunakan sistem 10 kali ganda menunjukkan prestasi yang membanggakan daripada pemangkin dengan penurunan 2-CP yang hampir lengkap. Penggunaan pemangkin dalam penurunan pelbagai bahan pencemar seperti fenol, pewarna kationik dan pewarna anionik juga telah menunjukkan prestasi luar biasa, menunjukkan potensi penggunaan pemangkin untuk pelbagai aplikasi. Nyata, kaedah sintesis pemangkin ini boleh menjadi satu kelebihan yang besar dalam pembangunan masa depan teknologi nano.

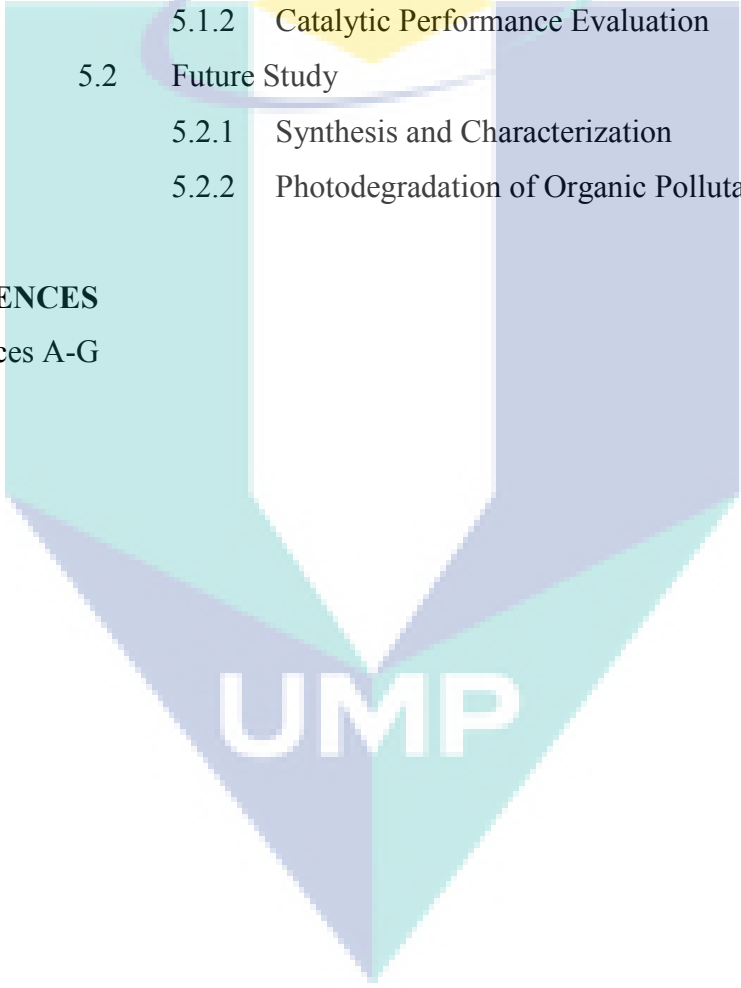
TABLE OF CONTENTS

CHAPTER	TITLE	PAGE
	DECLARATION	ii
	DEDICATION	iii
	ACKNOWLEDGEMENT	iv
	ABSTRACT	v
	ABSTRAK	vi
	TABLE OF CONTENTS	vii
	LIST OF TABLES	xi
	LIST OF FIGURES	xiii
	LIST OF ABBREVIATIONS	xix
	LIST OF SYMBOLS	xxi
	LIST OF APPENDICES	xxii
1	INTRODUCTION	1
	1.1 Research Background	1
	1.2 Problem Statement and Hypothesis	5
	1.3 Objective of the Study	7
	1.4 Scope of the Study	8
	1.5 Significance of Study	10
	1.6 Thesis Outline	11
2	LITERATURE REVIEW	12
	2.1 Introduction	12

2.2	Phenolic Compound	13
2.2.1	Chlorophenol	16
2.2.2	2-chlorophenol (2-CP)	17
2.3	Degradation Method	18
2.3.1	Biological Method	18
2.3.2	Physical Method	19
2.3.3	Chemical Method	20
2.4	Advanced Oxidation Process	21
2.4.1	Fenton Degradation	23
2.4.2	Fenton-like Degradation	24
2.4.3	Photocatalytic Degradation	25
2.4.4	Photo-Fenton-like Degradation	25
2.4.5	Optimization of Process Conditions	27
2.4.6	Kinetic Analysis	29
2.4.7	Mechanism of 2-CP Photodegradation	30
2.4.8	Scaling Up System	32
2.5	Photocatalyst Synthesis and Modification	33
2.5.1	α -FeOOH as Photocatalyst	34
2.5.2	Preparation of α -FeOOH	36
2.5.3	Electrolysis as Preparation Method	36
2.5.4	Cationic Surfactant as Electrolyte	38
2.5.5	Mesostructured Silica Nanoparticles as Support Material	40
2.6	Summary	41
3	METHODOLOGY	43
3.1	Introduction	43
3.2	Materials	45
3.3	Catalyst Preparation	45
3.3.1	Preparation of Mesoporous Silica Nanoparticles (MSN)	46
3.3.2	Preparation of α -FeOOH	46
3.3.3	Preparation of α -FeOOH/MSN	47

3.4	Catalyst Characterization	48
3.4.1	Crystallinity, Phase and Structural Studies	48
3.4.2	Morphological Properties	49
3.4.3	Vibrational Spectroscopy	49
3.4.4	Study of Textural Properties	49
3.4.5	Chemical Environment Determination	50
3.4.6	Chemical Oxidation State Determination	50
3.5	Catalytic Activity	51
3.5.1	Preparation of 2-CP Solution	51
3.5.2	Photoreactor System	51
3.5.3	Photodegradation Activity	52
3.6	Optimization of Process Conditions	53
3.7	Scale-up Process	60
4	RESULTS AND DISCUSSION	61
4.1	Introduction	61
4.2	Synthesis and Characterization	62
4.2.1	Crystallinity, Phase and Structural Studies	62
4.2.2	Morphological Properties	65
4.2.3	Vibrational Spectroscopy	68
4.2.4	Study of Textural Properties	78
4.2.5	Chemical Environment Determination	81
4.2.6	Chemical Oxidation State Determination	82
4.2.7	Proposed Structure of Photocatalysts	85
4.3	Photodegradation Performance Evaluations	87
4.3.1	Performance of Photocatalyst	88
4.3.2	Effect of Metal Loading	91
4.3.3	Effect of pH	94
4.3.4	Effect of H ₂ O ₂ Concentration	96
4.3.5	Effect of Catalyst Dosage	98
4.3.6	Effect of Initial Concentration	100
4.3.7	Effect of Reaction Temperature	102
4.3.8	Proposed Photodegradation Mechanism	105

4.4	Response Surface Methodology	112
4.5	Kinetic Analysis	129
4.6	Reusability Study	134
4.7	Scaling Up System	137
4.8	Application to Various Pollutant	139
5	CONCLUSION	141
5.1	Result Summary	141
5.1.1	Synthesis and Characterization	141
5.1.2	Catalytic Performance Evaluation	142
5.2	Future Study	143
5.2.1	Synthesis and Characterization	143
5.2.2	Photodegradation of Organic Pollutants	144
	REFERENCES	145
	Appendices A-G	164-170

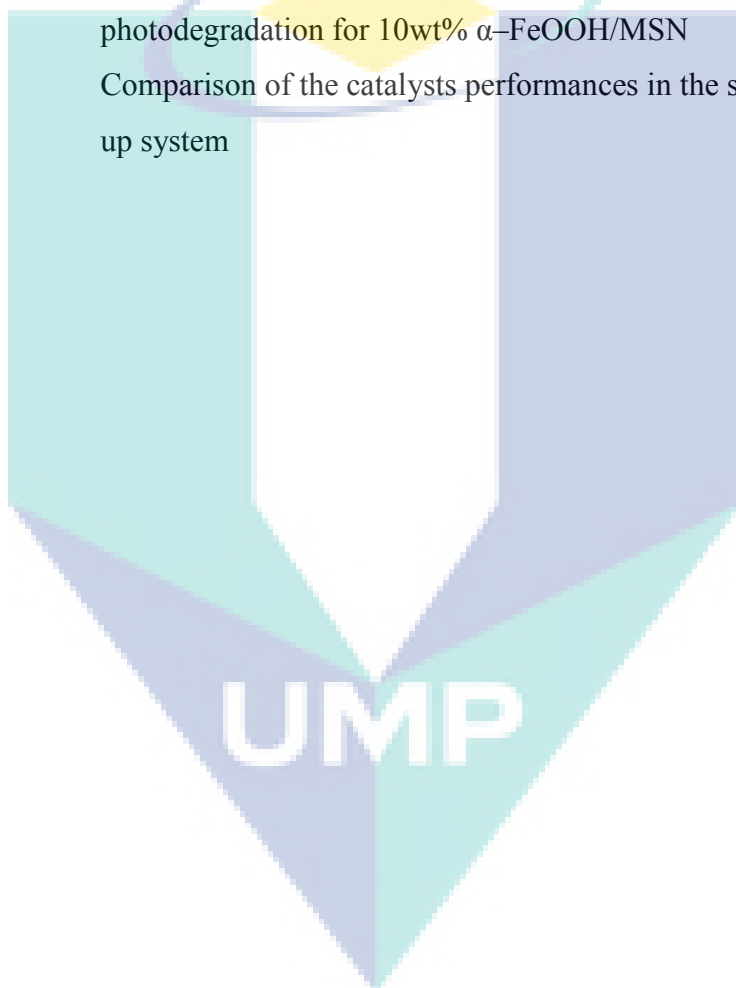
The logo for UMP (Universiti Malaysia Perlis) is a large, downward-pointing arrow shape. It is composed of several overlapping geometric shapes in shades of teal and light blue. The letters 'UMP' are printed in a bold, white, sans-serif font across the bottom of the arrow.

UMP

LIST OF TABLES

TABLE NO.	TITLE	PAGE
2.1	Previous studies for 2-CP degradation using α -FeOOH	35
3.1	List of chemicals	45
3.2	Variables showing operating conditions used in two-level factorial design employing α -FeOOH photocatalyst	54
3.3	Variables showing operating conditions used in two-level factorial design employing α -FeOOH/MSN photocatalyst	54
3.4	Two-level factorial design of experiments of four variables employing α -FeOOH photocatalyst	55
3.5	Two-level factorial design of experiments using α -FeOOH/MSN catalyst	55
3.6	Central composite design (CCD) design of experiments employing α -FeOOH photocatalyst	57
3.7	Central composite design (CCD) design of experiments employing α -FeOOH/MSN photocatalyst	58
4.1	Textural properties of catalysts	81
4.2	Calculated band gap value for each catalyst	94
4.3	Response for two-level factorial of four variables (X_1 - X_4)	112
4.4	Response for central composite design (CCD)	114
4.5	ANOVA of photodegradation of 2-CP by α -FeOOH	115
4.6	Response for two-level factorial of five variables	119
4.7	Central composite design of experiments of four	

	variables	1121
4.8	Analysis of variance (ANOVA) for central composite design for α -FeOOH /MSN catalyst	123
4.9	Analysis of variance (ANOVA) for central composite design for α -FeOOH /MSN catalyst (reduced)	124
4.10	Confirmation experiments	129
4.11	Pseudo-first order apparent constant values for 2-CP photodegradation for α -FeOOH	130
4.12	Pseudo-first order apparent constant values for 2-CP photodegradation for 10wt% α -FeOOH/MSN	132
4.13	Comparison of the catalysts performances in the scale-up system	138



LIST OF FIGURES

FIGURE NO.	TITLE	PAGE
2.1	Phenolic compounds considered priority pollutants by US EPA and EU	15
2.2	Interaction between variable X_1 and X_2 over the response	28
2.3	A mechanism to account for the pathways of photoproducts in the course of mineralisation of 2-CP (Bandara <i>et al.</i> , 2001a)	31
2.4	Illustration of heterogeneous photocatalytic processes on the semiconductor (Litter, 1999).	33
2.5	Illustration of surfactant showing hydrophilic (head) and hydrophobic (tail) components	38
3.1	Flow chart of the research activity	44
3.2	Schematic diagram of electrolysis cell	47
3.3	Schematic diagram of laboratory scale photoreactor	52
3.4	Schematic diagram of pilot scale photoreactor	60
4.1	XRD patterns of α -FeOOH nanoparticles	63
4.2	XRD patterns in region $2-10^\circ$ of MSN and α -FeOOH/MSN catalysts at different α -FeOOH loading	64
4.3	XRD patterns in region $2-10^\circ$ of MSN _{APTES} and α -FeOOH/MSN _{APTES} catalysts as compared to its pristine catalysts	65
4.4	(A) and (B) TEM image of α -FeOOH nanoparticles; (C) HRTEM image and the FFT image (as inset)	66

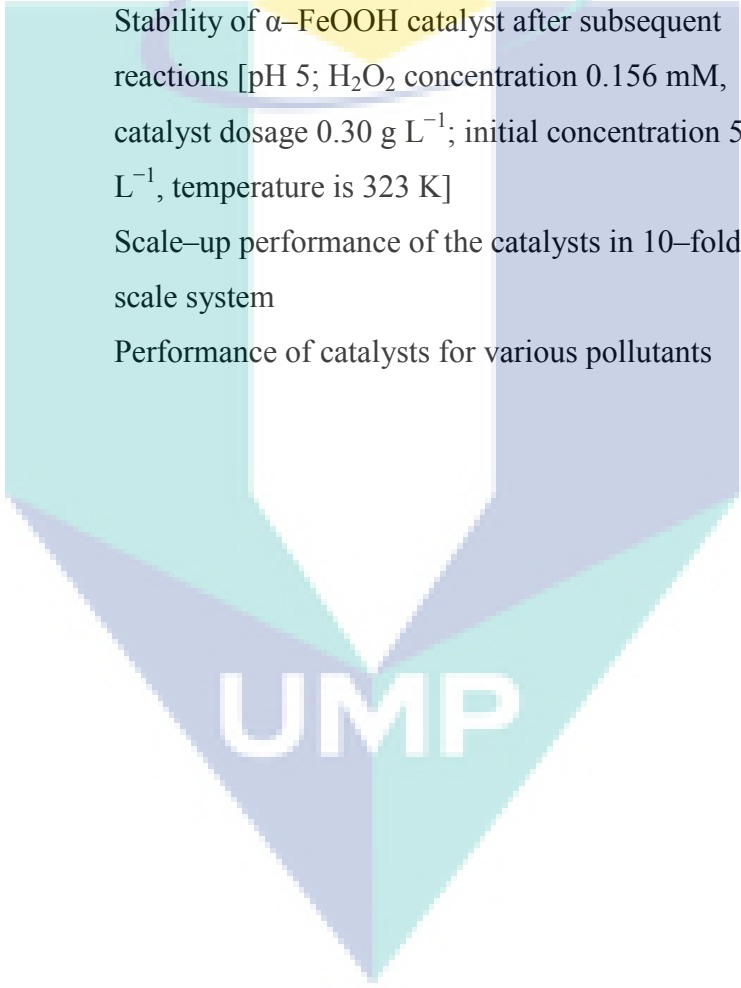
4.5	TEM image of (A) MSN; (B and C) 10 wt% α -FeOOH /MSN; (D) HRTEM image of 10 wt% α -FeOOH /MSN	68
4.6	FT-IR spectra of (a) ionic surfactant, (b) α -FeOOH, (c) P-FeOOH, and (d) C-FeOOH. (A) Region 3800–2700 cm^{-1} ; (B) region 1800–1400 cm^{-1} ; (C) region 1100–400 cm^{-1}	70
4.7	FT-IR spectra of α -FeOOH in evacuated system at (a) 303 K, (b) 313 K, and (c) 323 K. (A) Region 3900–2700 cm^{-1} ; (B) region 1800–900 cm^{-1}	70
4.8	FT-IR spectra of catalysts. (A) Region 3800–2700 cm^{-1} ; (B) region 1800–1360 cm^{-1} ; (C) region 1300–400 cm^{-1} ; (D) in evacuated system for region 3770–3700 cm^{-1}	72
4.9	FT-IR spectra of (A) MSN, (B) 5wt% α -FeOOH /MSN, (C) 10wt% α -FeOOH /MSN and (D) 15wt% α -FeOOH /MSN and Gaussian curve-fitting of band at 960 cm^{-1}	76
4.10	FT-IR spectra of catalysts. (a) MSN; (b) MSN _{APTES} ; (c) α -FeOOH/MSN; (d) α -FeOOH/MSN _{APTES}	77
4.11	(A) N ₂ adsorption-desorption isotherm; (B) pore size distributions of the catalysts	79
4.12	Pore distribution of catalysts	80
4.13	²⁹ Si MAS NMR spectra of (a) MSN and (b) 10wt% α -FeOOH/MSN	82
4.14	ESR spectra of (a) 5wt% α -FeOOH/MSN, (b) 10wt% α -FeOOH/MSN, (c) 15wt% α -FeOOH/MSN, and (d) α -FeOOH	83
4.15	XPS spectra of (B) Fe _{2p} and (C) Si _{2p} for 10 wt% α -FeOOH/MSN catalyst	84
4.16	The proposed reaction pathways for electrosynthesis of α -FeOOH	86
4.17	Proposed structure of α -FeOOH/MSN	87

- 4.18 The performance of catalysts under light irradiation for photocatalysis of α -FeOOH, photo-Fenton-like reaction of C-FeOOH, P-FeOOH, and α -FeOOH catalysts [pH 5; H₂O₂ concentration 0.156 mM; catalyst dosage 0.30 g L⁻¹; initial concentration 50 mg L⁻¹; temperature 303K]. 89
- 4.19 Effects of cationic surfactant on the photo-Fenton-like activity [pH 5; H₂O₂ concentration 0.156 mM; catalyst dosage 0.30 g L⁻¹; initial concentration 50 mg L⁻¹; temperature 303K]. 90
- 4.20 The 2-CP photodegradation performance of the catalysts [pH 5; H₂O₂ concentration 0.156 mM; catalyst dosage 0.30 g L⁻¹; initial concentration 50 mg L⁻¹; temperature 303K]. 91
- 4.21 The 2-CP photodegradation performance of the catalysts [pH 5; H₂O₂ concentration 0.156 mM; catalyst dosage 0.30 g L⁻¹; initial concentration 50 mg L⁻¹; temperature 303K]. 92
- 4.22 Photoluminescence spectra for α -FeOOH/MSN catalysts 93
- 4.23 Influence of pH on 2-CP photodegradation over α -FeOOH (H₂O₂ molar concentration is 0.156 mM; catalyst dosage 0.375 g L⁻¹; initial concentration is 10 mg L⁻¹; temperature 30°C). 95
- 4.24 Effect of pH on 2-CP photodegradation over α -FeOOH/MSN (metal loading is 10wt%; H₂O₂ molar concentration is 0.156 mM; catalyst dosage 0.375 g L⁻¹; initial concentration is 50 mg L⁻¹; temperature 30°C). 96
- 4.25 Influence of H₂O₂ molar concentration on 2-CP photodegradation over α -FeOOH (pH 5; catalyst dosage 0.375 g L⁻¹; initial concentration is 10 mg L⁻¹; temperature 30°C). 97

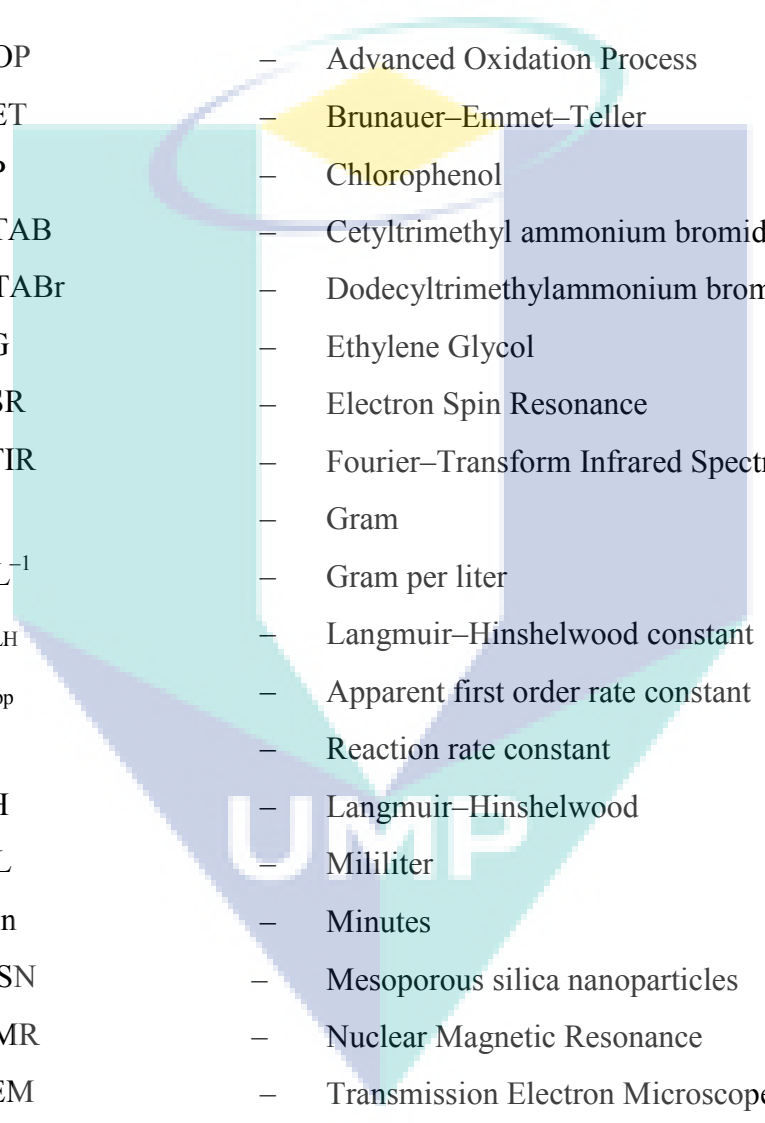
- 4.26 Effect of H_2O_2 molar concentration on 2-CP photodegradation over $\alpha\text{-FeOOH/MSN}$ (metal loading is 10wt%; catalyst dosage 0.375 g L^{-1} ; initial concentration is 50 mg L^{-1} ; temperature 30°C). 98
- 4.27 Influence of $\alpha\text{-FeOOH}$ dosage on 2-CP photodegradation (pH 5; H_2O_2 molar concentration is 0.156 mM ; initial concentration is 10 mg L^{-1} ; temperature 30°C). 99
- 4.28 Effect of catalyst dosage on 2-CP photodegradation over $\alpha\text{-FeOOH/MSN}$ (metal loading is 10wt%; H_2O_2 molar concentration is 0.156 mM ; initial concentration is 50 mg L^{-1} ; temperature 30°C). 100
- 4.29 Influence of initial concentration of 2-CP on 2-CP photodegradation over $\alpha\text{-FeOOH}$ (pH 5; H_2O_2 molar concentration is 0.156 mM ; catalyst dosage 0.3 g L^{-1} ; temperature 30°C). 101
- 4.30 Effect of initial 2-CP concentration on 2-CP photodegradation over $\alpha\text{-FeOOH/MSN}$ (metal loading is 10wt%; H_2O_2 molar concentration is 0.156 mM ; temperature 30°C). 102
- 4.31 Influence of reaction temperature on 2-CP photodegradation over $\alpha\text{-FeOOH}$ (pH 5; H_2O_2 molar concentration is 0.156 mM ; catalyst dosage 0.3 g L^{-1} ; initial concentration is 50 mg L^{-1}). 103
- 4.32 Effect of reaction temperature on 2-CP photodegradation over $\alpha\text{-FeOOH/MSN}$ (metal loading is 10wt%; pH is 5; H_2O_2 molar concentration is 0.156 mM ; initial concentration is 50 mg L^{-1}). 104
- 4.33 Plot of activation energy as a function of metal loading for 2-CP degradation. 105
- 4.34 Photodegradation efficiencies of 2-CP in the presence of hole scavenger, $\bullet\text{OH}$ scavenger, and electron scavenger by (A) $\alpha\text{-FeOOH}$ and (B) C-FeOOH [pH

	5, H ₂ O ₂ concentration 0.156 mM; catalyst dosage 0.30 g L ⁻¹ ; initial concentration 50 mg L ⁻¹ ; temperature 303 K].	107
4.35	Schematic illustration of 2-CP photodegradation over (A) C-FeOOH, and (B) photogenerated electron trapping by cationic surfactant headgroups of α-FeOOH	109
4.36	Photodegradation efficiencies of 2-CP in the presence of hole scavenger, [•] OH scavenger, electron scavenger, and [•] OH _{ads} scavenger by 10 wt% α-FeOOH /MSN catalyst [pH 5; H ₂ O ₂ concentration is 0.156 mM, catalyst dosage 0.40 g L ⁻¹ ; initial concentration is 50 mg L ⁻¹]	110
4.37	Schematic illustration of 2-CP photodegradation over α-FeOOH/MSN	111
4.38	The studentized residuals and predicted response plot for 2-CP photodegradation	116
4.39	Normal % probability and studentized residual plot for 2-CP photodegradation	117
4.40	The actual and predicted plot for 2-CP photodegradation.	117
4.41	3D response plot showing effect of temperature, catalyst dosage, and H ₂ O ₂ /2-CP ratio at fixed pH	118
4.42	Residual diagnostics for 2-CP photodegradation of normal probability plot	126
4.43	Residual diagnostics for 2-CP photodegradation of residual vs. predicted response plot	126
4.44	Response surface plot of (A and B) pH and reaction temperature; and (C and D) α-FeOOH metal loading and pH	128
4.45	Linear transform $\ln C_o/C_t = f(t)$ of 2-CP photodegradation over α-FeOOH.	130
4.46	Relationship between $1/r_o$ and $1/C_o$ at different initial	

	concentrations of 2-CP	131
4.47	Plot of $\ln C_0/C_t$ as a function of time (t).	132
4.48	Plot of $1/r_0$ as a function of $1/C_0$	133
4.49	Proposed degradation mechanism of 2-CP over the catalysts	134
4.50	Stability of α -FeOOH catalyst after subsequent reactions [pH 5; H_2O_2 concentration 0.156 mM, catalyst dosage 0.30 g L^{-1} ; initial concentration 50 mg L^{-1} , temperature is 323 K].	135
4.51	Stability of α -FeOOH catalyst after subsequent reactions [pH 5; H_2O_2 concentration 0.156 mM, catalyst dosage 0.30 g L^{-1} ; initial concentration 50 mg L^{-1} , temperature is 323 K]	136
4.52	Scale-up performance of the catalysts in 10-fold pilot scale system	138
4.53	Performance of catalysts for various pollutants	139

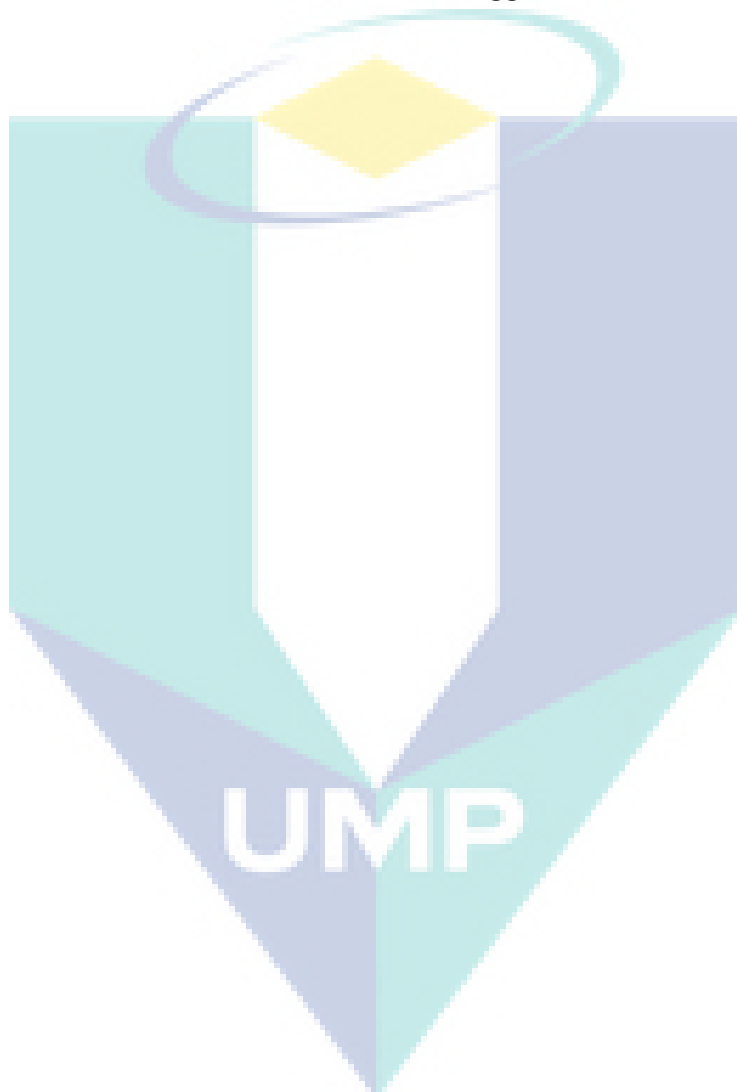
The logo for UMP (Universitas Muhammadiyah Purwokerto) is a large, downward-pointing arrow shape. It is composed of several overlapping triangles in shades of teal and light blue. The letters 'UMP' are printed in a bold, white, sans-serif font across the center of the arrow's shaft.

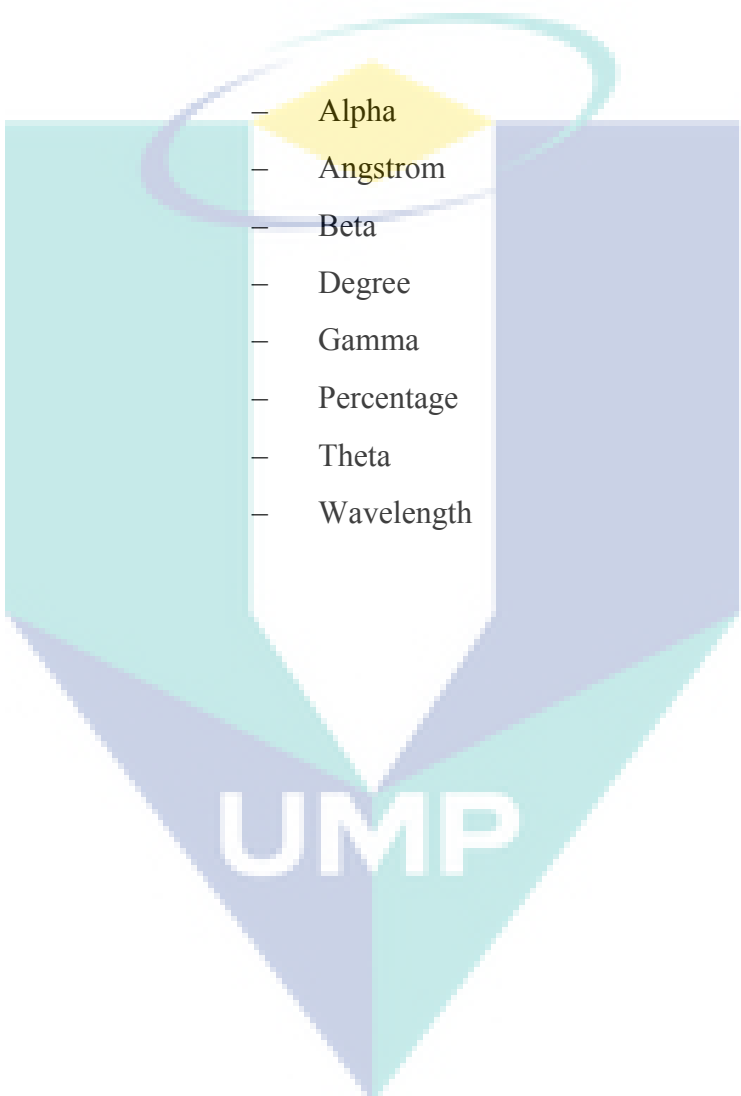
UMP

LIST OF ABBREVIATIONS

AOP	–	Advanced Oxidation Process
BET	–	Brunauer–Emmet–Teller
CP	–	Chlorophenol
CTAB	–	Cetyltrimethyl ammonium bromide
DTABr	–	Dodecyltrimethylammonium bromide
EG	–	Ethylene Glycol
ESR	–	Electron Spin Resonance
FTIR	–	Fourier–Transform Infrared Spectrometer
g	–	Gram
$g L^{-1}$	–	Gram per liter
K_{LH}	–	Langmuir–Hinshelwood constant
k_{app}	–	Apparent first order rate constant
k_r	–	Reaction rate constant
LH	–	Langmuir–Hinshelwood
mL	–	Mililiter
min	–	Minutes
MSN	–	Mesoporous silica nanoparticles
NMR	–	Nuclear Magnetic Resonance
TEM	–	Transmission Electron Microscope
TEOS	–	Tetraethylorthosilicate

UV-Vis/DRS	-	Ultraviolet-Visible/Diffuse Reflectance Spectrophotometer
wt%	-	Weight percentage loading
XPS	-	X-Ray Photoelectron Spectroscopy
XRD	-	X-ray Diffraction
α -FeOOH	-	α -FeOOH without support
α -FeOOH/MSN	-	α -FeOOH supported on MSN

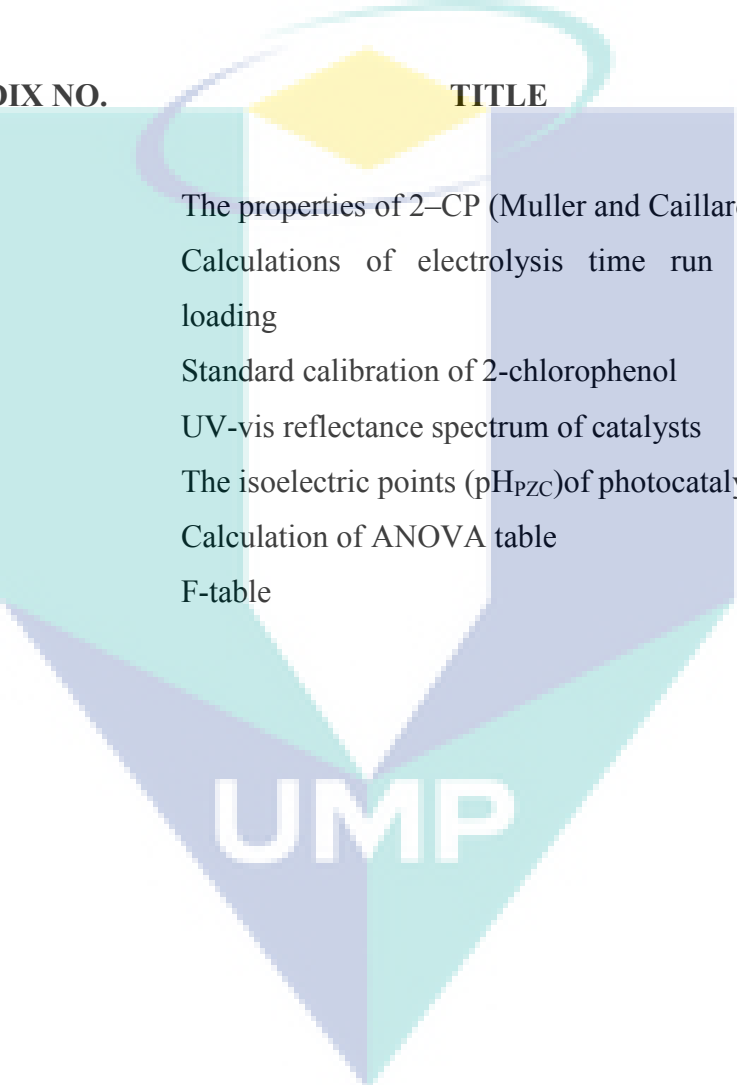


LIST OF SYMBOLS

α	—	Alpha
\AA	—	Angstrom
β	—	Beta
$^{\circ}$	—	Degree
γ	—	Gamma
%	—	Percentage
θ	—	Theta
λ	—	Wavelength

LIST OF APPENDICES

APPENDIX NO.	TITLE	PAGE
A	The properties of 2-CP (Muller and Caillard, 2011)	164
B	Calculations of electrolysis time run for wt% loading	165
C	Standard calibration of 2-chlorophenol	166
D	UV-vis reflectance spectrum of catalysts	167
E	The isoelectric points (pH_{PZC}) of photocatalysts	168
F	Calculation of ANOVA table	169
G	F-table	170

The logo for UMP (Universitas Muhammadiyah Purwokerto) is a large, downward-pointing triangle. The top part of the triangle is a light blue rectangle containing the text 'APPENDIX NO.' and 'TITLE'. The middle part is a white rectangle containing the text 'PAGE'. The bottom part is a dark blue triangle containing the text 'UMP'. The entire logo is set against a white background.

UMP

CHAPTER 1

INTRODUCTION

1.1 Research Background

Within the last decade, there has been a growing concern related to the health impact and environmental damage due to phenolic compounds. The occurrence and widespread use of the phenolic compound and its derivatives as aromatic solvents, cleaning agents, biocides, preservatives and pesticides in the environment represents a serious problem owing to their toxicity, perseverance and accumulation in the environment while soluble phenolic compounds have revealed their absolute potential to enter the food chain (Santana *et al.*, 2009). Adverse effects of the phenolic compounds and its derivatives on human, environment, as well as aquatic life have been recently reported (Maji *et al.*, 2014) and have been associated to numerous biological disorders (Mangrulkar *et al.*, 2008).

Chlorophenols as derivatives of the phenolic compound were identified as a pollution concern due to their high toxicity, high stability, and potentially carcinogenic. For this reason, United States Environmental Protection Agency (US EPA) had listed them as priority pollutants (Gordon and Marsh, 2009). In Malaysia, Department of Environment (DOE) has enacted allowable limits as in Environmental

Quality Act 1979 (Sewage and Industrial Effluent) that this pollutant should be treated to be less than 1 mg L^{-1} for inland water discharged.

Among chlorophenols, 2-chlorophenol (2-CP) has been considered to be the most toxic and carcinogenic. It is widely used in industry and daily life, and has caused considerable damage and threat to the aquatic ecosystem and human health (He *et al.*, 2011). Due to the severe toxicity of 2-CP, there is a continuing study over appropriate methods to be used when eliminating this organic compound from aqueous systems. Several removal techniques including adsorption and solvent extraction are available for removing chlorophenols. However, these techniques suffer from the possibility for the generation of secondary pollution (Khan *et al.*, 2011). Other than that, biological treatment which commonly used for the decomposition of many chlorinated phenols has proven ineffective since chlorinated phenols are resistant to biodegradation in a satisfactory time period (Bandara *et al.*, 2001a). Therefore, other treatment technologies have received increased interest to substitute the conventional treatment method.

Among diverse alternative treatment technologies, advanced oxidation process (AOP) has shown absolute potential during the last decades as an abatement method for the degradation of the chlorinated phenols. The term "AOP" is used to describe the production of very active species like hydroxyl radicals ($\bullet\text{OH}$) which depends on the oxidation mechanism. The treatment process provide a great advantage that they completely degrade the organic pollutants from the environment, which not only from the aqueous phase, but also by substituting them into other organic compounds before transforming them into innocuous inorganic species (Bertelli and Selli, 2006). Among various types and combinations of AOPs, the integration of two different AOPs (photocatalytic and Fenton-like), which commonly known as photo-Fenton-like, often offers synergistic reaction routes for the production of $\bullet\text{OH}$ and has been shown to be suitable for the degradation of various chlorinated phenol pollutants (Munoz *et al.*, 2011, Metz *et al.*, 2011).

The most extensively studied photocatalyst for the photodegradation of organic and inorganic contaminants in wastewaters is titania-based catalysts, especially titanium dioxide, TiO_2 (Khalil *et al.*, 1998). However, the commercial utilization of this catalyst is limited due the fact that TiO_2 aggregates rapidly in suspension which cause them to losing its surface area as well as the catalytic efficiency. Moreover, titania was proven to be unavailable for wider applications since it is only active with light radiation with wavelength approximately below 387 nm. Furthermore, due to the high costs required for separating and recovering these particles from the treated water, TiO_2 particles is not suitable to be used as the photocatalyst in a commercial suspension reactor system. Thus, there is an urgent need to develop a photocatalyst with high efficiency in employment of visible light irradiation, narrow band gap, stable in operation, and requires relatively low cost for the preparation (Guo *et al.*, 2007a).

Iron oxides/oxyhydroxides are relevant in many scientific and technical applications and have been widely used in AOP technology. Among them, goethite, also known as $\alpha\text{-FeOOH}$, is a type of iron oxyhydroxide with band-gap around 2.2 eV that seems to be a realistic candidate to be used as photocatalyst for degradation of 2-CP (Hu *et al.*, 2012b). It is considered as one of the most environmentally friendly catalysts and thermodynamically stable which important upon photocatalysis illumination (Prasad *et al.*, 2006). $\alpha\text{-FeOOH}$ also combines attractive properties for large-scale application such as resistance to photocorrosion, have wide range of operating pHs and proven to have almost undetectable leaching of iron into the solution.

The commercialized method for the preparation of $\alpha\text{-FeOOH}$ was known to be precipitation technique. However, this preparation technique may have several drawbacks related to longer time consumption, high temperature, and the precipitation conditions require extremely careful control (Gupta, 2003b). Therefore, it is necessary to find a simple and rapid route for the preparation of $\alpha\text{-FeOOH}$. Electrosynthesis is a simple method that has been explored for a few decades for the synthesis of nano-sized $\alpha\text{-FeOOH}$. Nano-sized $\alpha\text{-FeOOH}$ particles with structures

ranging from 1 to 100 nm in size have been shown to have unique physicochemical, surface, and optoelectronic properties, as well as excellent visible light photocatalytic activity (Ortiz de la Plata *et al.*, 2010c). Regarding these factors, there is an urgent need in synthesizing α -FeOOH nanomaterials by electrosynthesis method. Previously, gamma phase of FeOOH were successfully synthesized by electrosynthesis method as reported by Hashimoto and Cohen (1974). More recent, simpler electrolysis method for the preparation of metal nanoparticles was reported by Aishah *et al.*, (2002) employing dimethylformamide, naphthalene, and triethylammonium phosphate as its electrolyte.

Although electrosynthesis of α -FeOOH have been explored for few decades (Jiao *et al.*, 2009), the use of surplus organic solvents urges the needs of investigating other alternatives in substituting the conventional solvents. Moreover, small (< 5 nm) nanoparticles tend to agglomerate due to high surface energy and the large surface area. In these scenarios, surfactant can be an alternative. Surfactants are composed of both hydrophilic and hydrophobic groups, with the presence of charged hydrophilic component. Cationic surfactants, which contain positive charged ions, have always sparked researcher's interest due to their peculiar and interesting properties which include—contrasting hydrophobic and hydrophilic nature; tendency to self associate; ability to solubilize both polar as well as non polar components, etc. (Kaur and Mehta, 2014). It has abundance of charge—carrying ions which allows its usage as solvent without the need for supporting electrolyte. Moreover, cationic surfactants has been extensively used as templates in the preparation of various materials as it provide electrosteric protection through strongly coordinating protective ligand and can be efficiently used as scaffolds for nanostructure materials (Nikoobaht and El-Sayed, 2001).

Besides the needs of synthesizing iron nanometal, research has been oriented to the iron compounds immobilization on different carriers. This is to facilitate iron separation and to avoid more complex post—treatments (Feng *et al.*, 2003). Recently among commonly employing solid supporters, mesostructure materials have been attracted interest as functional carrier due to their high surface area, assessable pore

channels, simple pore chemistry and enhanced powder recoverability (Deng *et al.*, 2011). Moreover, it was proven that mesoporous-assembled structure with incorporation of metal catalyst offer better light-induced hydrophilicity, which therefore exhibiting higher photocatalytic activities than non-mesoporous-assembled catalyst (Puangpetch *et al.*, 2010).

System upscaling is a critical factor in order to demonstrate the practicability of synthesized photocatalysis and the catalytic system for environmental remediation. The reality of research based photodegradation system is that very few systems for laboratory scale test are ultimately viable in terms of industrial scale up (McCullagh *et al.*, 2011). Therefore, it is necessary to study the capability of the laboratory scale system to be used in pilot scale which will provide the benchmark for industrially practicable applications.

1.2 Problem Statement and Hypothesis

2-CP have been widely used in agriculture, paper, cosmetic, biocide, public health industries and can also be formed as a result of chlorination in water. Because of its toxicity, carcinogenicity, yet poor biodegradability, 2-CP is among the priority pollutants of major environmental concern. The individual dose requires to kill 50% of a population of mice (LD_{50}) values determined indicate that 2-CP is considerably more toxic than dichlorophenols (Mozia *et al.*, 2012). Moreover, 2-CP is known to be the starting materials to dioxins and furans, the most toxic chemicals ever studied. Therefore, it is very important to degrade the 2-CP into harmless species.

Various techniques including solvent extraction, membrane filtration, adsorption, and biological degradation have been developed for degrading 2-CP from waters. However, these techniques suffer from several drawbacks related to

high cost, time consuming, and have the possibility of producing secondary pollutant. Furthermore, 2-CP do not undergo direct sunlight photolysis in the natural environment since they only absorb light below 290 nm. Thus, there are needs in searching other possible degradation method and recently, semiconductor-based photocatalysis has shown promise in degrading the toxic compounds into innocuous inorganic species.

Meanwhile, the commercialized method for preparation of α -FeOOH was known to be precipitation technique but it may have several disadvantages related to longer time consumption, high temperature, and the precipitation conditions require extremely careful control. Therefore, it is necessary to find a simple and rapid route for the preparation of α -FeOOH. Although electrosynthesis of α -FeOOH have been explored for few decades, the use of surplus organic solvents and the tendency of nanoparticles to agglomerate urge the needs of investigating other alternatives in substituting the conventional solvents. In these scenarios, cationic surfactant can be an alternative.

Moreover, the study on the interaction of electrosynthesized metal oxide in cationic surfactants with a mesostructured silica nanoparticles support is still rare. Although several studies have been conducted to deposit the metal-surfactant catalyst onto several supports including clay (Mastalir *et al.*, 2001), metal oxide (Sato *et al.*, 2002), and activated carbon (Porta *et al.*, 2002), the interaction between the metal oxides and the support material was not well-studied. Moreover, the properties of the catalyst are known to be strongly affected by the support, which makes it very complicated to understand its reaction mechanism. Thus, detail investigation on supported metal catalyst is very crucial.

For many iron oxides-based catalysts employed in photo-Fenton-like system, the fastest rates in solution were observed at strong acidic pH (Ortiz de la Plata *et al.*, 2010a). This selection, however, introduces the need for acidification of the reacting medium and subsequent neutralization after treatment. Thus, nearly

neutral condition appears as more favorable in employing photo-Fenton-like system which suggests an attempt to conduct the system at mild pH condition (Kolata *et al.*, 1994). On the other hand, insufficient amount or a disproportionate excess of H_2O_2 concentration can result in negative effects of the photo-Fenton-like system (Burbano *et al.*, 2003). Since the selection of a reduced H_2O_2 concentration for the degradation of pollutants is important from practical point of view due to the cost and toxicity (Sun *et al.*, 2007), an attempt is necessary to investigate the behavior of the system and to reduce the amount of H_2O_2 required for efficient degradation.

The $\alpha\text{-FeOOH}$ and $\alpha\text{-FeOOH/MSN}$ catalysts synthesized in cationic surfactant was hypothesized to endow extra properties on the characteristics of the catalyst which is believed can hinder the electron-hole recombination, as well as induce the capability of the catalysts to be used in visible light regions. The high surface area of MSN provides well distributions of the iron oxides on the surface of MSN besides the ability of MSN to act as an electron acceptor to synergically perform with the loaded $\alpha\text{-FeOOH}$ to enhance the photodegradation activity. Along this line, herewith we proposed to focus on the “Electrosynthesis of goethite supported on mesostructured silica nanoparticles in cationic surfactant for photodegradation of 2-chlorophenol”.

1.3 Objective of the Study

The objectives of this study are:

1. To synthesize and characterize nanosized $\alpha\text{-FeOOH}$ and $\alpha\text{-FeOOH/MSN}$ catalysts.
2. To optimize the photocatalytic degradation of 2-chlorophenol over the synthesized catalysts by Response Surface Methodology (RSM).

3. To study the degradation mechanism and kinetic modeling of the photocatalytic process.
4. To study the potential of the synthesized catalysts for pilot plant scale applications.

1.4 Scope of the Study

The scopes of this study consist of four parts which are;

1. Synthesis and characterize nanosized α -FeOOH and α -FeOOH/MSN catalysts
 - i. The α -FeOOH was synthesized in cationic surfactant via electrosynthesis method in a normal compartment cell fitted with a cathode and anode plate at a constant current density of 120 mA cm^{-2} under ambient atmosphere at 0°C . The α -FeOOH was also supported on mesostructured silica nanoparticles (MSN) to give α -FeOOH/MSN catalyst using impregnation method.
 - ii. The physicochemical properties of the catalysts were determined by different means of characterizations. The crystallographic structure, crystallite size, and structural orientation of the prepared catalysts were recorded using X-ray diffraction (XRD) analysis. The morphological properties and distribution of metal oxides onto supportive material were examined using transmission electron microscopy (TEM). The vibration information of the catalysts was elucidated by Fourier transform infrared (FTIR) spectroscopy. Nitrogen adsorption-desorption isotherms (Brunnauer-Emmett-Teller, BET) was used to obtain the textural properties of catalysts. The chemical oxidation state of the catalysts was determined using X-ray photoelectron spectroscopy (XPS). The chemical environments of Si atoms were detected using ^{29}Si magic angle spin nuclear magnetic

resonance (^{29}Si MAS NMR). The band gap energy determination of the catalysts were studied using ultraviolet–visible diffuse reflectance spectroscopy (UV–vis DRS) while the optical properties of the catalysts were analysed by photoluminescence spectroscopy (PL). The mechanistic pathway for the structure formations were also proposed based on the characterizations results.

2. The catalytic activity of the catalysts were tested on photodegradation of 2–CP in aqueous solution. The screening process was conducted to identify crucial process conditions including the effect of metal loading, pH, catalyst dosage, H_2O_2 concentration, 2–CP initial concentration, and temperature. Optimization of the photodegradation system was done via Response Surface Methodology (RSM) using statistical software package Design–Expert, by employing sequence optimization of full factorial design and central composite design.
3. The mechanisms of the 2–CP photodegradation over the catalysts were studied by using several scavengers. Four types of scavengers were used for the system: potassium dichromate (PD); isopropanol (IP); sodium oxalate (SO); and potassium iodide (PI), with the role as a scavenger of photogenerated electrons, hydroxyl radicals ($\bullet\text{OH}$), photogenerated holes (H^+), and hydroxyl radicals adsorbed on the catalyst surface ($\bullet\text{OH}_{\text{ads}}$), respectively. The kinetic modeling of the photocatalytic process was investigated using Langmuir–Hinshelwood model to accommodate reactions occurring at solid–liquid interface. The reaction rate constant (K_R) and the adsorption equilibrium constant (K_{LH}) were calculated to determine the type of reaction occurs during the photodegradation process.
4. The potential of the catalysts for applications in pilot scale was studied in the aspects of reusability, upscaling feasibility, and degradation ability on various pollutants. The reusability of the catalysts were investigated to indicate the robustness of the catalysts towards the photodegradation process. Repeated experiments were carried out using same operating

conditions and the performances of the catalysts at each reaction cycles were compared. The feasibility of up-scaled system for photocatalytic degradation of 2-CP was investigated using a pilot scale reactor system with a 10-fold upscale system of the laboratory scale. Lastly, the potential applications of the catalysts to various target pollutants were investigated using cationic dye, anionic dye, and phenol.

1.5 Significance of Study

In this study, detailed investigation on the 2-CP degradation using α -FeOOH and α -FeOOH/MSN catalysts via photo-Fenton-like process was conducted. The employment of the photocatalysts to give complete degradation of 2-CP under mild operating conditions provide new insight in reducing the use of oxidizing agents which normally employed in huge amounts for this catalytic system. This study also provides a platform to eliminate the subsequent neutralization process which commonly required in most of the 2-CP degradation processes. Furthermore, the proposed degradation mechanism using the catalysts offers better understanding of the catalytic process employing metal-surfactant catalyst supported on a silica material.

The simple and rapid route for the synthesis of the catalysts offers new alternative to current commercial synthesis process since this electrosynthesis method using cationic surfactant as a single electrolyte avoids the surplus use of the organic solvents. The study on the mechanistic pathways for the formation of the electrosynthesized metal-surfactant catalyst presents additional knowledge in current progress in this research area. Moreover, the study on the interaction of electrosynthesized metal oxide in cationic surfactants with a mesostructured silica nanoparticles support may provide new insight to the current understanding in the metal-surfactant field.

1.6 Thesis Outline

This thesis is divided into five chapters. In Chapter 1, introduction is given about the wide usage of phenolic compound and the importance on the degradation of the chlorinated phenolic compound, especially 2-chlorophenol which caused severe problems to human and environment. Several techniques were reported to potentially overcome this problem including physical, biological, and chemical treatment. The potential of α -FeOOH and α -FeOOH/MSN as semiconductor for photo-Fenton-like process are highlighted. The problem statement of the current research was stated which subsequently provide a clear objective of the present study. The scope of study covers the research which was done to meet the objectives. The significance of research was also clearly mentioned.

Chapter 2 or literature review covers the conventional method of 2-CP degradation, basic information of 2-CP and characteristics of α -FeOOH and MSN as previously studied. The previous studies on photoreactor scaling up also included. Chapter 3 or methodology describes the chemicals and materials used in the research work, instrumentations, catalysts preparation and characterizations, experimental setup, photodegradation testing, and it also includes the procedure for the analysis calculations.

Chapter 4 concerned with the results and discussion which in further divided into seven parts. The first part is synthesis and characterization, followed by the photodegradation performance evaluation, optimization of reaction conditions, kinetic analysis, reusability study, scaling up system, and the last part is the capability study of the catalysts towards various pollutants. The results are presented and discussed comprehensively. Finally, Chapter 5 covers the results summary and future study.

CHAPTER 2

LITERATURE REVIEW

2.1 Introduction

Chlorophenols are widely used in many industrial processes for the applications of drugs, pesticides, explosives, and dyes. Because of its toxicity, carcinogenicity, yet poor biodegradability, chlorophenols is among the priority pollutants of major environmental concern (Mozia *et al.*, 2012). Due to the urgent needs to degrade this compound, various techniques including solvent extraction, membrane filtration, adsorption, and biological degradation have been developed for degrading 2-CP from waters. However, these techniques suffer from several drawbacks related to high cost, time consuming, and have the possibility of producing secondary pollutant. Furthermore, 2-CP do not undergo direct sunlight photolysis in the natural environment since they only absorb light below 290 nm. Thus, there are needs in searching other possible degradation method and recently, semiconductor-based photocatalysis has shown promise in degrading the toxic phenolic compounds and its derivatives into innocuous inorganic species.

2.2 Phenolic Compound

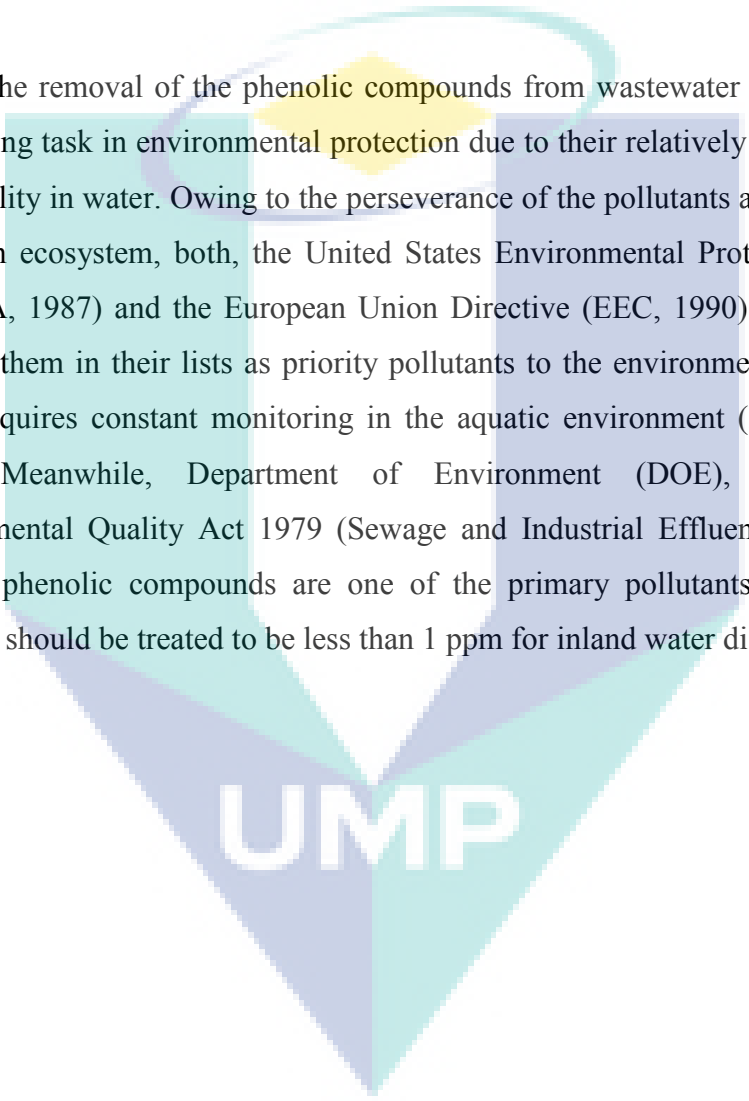
Phenolic compounds are a class of chemical compounds which contains one or more hydroxyl groups bonded on a benzene ring. The aromatic compound with one hydroxyl group attached to its structure is commonly known as phenol, the simplest compound of the class, with the molecular formula of C_6H_5OH . Additional substitution of other functional groups such as chloro, nitro, and methyl group in this phenol molecule are regularly named as phenolic derivatives. The position of the additional group in the derivatives are located either by ortho, meta, para prefix or by the numbering system (Carey, 2000).

The phenolic compound and its derivatives are widely used in many industrial processes as essential ingredients for a large production of chemicals related to the applications of drugs, pesticides, explosives, and dyes. Apart from that, they are normally used in the bleaching process of paper manufacturing as well as in textile industries. In addition, phenolic compounds are also known to have a substantial application in agriculture field as herbicides, insecticides and fungicides (Santana *et al.*, 2009). Furthermore, it was reported that the production level of the phenol and its derivatives is about 7 billion kg per year, which subsequently indicates the commercial importance of the compounds (Maji *et al.*, 2014). Meanwhile, besides being generated into the environment by human activity, phenolic compounds and its derivatives are also formed naturally in the ecosystem. As a result, they are usually found in sediments and soils, and this often leads to the contamination of ground water and wastewater.

The presence of the phenolic compounds in the environment as low as in parts per million (ppm) concentrations was identified to be extremely toxic for the human, environment, as well as aquatic life (Maji *et al.*, 2014). It has been found that the concentration of the phenolic compound is ranged between 6 to 7000 ppm in industrial wastewater streams discharged to the environment (Maarof *et al.*, 2004). Moreover, they are known to be estrogenic, carcinogenic and mutagenic

when present at elevated levels in the environment as well as capable to exert negative effects on different biological processes (Mangrulkar *et al.*, 2008). In addition, the phenolic compounds have high tendency to bioaccumulate in the environment. Therefore, due to their numerous drawbacks, phenolic compound and its derivatives has recognized as one of the major, persistent and recalcitrant pollutants to the environment.

The removal of the phenolic compounds from wastewater has becomes a challenging task in environmental protection due to their relatively high solubility and stability in water. Owing to the perseverance of the pollutants and their severe effects in ecosystem, both, the United States Environmental Protection Agency (US EPA, 1987) and the European Union Directive (EEC, 1990) have included some of them in their lists as priority pollutants to the environment (Figure 2.1) which requires constant monitoring in the aquatic environment (Elghniji *et al.*, 2012). Meanwhile, Department of Environment (DOE), Malaysia in Environmental Quality Act 1979 (Sewage and Industrial Effluent) has enacted that the phenolic compounds are one of the primary pollutants in which the pollutant should be treated to be less than 1 ppm for inland water discharged.



UMP

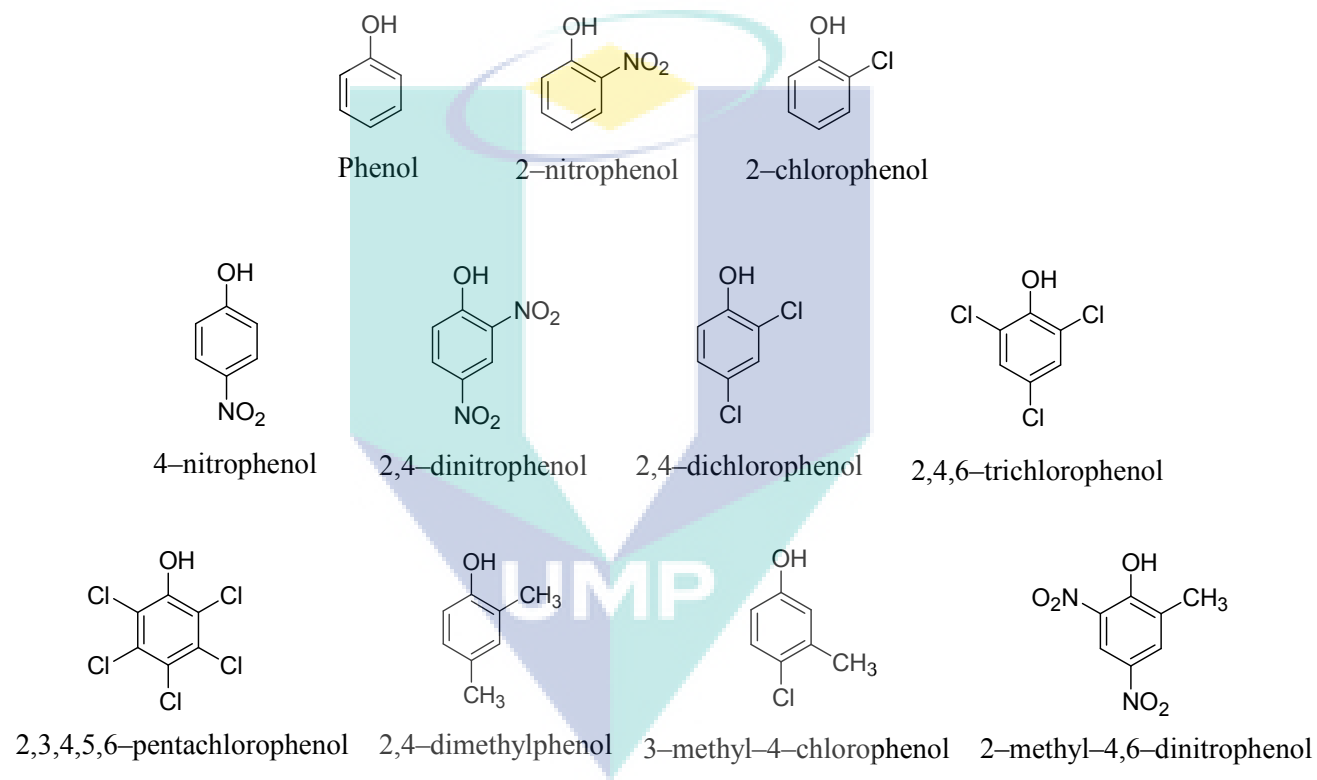


Figure 2.1 Phenolic compounds considered priority pollutants by US EPA and EU

2.2.1 Chlorophenol

Chlorinated phenol is any phenol compound that contains one or more chlorine atoms bonded on its structure. Most chlorophenols commonly have a number of different isomers. Since three ring positions on the phenol molecule can only occupy one chlorine atom, monochlorophenols have three isomers. 2-chlorophenol, for example, is the isomer that has a chlorine atom in the ortho position. Pentachlorophenol, by contrast, has only one isomer due to fully chlorinated five available ring positions on the phenol.

Chlorophenol have a wide range of applications due to its structural variety and divergent chemical properties. During decades, chlorophenols have been widely used as wood preservative agents and disinfectants, so there have been a surplus released in the environmental media. The existence and widespread use of chlorophenol in aromatic solvents, pesticides, cleaning agents, preservatives, and biocides in the environment represents a serious problem due to their toxicity, perseverance, and accumulation potential in plants and animal tissues (Bandara *et al.*, 2001a). Soluble chlorophenol compounds have recently shown their extensive potential to enter the food chain. Besides that, these compounds are commonly found in natural water bodies due to their low and inefficient biodegradability.

The most complex chlorophenol compound, pentachlorophenol, is still widely found in the wood of pallets, containers, crates and in cardboard, paper, etc. although its usage is prohibited in most countries. Since fresh fruits are often been stored and transported using wooden crates and cardboard boxes, chlorophenols which present in these materials may contaminate the stored fruits by migration. Tri-, tetra- and pentachlorophenol are proven to be the precursors in the formation of the chloroanisoles which known to be powerful odorants in corks and wine. This is one of the most serious problems in the enological industry. In addition, more hydrophilic phenols, such as less chlorinated phenols, are easily dispersed in the aquatic media, which has increasing the concerns regarding the presence of the

substance in inland water. Meanwhile non polar compounds which are the more chlorinated phenols are usually persisting in a longer time period in the environment (Santana *et al.*, 2009).

Other related concerns is that the chlorinated phenols can also be produced from nonchlorinated phenols during drinking water chlorination. The taste and odour of drinking water will be highly affected by chlorophenols which are toxic and carcinogenic with concentrations as low as a few $\mu\text{g L}^{-1}$. As a result, a maximum concentration of $0.5 \mu\text{g L}^{-1}$ in drinking water was set by EU Directive 2455/2001/EC and $0.1 \mu\text{g L}^{-1}$ is the threshold value for their individual concentration.

2.2.2 2-Chlorophenol (2-CP)

2-chlorophenol (2-CP) is a monochlorophenol compound in which the chlorine molecule is bonded to the phenol structure at ortho position. 2-CP is widely used in various chemical processes such as in the agricultural, paper, cosmetic, biocide, and public health industries; it can also be formed as a result of chlorination in drinking water treatment. It have frequently used as a precursor for synthesizing pesticides and other chlorophenols (Guo *et al.*, 2012c).

Among chlorophenol compounds, 2-CP has been regarded as a unique class of pollutants which has been considered as most toxic to aquatic life as well as mammalian at concentrations as low as parts per billion level. Moreover, the 2-CP was found to be the most persist and carcinogenic pollutant in its class (Wei *et al.*, 2014).

2-CP was also reported as a common precursor for poly-chlorinated dibenzo-p-dioxins and poly-chlorinated dibenzofurans (PCDD/F), which are environmental pollutants that can contaminate and are monitored in food, rivers, and atmosphere (Gao and Teplyakov, 2014b). In addition, the LD₅₀ values determined in mice indicate that 2-CP is considerably more toxic than dichlorophenols (Mozia *et al.*, 2012), indicating the severe effects of this monochlorophenol pollutant to the surrounding ecosystem.

2.3 Degradation Method

The wide usage of chlorophenol and contamination to drinking water urges the need to degrade or remove the toxic compound to avoid further risks to the human and environment. Wastewater treatment is necessary to remove chlorophenols before their potential discharge into the environment. Therefore, many interests to remove chlorophenol from aqueous solution have aroused in the last few years that leads to the development of effective methods for chlorophenol removal.

2.3.1 Biological Method

Biological method is to introduce contact of organic materials in the wastewater with bacteria (cells), which thereby reducing its BOD content. The method is usually more economical compared to other method due to it usage of commonly found microorganisms which are known to degrade and accumulate different organic pollutants.

Microflora in natural systems, aerobic as well as anaerobic, has remarkable ability to eliminating chlorophenols compounds over prolonged exposure. Several researchers have found aerobic process such as aerated lagoon is beneficial to chlorophenols treatment with some modifications on the process (Holladay *et al.*, 1978). Besides that, research has also shown that chlorophenols can be effectively treated biologically under anaerobic conditions but sludge acclimatization is necessary (Ye and Shen, 2004). It was reported that removal efficiency of chlorophenol would be enhanced by operating anaerobic and aerobic treatment processes in combination.

Nevertheless, it has been reported that the biodegradability of phenolic compounds are critically depends on the number, type, and position of substituent on the phenolic ring. (Annachhatre and Gheewala, 1996). It is are less readily biodegradable than phenol thus proves that their rate of biodegradation decrease with increasing number of chlorine substituent on the aromatic ring.

However, there are certain limitations in this type of treatment process. The sensitivity of bacteria toward chlorophenols may vary, depending on the bacterial species as well as the chlorophenol congener. Other than that, chlorinated phenols are resistant to biodegradation in an appropriate time period and tend to accumulate in sediments (Bandara *et al.*, 2001a). Therefore, the current biological method seems to be unpromising to completely degrade the chlorophenols which then urges the needs to study other possible alternatives for removal of these pollutants.

2.3.2 Physical Method

A physical treatment method is process units in which the applications of physical forces are predominate. In general, physical treatment mechanisms do not

result in changes in chemical structure of the target substances. Adsorption, as a type of physical treatment method, is widely used in industrial applications. In this process, atoms of the surface functional group donate electron to the sorbate molecules leads to the occurrence of adsorption by the donor–acceptor complexation mechanism (Al Duri, 1995). Generally the factors like initial concentration, initial pH and effluent temperature affect the removal process (Li *et al.*, 2009b).

Adsorbents commonly used to remove chlorinated phenols from aqueous solution include clays, modified clays, granular activated carbon, and polymer resins. Although clays have large surface area, its uptake of chlorophenols is not significant of its low total organic carbon content. It was reported that the adsorption capacity of chlorophenols on activated carbon could reach up to 130 mg g^{-1} in a column study (Gupta *et al.*, 2000a). Although satisfactory outcomes has been achieved using this method, high cost of producing the commercial activated carbon may hinder its practical use. Furthermore, the generation of secondary pollutants has also increase the public awareness on its usage.

2.3.3 Chemical Method

Chemical treatment is a treatment method in which the conversion or removal of contaminants is carried out by the addition of chemicals or by other chemical reactions. Solvent extraction is a chemical method to separate compounds in two different immiscible liquids, normally water and an organic solvent, based on their relative solubility. It involves the extraction of a substance from one liquid phase into another liquid phase. Liquid–liquid extraction is performed using a separatory funnel and it is a basic technique in chemical laboratories. This type of process is usually performed after a chemical reaction as part of the work–up.

Extraction by emulsion liquid membrane is an attractive alternative of chlorophenol degradation because of its high efficiency and recovery of phenolic compounds for reuse as raw materials. Since the initial work by Li (1968a), liquid membranes have demonstrated considerable potential as effective tools for an increasing variety of separation applications.

However, liquid–liquid extraction is time consumption and requires a large volume of sample and of toxic organic solvent. It is also difficult to automate. Solid phase extraction (SPE) is another often–applied technique for the extraction of phenols. Although the SPE techniques are easier to automate compared to liquid–liquid extraction, they still require quite significant amount of organic solvents used to degrade significant amount of chlorophenols (Schellin and Popp, 2005).

2.4 Advanced Oxidation Process

Advanced oxidation process (AOP) is a set of designed treatment procedures to remove organic and inorganic contaminants in waste water by oxidation. The term “AOP” refers to the oxidation mechanism that depends on the production of very active species such as hydroxyl radicals ($\bullet\text{OH}$). Commonly, contaminants are oxidized by four different reagents which are ozone, hydrogen peroxide, oxygen, and air. These procedures may also be combined with UV light irradiation and specific catalysts.

Oxidation is referring to the transfer of one or more electrons from an electron donor to an electron acceptor, which has a higher affinity for electrons. These electron transfers result in the chemical transformation of both the acceptor and the donor, which in some cases producing chemical species with an odd number of valence electrons. These species which known as radicals is tend to be unstable

and therefore, highly reactive because due to one unpaired electrons. Additional oxidation reactions between the radical oxidants and other reactants (both organic and inorganic) follows the oxidation reactions that produce radicals until thermodynamically stable products are formed. The oxidation potential will be study to indicate the ability of an oxidant to initiate chemical reactions. The most powerful and commonly used oxidants are fluorine, hydroxyl radicals ($\bullet\text{OH}$), ozone, and chlorine with oxidation potentials of 2.85, 2.70, 2.07 and 1.49 electron volts, respectively (Dorfman and Adams, 1973). The end products of complete oxidation of organic pollutants are carbon dioxide (CO_2) and water (H_2O).

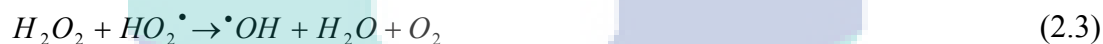
The AOP procedure is particularly practical for cleaning non-degradable materials such as petroleum constituents, pesticides, aromatics, and volatile organic compounds in waste water. The contaminant materials are converted into stable inorganic compounds such as water and carbon dioxide. The aim of the waste water purification by means of AOP procedures is the reduction of the chemical contaminants and the toxicity to such an extent that the cleaned waste water may be able to be reintroduced into receiving streams or, at least, into a conventional and simple sewage treatment.

AOP has shown promise during the last decades as a decontaminant method for the degradation of chorophenols compounds. The process present the great advantage that they completely remove organic contaminants from the environment by transforming them into other organic compounds and finally into non-hazardous inorganic species (Bertelli *et al.*, 2006).

It has been reported by Taleb (2014) who has synthesized the $\text{CS}/\text{CoFe}_2\text{O}_4$ nanocomposites via γ -irradiation cross-linking method with the aid of sonication. The catalyst was found to degrade 2-CP under sunlight irradiation with high photocatalytic efficiency. However, the optimum conditions for the system was found to be at alkaline medium with pH of 10 and the photocatalytic degradation of 2-CP performed best at low initial 2-CP concentration. More recent, the degradation

of 2-CP by ZnO thin film was reported by Rashid *et al.* (2015). The ZnO thin film with 200 nm thickness showed the highest efficiency for the degradation. However, the conditions requires high acidic condition (pH 3) to achieve complete degradation of 2-CP. Meanwhile, the effect of tri-elemental doping specifically potassium (K), aluminum (Al) and sulfur (S) on the performance of the synthesized titanium dioxide (TiO₂) nanoparticles under visible light illumination for the degradation of 2-CP has been reported by Tolosa *et al.* (2011). It was found that the 2-CP degradation was increased up to 96% in 4h irradiation at low initial concentration of 2-CP.

AOP involve four steps which are initiation (Eq. 2.1), hydroxyl radical propagation (Eq. 2.2–2.3), hydroxyl radical termination (Eq. 2.4–2.6), and decomposition (Eq. 2.7) which show the photochemical and chemical reactions in UV radiation with H₂O₂ (Xu *et al.*, 2009) where *X* is the contaminants.



2.4.1 Fenton Degradation

Fenton, an advanced oxidation process, is an attractive environmental remediation technology in which H₂O₂ is catalytically converted to reactive radicals in the presence of soluble ferrous ions as homogenous catalysts. Fenton process has

been used in the acute toxicity removal in textile finishing wastewater, degradation of nitroaromatic explosives, and treatment of simulated wastewater containing phenolic compound (Sheydaei *et al.*, 2014).

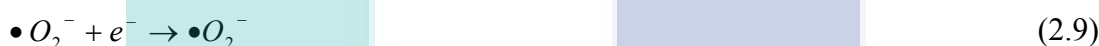
Fenton oxidation was found to be efficient and cost-effective method for treating various pollutants. However, homogenous Fenton oxidation to generate $\bullet\text{OH}$ using H_2O_2 and Fe^{2+} is effective at only narrow pH conditions while it generates iron sludge after treatment (Kim and Kan, 2015). Since application of homogeneous ferrous ions has some drawbacks such as iron precipitation and the deactivation of Fenton process, studies concerning heterogeneous iron sources such as oxides nanoparticles become appropriate alternatives.

2.4.2 Fenton-like Degradation

Fenton-like process was usually denoted when heterogeneous iron sources were used with the oxidants such as H_2O_2 . The catalyst used in this process should be in big sizes or supported on appropriate support to facilitate its separation after wastewater treatment (Sheydaei *et al.*, 2014). Different from the Fenton system, Fenton-like system commonly employs the semiconductor in the form of particle, commonly nanoparticles, to substitute the use of ferrous ion. Apart from the usage of oxidizing agents, the concept of Fenton-like degradation employing light irradiation is very similar to the photocatalytic degradation system. Photocatalytic degradation is discussed in details in the next section.

2.4.3 Photocatalytic Degradation

Environmental photocatalytic on semiconducting surfaces have been shown promise during the last few years to be determined by the surface adsorbed species which known to play a vital role in scavenging the photogenerated charges. Photocatalytic remediation was found to be suitable for aqueous solutions that contain organic compounds and reducible toxic metal ions in water and wastewater treatment technologies since it was found that the photocatalytic oxidation of organics and reduction of metals are synergistic (Mohapatra et al., 2005). This observation was explained in terms of a closed redox cycle whereby the photocatalyzed oxidation destroyed the organics while the metals are removed by reduction. The photocatalytic steps are summarized in Eq. 2.8 –2.15.



2.4.4 Photo-Fenton-like Degradation

Application of light radiation together with Fenton-like process is another improvement of AOP process that often called photo-Fenton-like process. Photo-Fenton-like process is one of the advanced oxidation processes (AOP). In definition,

photocatalysis combined with Fenton-like reaction is the photoreaction acceleration with the presence of a catalyst with the aid of strong oxidizing agents such as H_2O_2 .

In catalyzed photolysis, light is absorbed by an adsorbed substrate and the photocatalytic activity depends on the capability of the catalyst to generate electron-hole pairs, which then generate free radicals. When the catalyst is subjected to radiation beyond the material's band gap, electron-hole pairs are produced so that additional electrons enter the conduction band, while holes will remain in the valence band. These photo-generated electron-hole pairs will then facilitate redox reactions through the formation of adsorbed radicals on catalyst surfaces. The photocatalytic activity of the catalyst depends on the levels of adsorbed radical-forming species on the catalyst surfaces as well as the relative rates of generation and recombination of electron-hole pairs.

The integration of this AOPs often offers synergistic reaction routes for the production of $\bullet OH$, and has been shown to be suitable for the degradation of various chlorinated phenol pollutants (Munoz *et al.*, 2011, Metz *et al.*, 2011). The development of this catalytic system, which works not only under UV light but also under visible light, has been a great concern regarding the efficient utilization of solar light and the need to address the world's energy problems. However, the photo-Fenton-like catalysts used generally face a practical problem, i.e., the undesired electron-hole pair recombination that represents a major energy-wasting step that may hinder the system efficiency under visible light irradiation (Zhao *et al.*, 2012). In addition, in the photo-Fenton-like system, the fastest rates in solution are observed at strong acidic pH, which introduces the need for acidification of the reacting medium and subsequent neutralization after treatment. Therefore, the improvement of this system has increase crucial interest among the researchers.

2.4.5 Optimization of Process Conditions

Conventional and classical methods of studying a degradation process by maintaining other factors involved at an unspecified constant level does not depict the combined effect of all the factors involved. This method is also time consuming and requires large number of experiments to determine optimum levels, which are unreliable. These limitations of a classical method can be eliminated by optimizing all the affecting parameters collectively by statistical experimental design such as Response Surface Methodology (RSM).

RSM is a collection of mathematical and statistical techniques useful for developing, improving and optimizing processes and can be used to evaluate the relative significance of several affecting factors even in the presence of complex interactions. The main objective of RSM is to determine the optimum operational conditions for the system or to determine a region that satisfies the operating specifications. The application of statistical experimental design techniques in various process developments can result in improved product yields, reduced process variability, closer confirmation of the output response to nominal and target requirements and reduced development time and overall costs (Annadurai *et al.*, 2002).

Photo-Fenton-like system is multifactor system. The efficiency of the process strongly depends on process parameters. Hence, the optimization of such system can be complicated and costly. In order to reduce prolong laboratory studies and save time and money, the application of modelling tools in combination with experimental approach such as response surface modelling (RSM) is favourable. Although the use of RSM is quite common for optimization of chemical processes, only few investigators (Joshi *et al.*, 2008, Goswami *et al.*, 2010) have used it using the combination of initial and second optimization method. This sequential optimization method is more systematic and capable to indicate the most optimum condition. Commonly, optimization cannot fully reach as investigators only

employed one step of optimization which leads to the imprecise optimum conditions. This is because investigators tend to eliminate a value to minimize the experimental which the variables that was eliminated have significant effects on the response due to experimental conventional methods. Therefore, fully interaction (shown in Figure 2.2) cannot be analyzed.

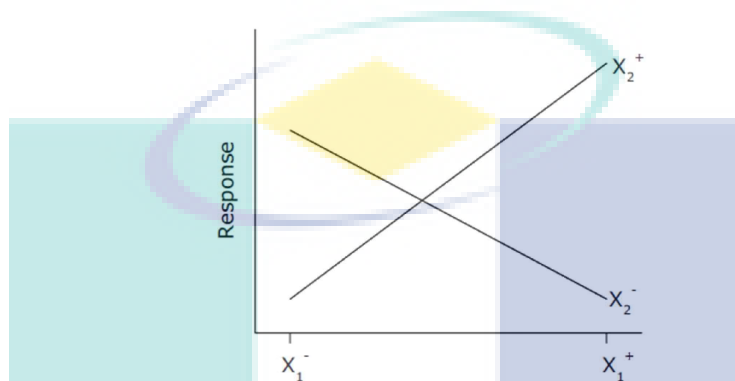


Figure 2.2 Interaction between variable X_1 and X_2 over the response

In order to employ sequential optimization approach, the important variables are first identified by a two-level factorial design. The total of independent variables, k are first selected for the study, where each variable represented at two levels, high (+) and low (-), in x trials as generated by the software.

Meanwhile, for optimization of screened variables, central composite design is employed. The full-factorial central composite design consists of a complete $2k$ factorial design, where k is the number of test variables; n_0 centre points ($n_0 \geq 1$) and two axial points on the axis of each design variable at a distance of α ($\alpha = 2^{k/4}$, $\alpha = 2$ for $k = 4$) from the design centre. Hence, the total number of design points is $N = 2^k + 2k + n_0$. A full-factorial central composite design (Sen and Swaminathan, 2004) is usually used to acquire data to fit an empirical second-order polynomial model. For four factors, the quadratic model takes the following form:

$$Y = b_0 + \sum_{i=1}^n b_i x_i + \left(\sum_{i=1}^n b_{ii} x_i \right) \sum_{i=1}^{2n-1} \sum_{j=i+1}^n b_{ij} x_i x_j \quad (2.16)$$

where Y is response variables, the coefficient b_0 is the free or offset term called intercept, b the regression coefficients of the model, x represents the coded levels of the independent variables. This regression model (Eq. 2.16) is a function of the sums of squares of the levels of the factors in that treatment combination and can well be used to estimate a response based on a particular process conditions.

2.4.6 Kinetic analysis

Langmuir–Hinshelwood (LH) kinetics model is the most commonly employed kinetic expression to explain the kinetics of the heterogeneous catalytic processes. The Langmuir–Hinshelwood expression that provides the explanation on the kinetics of heterogeneous catalytic systems can be expressed as follows (Guettai and Ait Amar, 2005).

$$r = -\frac{dC}{dt} = \frac{k_r K_{LH} C}{1 + K_{LH} C} \quad (2.17)$$

where r is the photoreduction rate of the reactant ($\text{mg L}^{-1} \text{min}$), K_{LH} is the adsorption coefficient of the reactant, k_r is the reaction rate constant ($\text{mg L}^{-1} \text{min}$) C is the concentration of the reactant (mg L^{-1}), and t is the illumination time.

Due to the formation of intermediates during photocatalytic reduction, interference in the determination of kinetics may occur related to the competitive adsorption and reduction. Therefore, calculations were performed at the beginning illuminated conversion. Any changes such as intermediates effects or pH changes can be neglected and the photocatalytic reduction rate expression is defined as:

$$r = -\frac{dC}{dt} = k_r \left(\frac{K_{LH} C_0}{1 + K_{LH} C_0} \right) \quad (2.18)$$

where r_0 is the initial photocatalytic reduction rate ($\text{mg L}^{-1} \text{min}$) and C_0 the initial concentration (mg L^{-1}) and K_{LH} is the adsorption equilibrium constant (L mg^{-1}). The equation can be simplified to an apparent first-order equation in cases where the chemical concentration C_i is very low (C_0 small) (Ollis, 1985):

$$\ln \frac{C_0}{C_t} = k_r k_t = k_{app} t \quad (2.19)$$

where C_t (mg L^{-1}) is the concentration of the 2-CP at time t (min) and C_0 (mg L^{-1}) is the initial concentration of the 2-CP.

Generally, the initial reduction rate can be deduced as follows:

$$r_0 = k_{app} C_0 \quad (2.20)$$

A plot of $\ln (C_0/C_t)$ versus illumination time represents a straight line, while the slope of which upon linear regression represent the apparent first order rate constant, k_{app} .

2.4.7 Mechanism of 2-CP Degradation

It has been established that the first process in 2-CP photo-oxidation may involves the hydroxylation at ortho position or scission of C-Cl bond. Figure 2.3 indicates possible degradation mechanism involving the hydroxylation as the first process as reported by Bandara *et al.* (2001a). If 2-CP is hydroxylated at the ortho

position, 2-chlorocatechol and catechol are formed. The para-dechlorination of 2-chlorocatechol yields 2-hydroxy-1,4-catechol.

In a similar way, if 2-CP is homolysed at ring-Cl bond, a short-lived hydroxyphenyl radical (HPR) is formed and may combine with proton to form phenol. Probably catechol is formed by o-hydroxylation of phenol. Further oxidative hydroxylation of catechol and phenol gives hydroxyhydroquinone and hydroquinone. Subsequently, hydroquinone and hydroxyhydroquinone are converted to benzoquinone hydroxybenzoquinone. Finally, quinone rings are opened to form aliphatic compounds which upon further oxidation are mineralised to CO₂ and H₂O.

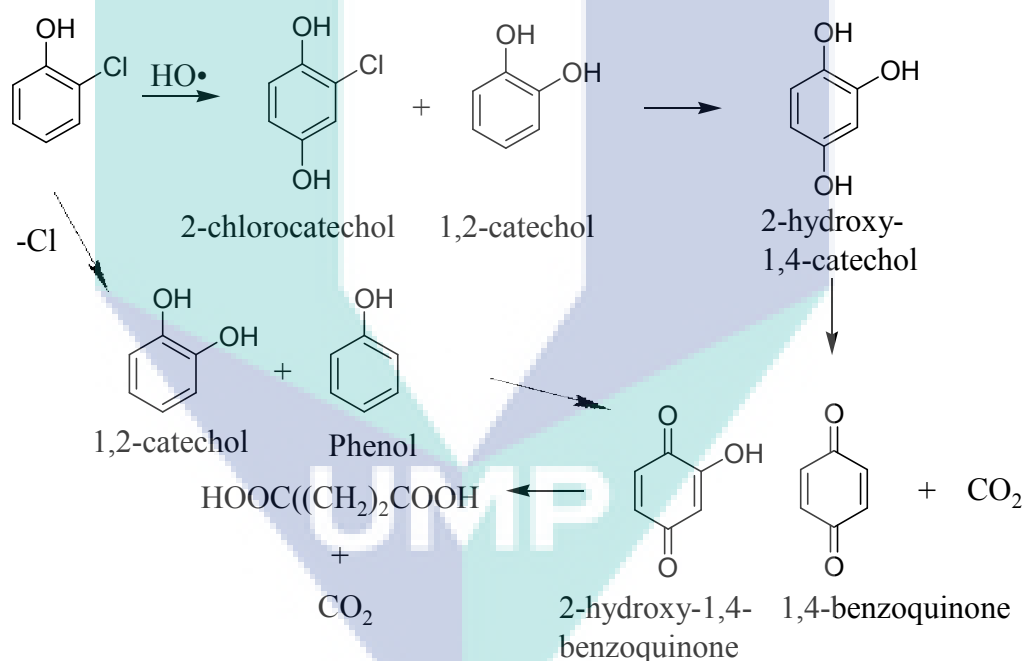


Figure 2.3 A mechanism to account for the pathways of photoproducts in the course of mineralisation of 2-CP (Bandara *et al.*, 2001a)

2.4.8 Scaling Up System

In order to reveal the feasibility of semiconductor photocatalysis for environmental remediation, degradation system is an equally vital factor. Research and development on efficient catalytic system intends to scale up laboratory bench scale processes to industrially practical applications. However, scaling up photocatalytic system is a complex process with many factors needing consideration to yield a economically and technically efficient process. In addition, the catalysts used in laboratory scale are not properly suitable for industrial scale applications and is still a matter of interest.

The issue of efficient photocatalyst illumination is particularly critical as this essentially determines the quantity of water that may be treated per unit area of deployed photocatalyst. A broad range of photocatalytic systems have been developed and used in both laboratory research and pilot scale studies. However, the provision of sufficient high specific surface area of catalyst is still the central problem of scale-up of photocatalytic systems. Nevertheless, it is possible to make precise predictions on the catalytic behavior of the catalysts on a pilot scale system to provide insight on its possible employments in large scale applications.

Bayarri *et al.*, (2013) had investigated the comparison on the system performance between the laboratory scale and pilot scale towards the degradation of 2,4-dichlorophenol. It was found that that although the degradation of target pollutant is higher at laboratory scale, the reaction rates for both scales are still similar. Meanwhile, Pereira *et al.*, (2011) study the comparison of the laboratory and pilot scale system on the photocatalytic degradation of oxytetracycline using TiO_2 . They reported that major difference between experiments in lab-scale and in pilot plant scale are regarded as reactor geometry, thus demonstrating that pilot scale system were more effective in the usage of accumulated UV energy to completely degrade the target pollutant.

2.5 Photocatalyst Synthesis and Modification

As aforementioned, photocatalytic process involves the presence of light radiation and a semiconductor catalyst. Material that able to conduct the electricity at room temperature but also act as an insulator is defined as semiconductor material. Based on their constituent atoms in the periodic table groups, the group of the materials is being classified. The transition metal ions can be reduced using semiconductor materials through photocatalysis process. As demonstrate in Figure 2.4, the band gap energy (E_g) is a difference between valence band hole (h_{VB}^+) and conduction band electron (e_{CB}^-). There is also worth noted that band gap is an area of prohibited energies in a perfect crystal (Litter, 1999).

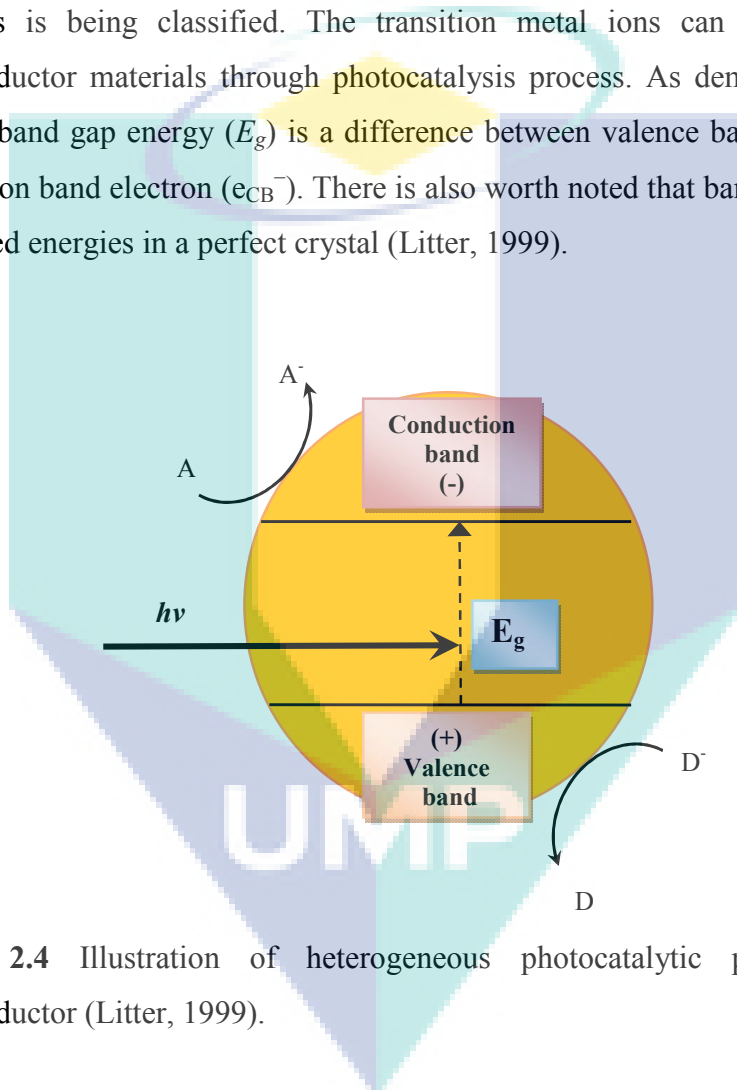


Figure 2.4 Illustration of heterogeneous photocatalytic processes on the semiconductor (Litter, 1999).

Once the valence band electron of semiconductor particles absorbs the photon of energy equal or larger than the catalyst band gap, the hole in valence band will be generated and the electron will jump to the conduction band ($h\nu \geq E_g$). Electron donor (D) or electron acceptor (A) may react or combine with the e_{CB}^- and h_{VB}^+ .

The semiconductors such as ZnO, SnO, TiO₂ and WO₃ were widely studied in the heterogeneous photocatalytic processes. TiO₂ is the photoactive catalyst which mostly being investigated for a long time due to the large band gap range. The TiO₂ has been studied in many forms such as pillars in the interlayer of clay minerals (Yoneyama, 1989), bulk material (Anpo, 1989) and colloid suspensions (Thomas, 1990).

2.5.1 α -FeOOH as Photocatalyst

α -FeOOH which an antiferromagnetic iron oxyhydroxide, have a band-gap of 2.2 eV (Hu *et al.*, 2012b). It is considered as one of the most environmentally friendly catalysts and it is known to be thermodynamically stable (Prasad *et al.*, 2006). α -FeOOH combines plausible properties for large-scale application such as resistance to photocorrosion, have wide range of operating pHs and almost undetectable leaching of iron into the solution. Other characteristics is that it is one of the most common forms of iron oxides found in oxisoils of temperate regions; it is one of the most chemically active compounds suspended in natural waters, it is widely used as a model compound in soil remediation, it has a low energy requirement, its catalytic activity is quite acceptable and most importantly, it can be operated with solar radiation.

Furthermore, according to the measured optical properties, reactors using the goethite catalyst were proven to have a much larger characteristic optical path length as compared with the most widely known photocatalytic reactions which employing titanium dioxide (Ortiz de la Plata *et al.*, 2008d). There are several studies that employed α -FeOOH as the catalyst for degradation of 2-CP (Table 2.2).

Table 2.1 Previous studies for 2-CP degradation using α -FeOOH

α -FeOOH particle size	2-CP concentration (mg/L)	pH	Catalyst dosage (g/L)	H ₂ O ₂ (mM)	2-CP degradation percentage (%)	Ref
75–150 μ m	50	3-4	0.50	11.7	99	Ortiz de la Plata <i>et al.</i> , 2010
0.08–0.15 mm	40	3	0.80	1.96	99	Lu <i>et al.</i> , 2002
0.074–0.044 mm	50	3	0.40	2.20	~99	Ming-Chun, 2000
600–900 μ m	50	3	0.20	2.20	~98	Gordon <i>et al.</i> , 2009
0.04–0.20 mm	50	-	2.00	20.0	~80	Ortiz de la Plata <i>et al.</i> , 2008
~0.05 mm	15	6.3	1.00	9.80	9	Huang <i>et al.</i> , 2001

It was found that many iron-oxides employed in a photo-Fenton-like system require strong acidic pH to have the fastest rates in solution (Ortiz de la Plata *et al.*, 2010a). These conditions introduce the need for acidification of the reacting medium and subsequent neutralization after treatment. Thus, nearly neutral conditions appear to be more favorable in employing a photo-Fenton-like system, so attempts should be made to conduct the system under mild pH conditions.

On the other hand, an insufficient amount or a disproportionate excess of H₂O₂ can result in negative effects in a photo-Fenton-like system. Some authors have conducted their work with H₂O₂ concentrations around 20.0 mM while others have used around 2.0 mM H₂O₂ (Ortiz de la Plata *et al.*, 2008d, Lu, 2000a, Lu *et al.*, 2002b). Since the selection of a reduced H₂O₂ concentration for the degradation of pollutants is important from a practical point of view due to the cost and toxicity of this compound, an attempt has been made in this study to investigate the behavior of the system and to reduce the amount of H₂O₂ required for efficient degradation.

2.5.2 Preparation of α -FeOOH

Precipitation method is the most commonly employed method for the synthesis of α -FeOOH (Cornell and Schwertmann, 2003). A portion of alkaline solution such as potassium hydroxide was mixed with the iron source solution and the mixture was stirred vigorously. The dispersion was aged for 48 h at 80°C. The precipitate was then centrifuged out and re-dispersed in an acidic solution, centrifuged again, and this procedure was repeated 10 times, and again three times, with distilled water. Then the precipitate were mixed together and freeze-dried. However, this method seems to be very time consuming and requires the use of surplus solvents.

The modification for the synthesis method for α -FeOOH has been reported by Chen *et al.* (2011) via ultrasonic-assisted hydrothermal method. The as-synthesized Fe nanopowders by electrical explosion method were immersed into distilled water and kept in a beaker under ultrasonically treatment at 85 °C. Subsequently, an acidic solution was dropped into the mixed solution at a constant flow rate. Finally, the resulting solid products were obtained with filtered off from the solution, washed with distilled water for several times, and dried in the vacuum dry chamber at 60 °C for 6 h. However, it was found that this method requires a very controlled environment and extreme careful observation. Therefore, other alternative method in synthesizing the α -FeOOH are still in demand.

2.5.3 Electrolysis as Preparation Method

Electrosynthesis process is a widely used especially in energy conversion and metal deposition. Furthermore, Aishah *et al.*, (2002) has proven that this technique may provide a clean and pure route for synthesizing nanoparticles. This method is a

good selection since the electron react a reducing agent which can contribute to low cost and effective reagent. In addition, this process has the capability to manage the characteristic of the product and the particle size is tunable in order to prepare the preferred product (Gao and Hao, 2009a).

The metals generated from the electrosynthesis process are nanosized particles with high purity compared to the conventional method. Therefore, the electrosynthesis is a promised technique in producing a bulk of metal nanoparticles. Other than that, this technique has other advantages related to the heterogeneous substrate–electrode electron transfer which allows the electron to directly transfer to or from the target molecule to perform oxidation or reduction, respectively.

Besides that, the electron can be accurately exchanged and controlled under extremely mild experimental conditions without any careful control. Electrolysis process has different selectivity from conventional synthesis since it offers a unique mechanistic pathway. The oxidizing or reducing power can be easily controlled by electrical potential of the electrode (Sultan and Tikoo, 1984).

It is well known that the electrode plays an important role in electrochemical process since there are main reactions that take place at the electrode during electrolysis (Tokuda *et al.*, 1993). Electrolysis process involves two electrodes. The cathode is for negatively charged where the reduction takes place while the anode is for positively charged which oxidation will occur. The electrodes are placed in a suitable distance to minimize the cell voltage and to ensure the flow of the current. The electrolyte is important in any electrolysis process which the most critical in ensuring the complete an electric circuit between two electrodes.

Electrosynthesis of α -FeOOH have been explored for few decades (Jiao *et al.*, 2009) since the size and yield of products may be easily controlled to some extent by adjusting the parameters of electrochemical reaction, such as voltage and

current density. Hashimoto and Cohen (1974) added anions such as phosphate, acetate, chloride, or sulfate in perchlorate solutions to electrodeposit the α -FeOOH. Leibenguth and Cohen (1972) synthesis α -FeOOH by anodic deposition from ferrous sulfate solutions of ferric oxide type films on a platinum substrate while Peulon (2007) electrodeposited α -FeOOH onto tin dioxide substrate (SnO_2). However, the surplus use of organic solvents urges the needs of investigating other alternatives in substituting the conventional solvents. In this scenario, cationic surfactant can be an alternative.

2.5.4 Cationic Surfactant as Electrolyte

Surfactants are usually defined as organic compounds that have amphiphilic behavior, which means that they have both hydrophobic groups, usually known as “tails”, and hydrophilic groups, which known as “head” (Figure 2.5). Therefore, a surfactant contains both water insoluble component and a water soluble component. Meanwhile, ionic surfactants are termed to the surfactants that carry a net charge at its head component. If the charge is positive, the surfactant is more specifically called cationic; if the charge is negative, it is called anionic. If a surfactant contains a head with two oppositely charged groups, it is usually named as zwitterionic.

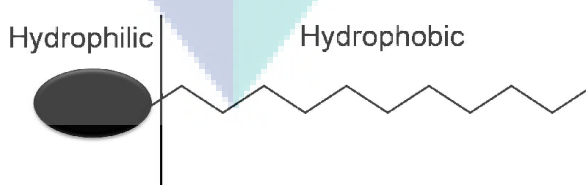


Figure 2.5 Illustration of surfactant showing hydrophilic (head) and hydrophobic (tail) components

Cationic surfactants have always sparked a researcher's interest due to their peculiar and interesting properties which include—contrasting hydrophobic and hydrophilic nature; tendency to self associate; ability to solubilize both polar as well as non polar components, etc. (Kaur and Mehta, 2014). They can be efficiently used as scaffolds for nanostructure materials or as mimics for natural products. The incorporation of various moieties, e.g. peptides, metals or even carbohydrates, etc. into the amphiphilic systems has led to the fabrication of numerous new classes of surfactants. Such systems possess the tendency to self-aggregate and form a variety of supramolecular assemblies.

Amongst all the classes of new amphiphilic complexes known, metallosurfactants or metal surfactant complexes have gained much attention in the recent past as they open up a vast arena of applications (Kaur and Mehta, 2014). Complexing metal ions to the conventional surfactant systems or ligands lead to the formation of metallosurfactants possessing unique properties. The complexes formed, possess not only the properties of metals such as acid–base, redox and magnetic properties but they also retain amphiphilic character, which usually important in terms of its surface activity. This basic idea of incorporation of a metal ion into the surfactant molecule provides a facile means of localizing both amphiphilic and metallic properties at the interface presenting a fascinating blend of organometallic chemistry and surface science.

Due to the conventional surfactant like properties, these metallic compounds are capable of forming aggregates of various sizes and morphologies including micelles, vesicles and bilayers incorporating metal ions. The aggregation behavior and self assembly of metallosurfactants have been studied for quite some time (Nikoobakht and El–Sayed, 2001). However, very little information is available on their possible role as nanosized reaction medium for the formulation of nanostructures.

2.5.5 Mesostructure Silica Nanoparticles (MSN) as Supporting Material

Support material for the metal oxides is an important aspect to be considered as it may give significant influence to the performance of the catalyst such as providing larger surface sites for the localization of the loaded metal, enhancing the recoverability of the catalyst as compared to the unsupported metal catalyst, and many more. As for α -FeOOH, there has been an increasing study on the supported α -FeOOH in these recent years. In 2012, Wang and co-workers (Wang *et al.*, 2012b) has supported the α -FeOOH on a diatomite for the degradation of dimethyl phthalate. More recent, α -FeOOH has been supported to a graphene oxide and has shown remarkable performance towards the reduction of Cr(VI) under visible light irradiation (Padhi and Parida, 2014).

The materials with pores in the range 20–500Å in diameter are grouped as mesostructure materials. They have huge surface areas and they have numerous applications in separation technology, catalysis, and many other fields. They are also often used as supporting materials for catalyst. Some kind of alumina and silica that have similarly-sized fine mesopores is known to be the typical mesostructure materials. Siliceous materials such as zeolite, silica, and clay are found widespread in the environment and they are commonly used for environmental contaminant remediation recently.

Mesostructure silicas, such as MCM-41 and SBA-15 silicas comprise of a honeycomb-like porous structure with hundreds of empty channels (mesopores). They are able to provide larger surface sites for photocatalysis activity. Many researchers have explored the functionalization and utilization of these materials since the discovery of surfactant-templated synthesis of mesostructure silica materials in 1992 and they have been oriented to various applications, such as catalysis, separation technology, and sensors.

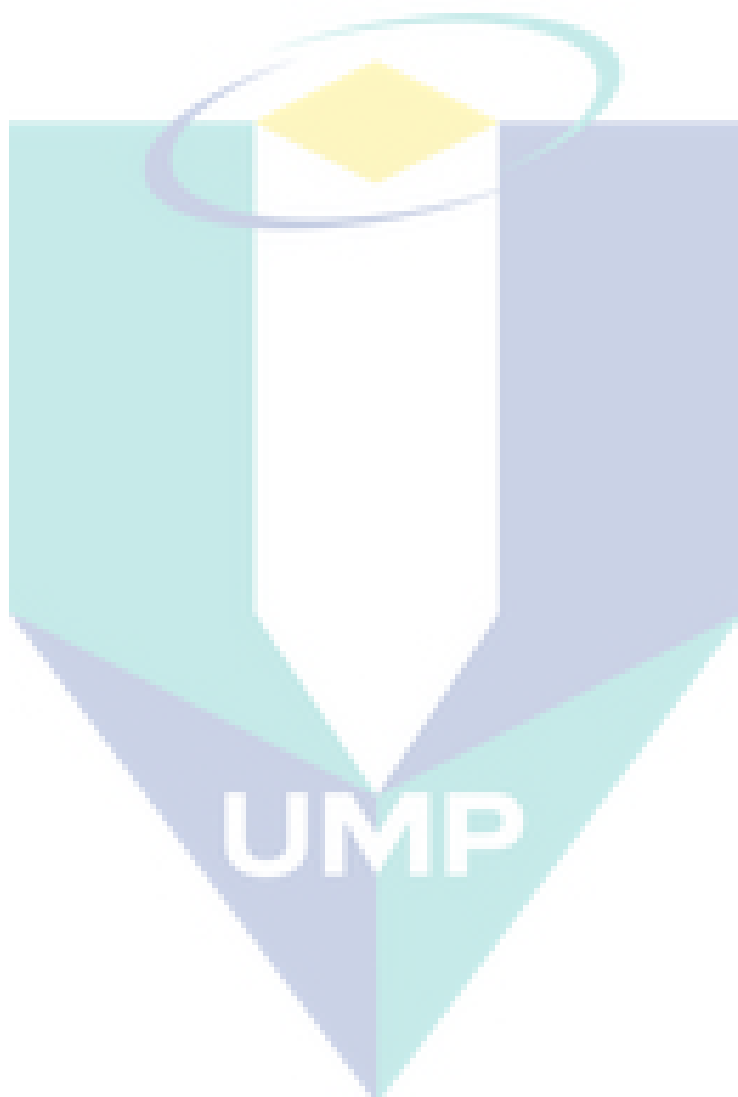
Meanwhile, Huh *et al.*, (2003) has developed a co-condensation synthesis technique which is a synthetic approach for preparing a series of mesostructure silica nanoparticle (MSN) materials. They took the benefit of the well-known synthesis of MCM-41, commonly used mesoporous silica materials, where TEOS was used as a silica source, a cationic surfactant cetyltrimethylammonium bromide (CTAB) as a structure directing agent, sodium hydroxide was used as a morphological catalyst, and water was used as solvent.

Recently, mesostructure materials as support material have been attracted interest due to their high surface area, assessable pore channels, simple pore chemistry with promising powder recoverability (Deng *et al.*, 2011). Moreover, better light-induced hydrophobicity was proven by mesoporous-assembled structure with incorporation of metal catalyst which then exhibiting higher photocatalytic activities than non-mesoporous-assembled catalyst (Puangpetch *et al.*, 2010).

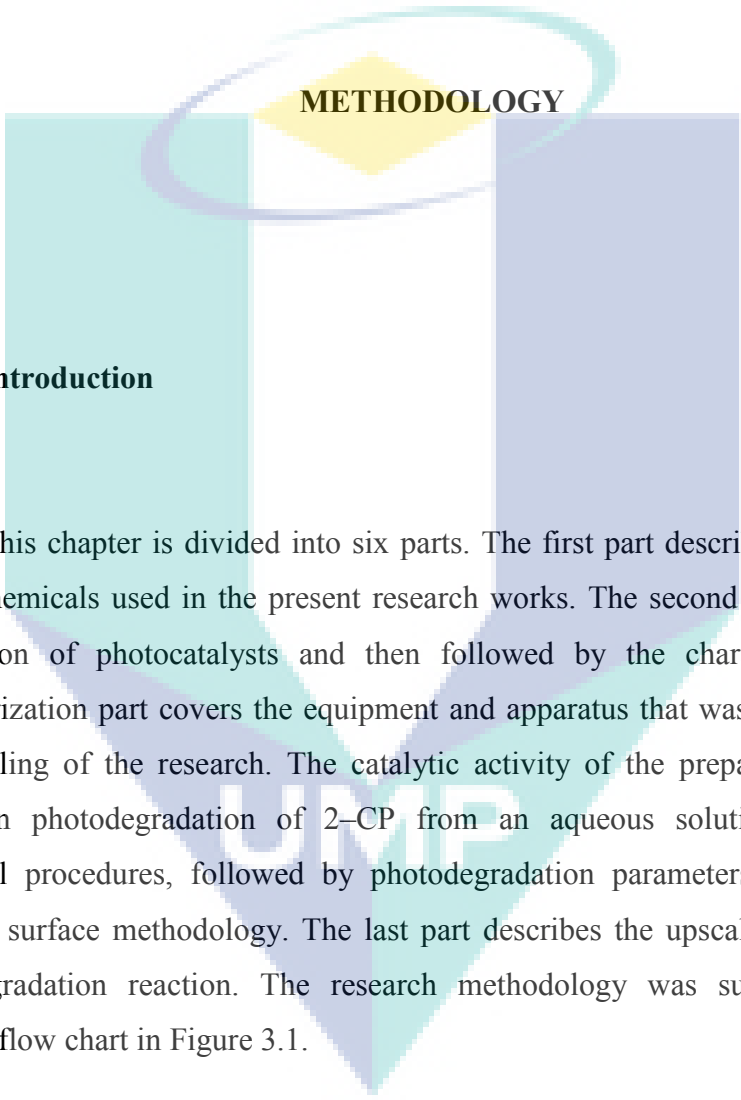
2.6 Summary

A review of recent studies has revealed that the electrosynthesized catalysts may exhibit better performance and photocatalytic activity. Although several heterogeneous photocatalysts have been extensively studied, they may have several disadvantages related to its unsuitable operating conditions from practical point of view due to the cost and toxicity. Thus, electrosynthesized α -FeOOH which seems to be the best candidate is expected to reduce the electron-hole recombination that could enhance the capability of the photocatalyst to be used in the visible light conditions. The use of mesoporous materials such as MSN a support for the metal oxide have attracted great interest due to the improved powder recoverability and large surface area which able to provide high distribution of iron oxides for enhanced photodegradation activity. Moreover, the study on the interaction of electrosynthesized metal oxide in cationic surfactants with a mesostructured silica

nanoparticles support is still rare. The properties of the catalyst are known to be strongly affected by the support, which makes it very complicated to understand its reaction mechanism. Thus, detail investigation on supported metal catalyst is very crucial.



CHAPTER 3



METHODODOLOGY

3.1 Introduction

This chapter is divided into six parts. The first part describes the particulars of the chemicals used in the present research works. The second part describes the preparation of photocatalysts and then followed by the characterizations. The characterization part covers the equipment and apparatus that was employed during the handling of the research. The catalytic activity of the prepared catalysts was tested on photodegradation of 2-CP from an aqueous solution including the analytical procedures, followed by photodegradation parameters optimization by response surface methodology. The last part describes the upscaling system of the photodegradation reaction. The research methodology was summarized in the research flow chart in Figure 3.1.

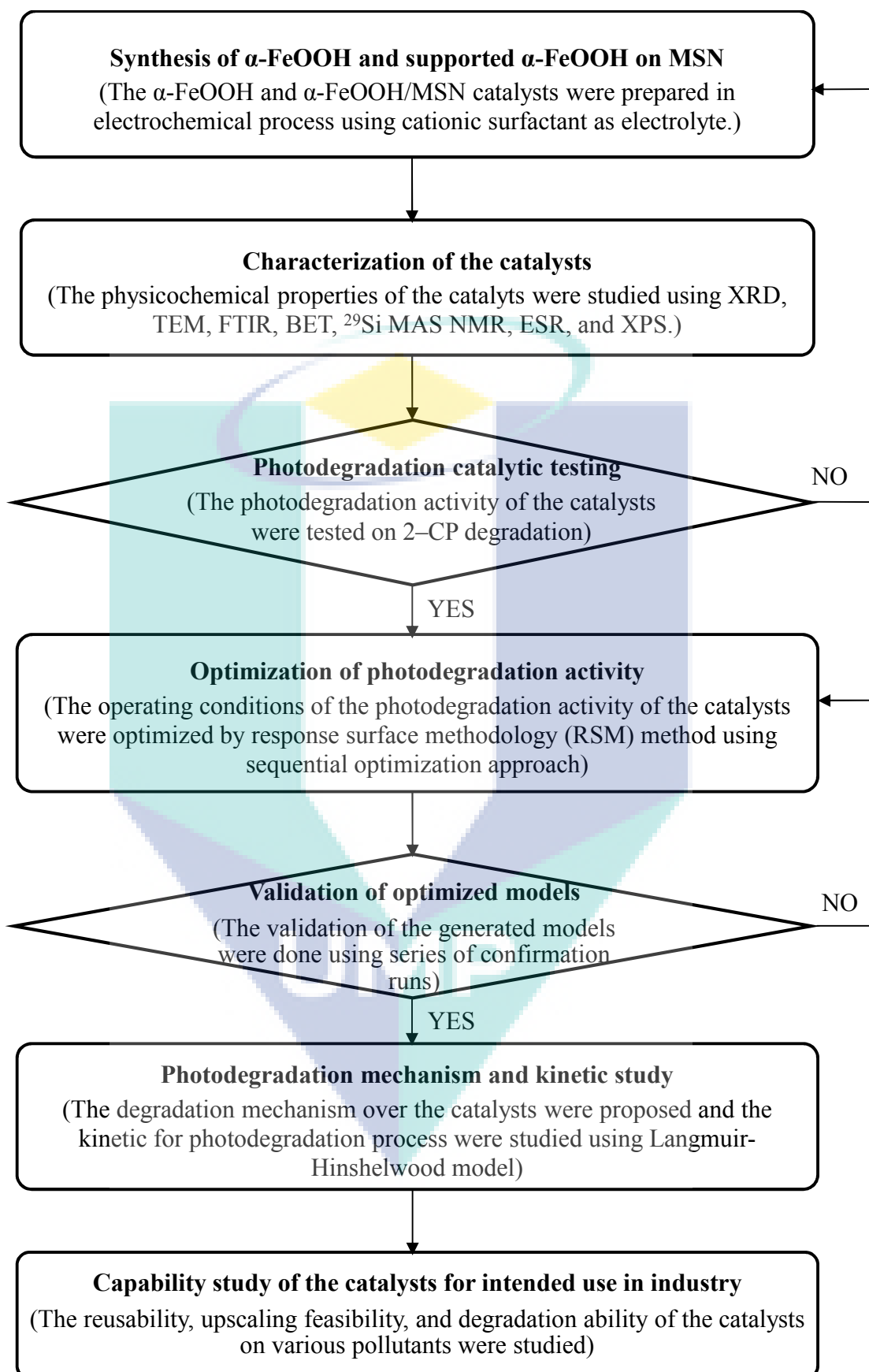


Figure 3.1 Flow chart of the research activity

3.2 Materials

The chemicals used for this study are listed in Table 3.1. The purity of the chemicals and the company supplying the chemicals are also presented.

Table 3.1 List of chemicals

Chemicals	Purity	Brand	Usage
2-Chlorophenol (2-CP)	99.9%	Alfa Aesar	Photodegradation
Dodecyltrimethylammonium bromide (DTABr)	>98%	Acros Organics	Synthesis
Cetyltrimethyl ammonium bromide (CTAB)	>98%	Merck Sdn Bhd	Synthesis
Ethylene glycol (EG)	>98%	Merck Sdn Bhd	Synthesis
Tetraethylorthosilicate (TEOS)	>98%	Merck Sdn Bhd	Synthesis
3-aminopropyl triethoxysilane (APTES)	>98%	Merck Sdn Bhd	Synthesis
Ammonium nitrate (NH ₄ NO ₃)	99.9%	Merck Sdn Bhd	Synthesis
Ammonium hydroxide solution (NH ₄ OH)	99.9%	QReC	Synthesis
Ethanol (EtOH)	99.9%	QReC	Synthesis
Sodium hydroxide (NaOH)	99.9%	QReC	Photodegradation
Hydrochloric acid (HCl)	99.9%	QReC	Photodegradation

3.3 Catalyst Preparation

The preparation method of the catalysts were explained in detail in this section including the preparation of supporting material (MSN), electrosynthesized

goethite (α -FeOOH) and the α -FeOOH incorporated with MSN support material (α -FeOOH/MSN).

3.3.1 Preparation of Mesoporous Silica Nanoparticles (MSN)

MSN was prepared by co-condensation method. CTAB which act as the surfactant was dissolved in a solution containing water, EG, and ammonia aqueous solution. Addition of EG into the mixture is to control the particle size and morphology and also to improve the structural order. After vigorous stirring, TEOS was added to the mixture to act as silica source. Then, the resulting solution was stirred for another 2 hours at 50°C and was kept statically at the same temperature for 3 hours. Samples were centrifuged, washed, and dispersed again with distilled water and absolute ethanol for 5 times. Next, the solid (gel) collected was dispersed in a mixture of NH_4NO_3 and ethanol in order to remove the surfactant template. The mixture was heated for 3 hours with temperature 60°C. Next, the mixture was separated by centrifugation and was washed for 3 times. The product in solid (gel) phase was dried in oven at 110°C overnight followed by calcinations in air at 550°C. A pore expander, 3-aminopropyl triethoxysilane (APTES), was also used to show the discrepancy in the pore size of MSN and its effects towards the loading of α -FeOOH (Karim *et al.*, 2012).

3.3.2 Preparation of α -FeOOH

α -FeOOH nanoparticles was synthesized by electrochemical process using cationic surfactant as electrolyte. The process was performed in one-compartment cell equipped with a magnetic stirring bar and two-electrode configuration. An iron plate (2 cm \times 2 cm) anode and a platinum plate (2 cm \times 2 cm) cathode were carefully

cleaned using 1.0 M HCl followed by deionized water before used as electrodes. The electrodes were placed in parallel with a distance of 2.0 cm and were inserted into the 15 mL DTABr cationic surfactant/water solution, with volume ratio of DTABr to water is 1:1. Then electrolysis was conducted at a constant current of 60 mA/cm^2 and 0°C under air atmosphere. After electrolysis, the mixture was heated at 80°C in an oil bath before being dried overnight at 110°C to give a brown-colored $\alpha\text{-FeOOH}$ powder. The schematic diagram for the electrolysis cell is shown in Figure 3.2.

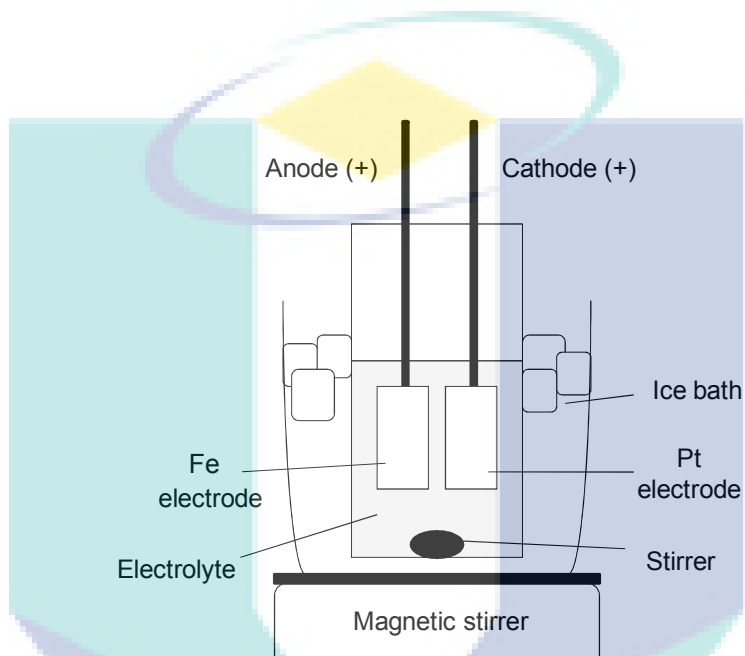


Figure 3.2 Schematic diagram of electrolysis cell

3.3.3 Preparation of $\alpha\text{-FeOOH/MSN}$

The $\alpha\text{-FeOOH/MSN}$ was prepared by ion-exchange electrolysis method (Figure 3.2). For the in situ preparation technique, a 15 mL of DTABr was added to a one-compartment cell fitted with a platinum plate cathode ($2 \text{ cm} \times 2 \text{ cm}$) and an iron plate anode ($2 \text{ cm} \times 2 \text{ cm}$). Then, the electrolysis was conducted at a constant current of 60 mA/cm^2 and 0°C under ambient condition with continuous stirring. The

required iron loading on the MSN support was calculated based on Faraday's law of electrolysis, as shown in the following equation,

$$n = \left(\frac{It}{F} \right) \left(\frac{1}{z} \right) \quad (3.1)$$

where n is the number of moles of Fe, I is constant current of electrolysis (A), t is the total time the constant current was applied (s), F is the Faraday constant ($96,487 \text{ C mol}^{-1}$), and z is the valency number of ions of the substance (electron transferred per ion). The number of moles of Fe required was calculated based on the total time t of the electrolysis. After electrolysis, the required α -FeOOH loading mixture was impregnated at 80°C with the as-prepared MSN, followed by oven-drying at 110°C overnight to give a brown-colored α -FeOOH/MSN catalyst. To investigate the effect of different metal loading loaded to MSN, a series of different percentage of α -FeOOH was prepared which are 5, 10 and 15 wt% of α -FeOOH loading.

3.4 Catalyst Characterization

3.4.1 Crystallinity, Phase and Structural Studies

The identity and crystallinity of α -FeOOH and α -FeOOH/MSN was confirmed by X-ray diffraction (XRD) recorded on a D8 Advanced Bruker X-ray diffractometer. The diffracted monochromic beam is at 40 kv and 40 mA with $\text{Cu K}\alpha$ ($\lambda = 1.5418 \text{ \AA}$) radiation. The data was collected at room temperature with a range of $2\theta = 2\text{--}90^\circ$. The scan rate would be 0.025° continuously.

3.4.2 Morphological Properties

The morphology and size of the synthesized catalyst was observed using TEM. The TEM characterization was carried out by employing JEOL JEM-2100F. For the TEM observations, a powder sample was dissolved in hexane and dropped onto the copper grid.

3.4.3 Vibrational Spectroscopy

The FTIR spectra was analyzed by using Perkin Elmer Spectrum GX FT-IR in a range of 400 to 4000 cm^{-1} to determine the functional groups of the catalysts. The characterization method was employed KBr pellet technique. The catalyst was mixed with KBr at approximately 1 to 3 % by weight before being grounded into powder. Then, the powder mixture was pressed in hydraulic press (8 tons) in order to form a thin pellet. The spectra were recorded at room temperature with an 8 cm^{-1} spectral resolution with accumulation of 5 scans in open beam air background.

3.4.4 Study of Textural Properties

The nitrogen adsorption characterization was employed to analyze the surface area of the catalysts. The adsorbate for this characterization apparatus is 77 K nitrogen gas. 0.05 g of sample will be dehydrated for 3 hours at 473 K before the measurement is performed. The dehydrated sample was then weighted and after that, the sample will be evacuated to 10–20 Torr followed by absorption in liquid

nitrogen. The sample BET surface area was automatically calculated from nitrogen adsorption data.

3.4.5 Chemical Environment Determination

²⁹Si MAS NMR experiments were carried out to study the chemical environments of the silicon atoms of the synthesized catalysts. ²⁹Si MAS NMR spectra were recorded on a Bruker Avance 400 MHz 9.4T spectrometer at frequency of 104.2 MHz. The spectra were recorded using 4 μs radio frequency pulses, a recycle delay of 60 s and spinning rate of 7 kHz using a 4 mm zirconia sample rotor.

3.4.6 Chemical Oxidation State Determination

The X-Ray photoelectron spectroscopy (XPS) was employed to identify the chemical oxidation state of synthesized catalysts. The measurement was performed in the range of 0 to 800 eV using a Kratos Ultra spectrometer equipped Mg K_α radiation source (10 mA, 15 kV). The powdered sample was pressed by using small Inox cylinder. Then, the sample was analyzed inside an analysis chamber pressure at about 1×10^{-10} Pa. As to correct the energy shift, the binding energy of the C (1s) at peak 284.5 ± 0.1 eV was taken as internally standard or reference as the solution.

JEOL JES-FA100 ESR spectrometer was utilized to determine the magnetism of the catalysts. The sample was placed height inside the glass vessel at about 2 cm. Then, the measurement which to identify the *g*-value was carried out at room temperature.

3.5 Catalytic Activity

3.5.1 Preparation of 2-CP Solution

The preparation of 2-CP solution was started by preparing the stock solution. The 1000 mL of 500 mg L⁻¹ 2-CP was prepared from the 99.9% initial 2-CP substance. Then, the stock solution was diluted to the desired concentration in a 1000 mL volumetric flask. The purity of prepared 2-CP solution is expected to be 100%.

3.5.2 Photoreactor System

A Pyrex batch photoreactor, 140 mm length and 85 mm diameter with a total volume of 0.25 m³ containing Philips TL 20W/52 fluorescent lamp within quartz glass housing (emission spectrum 350–600 nm) with a peak emission at 430 nm and a stirrer was used to determine the photocatalytic ability of the catalyst. Water bath was employed to provide the temperature control. Solution was stirred at 250 rpm. The entire set-up was placed inside a chamber covered with aluminum foil to prevent the passage of other lights into the reactor.

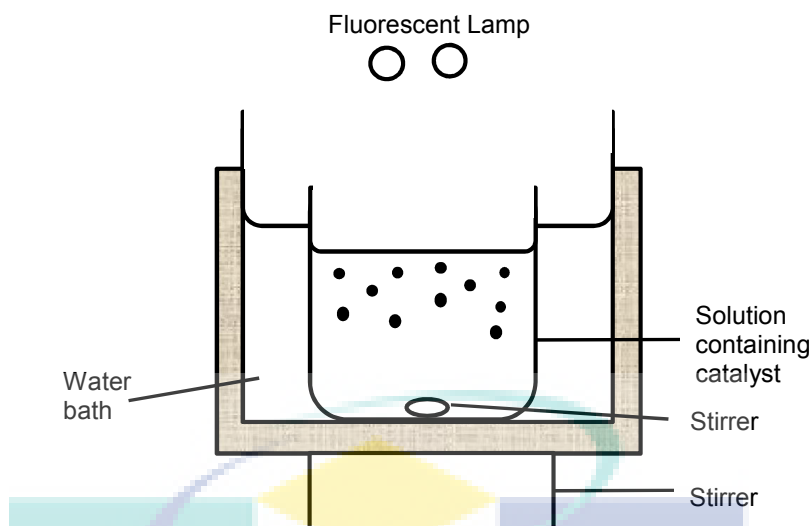


Figure 3.3 Schematic diagram of laboratory scale photoreactor

3.5.3 Photodegradation Activity

The photocatalytic degradation of 2-CP was tested using 0.03 g L^{-1} photocatalyst in 200 mL of 2-CP solution. For the effect of pH, a series of pH solutions of 3, 5, and 7 was used. Meanwhile, the effect of 0.02, 0.03, 0.04, and 0.05 g L^{-1} of catalyst dosage were also studied. H_2O_2 concentration of 0.10, 0.15, 0.20, and 0.50 mM was used to study the effect of H_2O_2 concentration. In addition, 10, 30, 50, and 70 mg L^{-1} of were used to study the effect of the 2-CP initial concentration.

The solution was stirred on a shaker at 250 rpm in dark condition for two hours to reach adsorption/desorption equilibrium. Then, the first sample was taken before being transferred into a centrifuged tube. The tube was covered with aluminium foil to avoid samples to undergo any absorption catalyzed by surrounding light.

Then, the solution was exposed to irradiation from the fluorescent lamps. The samples were taken and treated in the same procedure for every 15 minutes until the process reach its plateau. The samples were centrifuged using Hettich Zentrifugen Micro 120 at 75, 000 rpm for 15 minutes. The remaining sample concentrations of 2-CP in the solution was determined by measuring its absorbance using a double-beam UV-Vis spectrophotometer (Cary 60 UV-Vis Agilent) at 274 nm. The percentage of photocatalytic degradation was calculated by Eq. 3.2.

$$\text{Degradation (\%)} = \frac{C_0 - C_t}{C_0} \times 100 \quad (3.2)$$

where C_0 is the initial 2-CP concentration and C_t is the concentration of chlorophenol at time t .

3.6 Optimization of Process Conditions

RSM is a statistical method that uses quantitative data from appropriate experiments to determine regression model equations and operating conditions. RSM is a collection of mathematical and statistical techniques for modeling and analysis of problems in which a response of interest is influenced by several variables. A RSM design called full factorial was applied to screen the significance variables and to analyze the interaction between the parameters in this study, and then, RSM design called CCD was applied to optimize the effective parameters with a minimum number of experiments. The dependant variables selected for this study was selected based on the results from the preliminary experiments using traditional trial-and-error method. The response was selected as the degradation percentage of 2-CP and it will be used to develop an empirical model which correlated the response to the dependent variables.

To identify the important operating variables, a two-level factorial design was employed. A total of four independent variables, $k = 4$ which are temperature (X_1), catalyst dosage (X_2), $H_2O_2/2-CP$ ratio (X_3), and pH (X_4) were selected for the α -FeOOH and metal loading (A), pH (B), H_2O_2 concentration (C), catalyst dosage (D), and temperature (E) were selected for α -FeOOH/MSN catalyst. Each variable was represented at two levels, high (+) and low (–) as shown in Tables 3.2 and 3.3, with two replicates at four center points. The 2-CP degradation percentage (%) was taken as response parameters. The effect of each variable, sum of squares, mean square, F -value, P -value and confidence level (%) were determined using the statistical software package Design-Expert (Version 7.0.3, State-Ease, Minneapolis, USA). The generated factorial design of experiments are for both catalysts are depicted in Table 3.4 and Table 3.5.

Table 3.2 Variables showing operating conditions used in two-level factorial design employing α -FeOOH photocatalyst

Variables	Operating conditions	–values	+ values
X_1	Temperature ($^{\circ}C$)	30	50
X_2	Catalyst dosage ($g L^{-1}$)	0.25	0.38
X_3	$H_2O_2/2-CP$ ratio	0.2	0.6
X_4	pH	3	7

Table 3.3 Variables showing operating conditions used in two-level factorial design employing α -FeOOH/MSN photocatalyst

Variables	Operating conditions	–values	+ values
A	Metal loading (wt%)	5	15
B	pH	3	7
C	H_2O_2 concentration (mM)	0.1	0.2
D	Catalyst dosage ($g L^{-1}$)	0.2	0.6
E	Temperature ($^{\circ}C$)	30	50

Table 3.4 Two-level factorial design of experiments of four variables employing α -FeOOH photocatalyst

Run	Variables			
	X ₁	X ₂	X ₃	X ₄
1	50	0.25	0.2	3
2	40	0.31	0.4	5
3	40	0.31	0.4	5
4	30	0.38	0.2	7
5	50	0.25	0.2	7
6	30	0.38	0.2	3
7	50	0.25	0.6	7
8	50	0.38	0.6	7
9	30	0.25	0.2	3
10	40	0.31	0.4	5
11	30	0.38	0.6	7
12	30	0.38	0.6	3
13	30	0.25	0.6	7
14	50	0.38	0.6	3
15	50	0.38	0.2	7
16	50	0.25	0.6	3
17	30	0.25	0.2	7
18	30	0.25	0.6	3
19	40	0.31	0.4	5
20	50	0.38	0.2	3

Table 3.5 Two-level factorial design of experiments using α -FeOOH/MSN catalyst

Run	Variables				
	A	B	C	D	E
1	5	3	0.1	0.2	30
2	15	3	0.1	0.2	30
3	5	7	0.1	0.2	30
4	15	7	0.1	0.2	30
5	5	3	0.2	0.2	30
6	15	3	0.2	0.2	30
7	5	7	0.2	0.2	30
8	15	7	0.2	0.2	30
9	5	3	0.1	0.6	30
10	15	3	0.1	0.6	30

Continued

Run	Variables				
	A	B	C	D	E
11	5	7	0.1	0.6	30
12	15	7	0.1	0.6	30
13	5	3	0.2	0.6	30
14	15	3	0.2	0.6	30
15	5	7	0.2	0.6	30
16	15	7	0.2	0.6	30
17	5	3	0.1	0.2	50
18	15	3	0.1	0.2	50
19	5	7	0.1	0.2	50
20	15	7	0.1	0.2	50
21	5	3	0.2	0.2	50
22	15	3	0.2	0.2	50
23	5	7	0.2	0.2	50
24	15	7	0.2	0.2	50
25	5	3	0.1	0.6	50
26	15	3	0.1	0.6	50
27	5	7	0.1	0.6	50
28	15	7	0.1	0.6	50
29	5	3	0.2	0.6	50
30	15	3	0.2	0.6	50
31	5	7	0.2	0.6	50
32	15	7	0.2	0.6	50
33	10	5	0.15	0.4	40
34	10	5	0.15	0.4	40
35	10	5	0.15	0.4	40
36	10	5	0.15	0.4	40

For the optimization of screened variables, the full-factorial central composite design consists of a complete $2k$ factorial design, where k is the number of test variables; n_0 centre points ($n_0 \geq 1$) and two axial points on the axis of each design variable at a distance of α ($\alpha = 2^{k/4}$, $\alpha = 2$ for $k = 4$) from the design centre (Khuri and Cornell, 1987). Hence, the total number of design points is $N = 2^k + 2k + n_0$. A central composite design is usually used to acquire data to fit an empirical second-order polynomial model (Sen and Swaminathan, 2004). The quadratic model takes the following form:

$$Y = b_0 + \sum_{i=1}^n b_i x_i + \left(\sum_{i=1}^n b_{ii} x_i \right) \sum_{i=1}^{2n-1} \sum_{j=i+1}^n b_{ij} x_i x_j \quad (3.3)$$

where Y is response variables, the coefficient b_0 is the free or offset term called intercept, b the regression coefficients of the model, X represents the coded levels of the independent variables.

The statistical software package Design-Expert (Version 7.0.3, State-Ease, Minneapolis, USA) with the layout of central composite design was used to design and analyze the experiment. The actual values for the variables at various levels of the α -FeOOH and α -FeOOH/MSN catalysts are given in Table 3.6 and Table 3.7, respectively.

Table 3.6 Central composite design (CCD) design of experiments employing α -FeOOH photocatalyst

Run	Variables		
	X ₁	X ₂	X ₃
1	30	0.38	0.6
2	50	0.38	0.2
3	50	0.25	0.6
4	30	0.38	0.2
5	30	0.25	0.6
6	40	0.31	0.4
7	40	0.31	0.4
8	30	0.38	0.6
9	30	0.25	0.2
10	30	0.38	0.2
11	40	0.31	0.4
12	50	0.38	0.6
13	50	0.25	0.6
14	40	0.31	0.4
15	50	0.25	0.2
16	50	0.38	0.6
17	30	0.25	0.2

Continued

Run	Variables		
	X ₁	X ₂	X ₃
18	50	0.38	0.2
19	30	0.25	0.6
20	50	0.25	0.2
21	30	0.31	0.4
22	40	0.25	0.4
23	40	0.31	0.6
24	40	0.31	0.4
25	40	0.31	0.4
26	40	0.31	0.4
27	40	0.38	0.4
28	40	0.31	0.2
29	50	0.31	0.4

Table 3.7 Central composite design (CCD) design of experiments employing α -FeOOH/MSN photocatalyst

Run	Variables			
	A	B	C	D
1	5	3	0.1	30
2	5	3	0.1	30
3	15	3	0.1	30
4	15	3	0.1	30
5	5	7	0.1	30
6	5	7	0.1	30
7	15	7	0.1	30
8	15	7	0.1	30
9	5	3	0.2	30
10	5	3	0.2	30
11	15	3	0.2	30
12	15	3	0.2	30
13	5	7	0.2	30
14	5	7	0.2	30
15	15	7	0.2	30
16	15	7	0.2	30
17	5	3	0.1	50
18	5	3	0.1	50

Continued

Run	Variables			
	A	B	C	D
19	15	3	0.1	50
20	15	3	0.1	50
21	5	7	0.1	50
22	5	7	0.1	50
23	15	7	0.1	50
24	15	7	0.1	50
25	5	3	0.2	50
26	5	3	0.2	50
27	15	3	0.2	50
28	15	3	0.2	50
29	5	7	0.2	50
30	5	7	0.2	50
31	15	7	0.2	50
32	15	7	0.2	50
33	10	5	0.15	40
34	10	5	0.15	40
35	10	5	0.15	40
36	10	5	0.15	40
37	5	5	0.15	40
38	15	5	0.15	40
39	10	3	0.15	40
40	10	7	0.15	40
41	10	5	0.1	40
42	10	5	0.2	40
43	10	5	0.15	30
44	10	5	0.15	50
45	10	5	0.15	40
46	10	5	0.15	40
47	10	5	0.15	40
48	10	5	0.15	40

3.7 Scale-Up Process

The pilot-scale reactor consists of a 2000 mL batch tank and a platform for mounted irradiation source as shown in Figure 3.4. Philips TL 20W/52 fluorescent lamp within quartz glass housing (emission spectrum 350–600 nm) with a peak emission at 430 nm and a mounted stirrer was used to determine the photocatalytic ability of the catalyst. Water bath was employed to provide the temperature control. The solution consists of 2000 mL 2-CP aqueous solution at 50 mg L^{-1} with 0.4 g L^{-1} catalyst and the experiment was done using the best operating conditions determined by laboratory-scale experiments and by using the same procedures as in the laboratory-scale experiments, depicted in Section 3.5. The generated RSM models for both catalysts were employed. The performance of the catalyst activity for laboratory-scale and pilot-scale was compared and discussed.

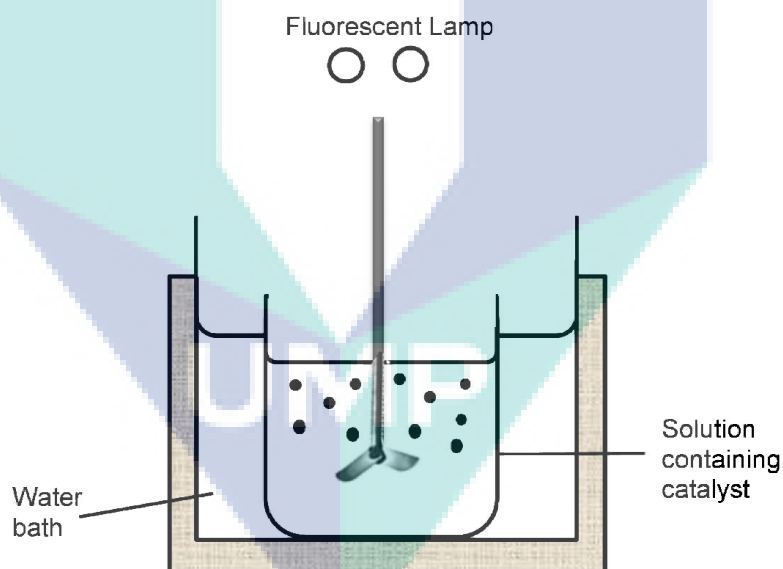


Figure 3.4 Schematic diagram of pilot scale photoreactor

CHAPTER 4

RESULTS AND DISCUSSION

4.1 Introduction

In this chapter, the synthesis and characterization of α -FeOOH nanoparticles and α -FeOOH supported mesostructured silica nanoparticles (MSN) photocatalysts which denoted as α -FeOOH and α -FeOOH/MSN, respectively were established in details. Then, the photodegradation performance evaluations were discussed that reflected to the characterization data and the photodegradation mechanism of the photocatalysts was proposed. The optimization of photodegradation parameters was conducted and the kinetic analysis of the photodegradation reaction was performed. The capability study of the catalysts for industrial applications was also studied including its reusability, upscaling feasibility, and degradation ability on various pollutants.

4.2 Synthesis and Characterization of α -FeOOH and α -FeOOH/MSN

This section described and discussed in details the synthesis and characterizations of α -FeOOH nanoparticles and α -FeOOH supported mesostructured silica nanoparticles (MSN) photocatalysts that were done by XRD, TEM, FT-IR, BET, ^{29}Si MAS NMR, ESR, and XPS.

4.2.1 Crystallinity, Phase and Structural Studies

Figure 4.1 illustrates the XRD pattern of synthesized α -FeOOH nanoparticles. The pattern reveals that diffraction peaks corresponding to (020), (110), (120), (021), (111), (121), (140), (151), and (161) planes match very well with those of bulk α -FeOOH (JCPDS file No. 81-0462), which proves that the nanoparticles collected from the electrolysis cell are pure orthorhombic phase α -FeOOH without any impurities.

The d -spacing observed for the strong (110) facet was 0.418 nm, and this is identical with the facet reported in the literature (Cornell and Schwertmann, 2003). This facet is predicted to have a great tendency to be bound with the cationic surfactant due to its high surface energy (Nikoobakht and El-Sayed, 2001).

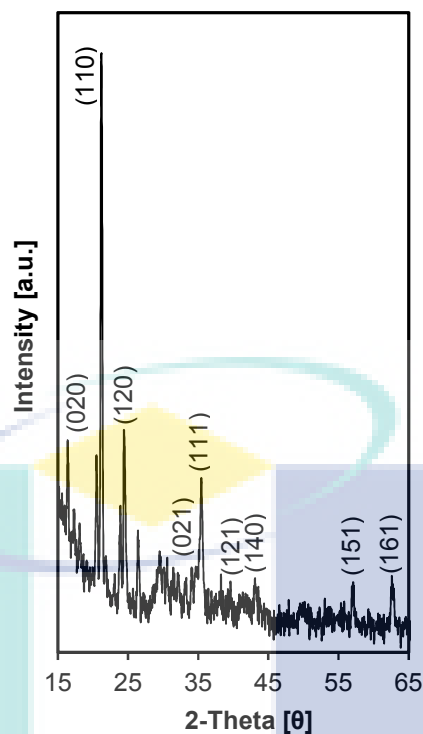


Figure 4.1 XRD patterns of α -FeOOH nanoparticles

For α -FeOOH loaded pristine MSN, three main diffraction peaks indexed as (100), (110), and (200) reflections were observed, which corresponded to $p6mm$ hexagonal symmetry in the mesostructured silica, demonstrating a high quality of mesopore packing (Kamarudin *et. al.*, 2014) (Figure 4.2). Introduction of α -FeOOH onto MSN inhibit the formation of the (100) peak, while the other two peaks were almost eliminated, signifying slight loss in MSN hexagonal structure ordering (Lang *et. al.*, 2002). The absence of α -FeOOH diffraction peaks in α -FeOOH /MSN may be due to the very small number of α -FeOOH species that are undetectable with XRD (Setiabudi *et. al.*, 2012).

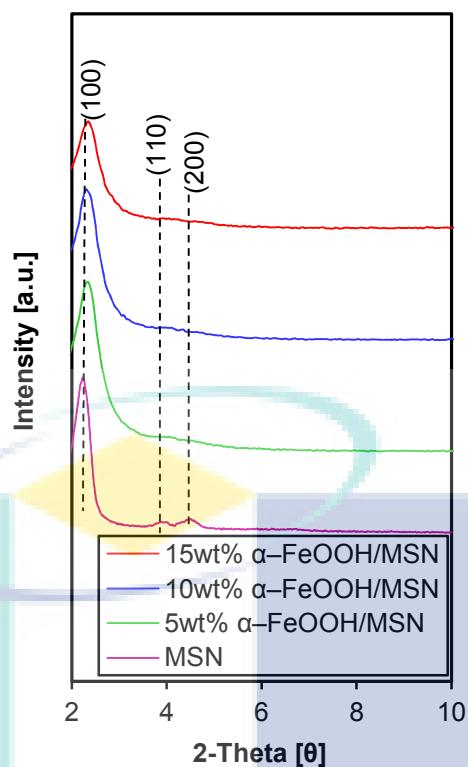


Figure 4.2 XRD patterns in region 2–10° of MSN and α -FeOOH/MSN catalysts at different α -FeOOH loading

The α -FeOOH was then loaded to the APTES-modified MSN (MSN_{APTES}) to study the effect of pore expander of the support towards the α -FeOOH loading. The XRD of the catalyst was compared with the pristine MSN and the α -FeOOH loaded pristine MSN catalyst (Figure 4.3). From the intensities of the (100) peak of the MSN_{APTES}, it was found that MSN_{APTES} had a greater pore order than pristine MSN. This may be due to the MSN modification by APTES which expanded the pore channels of MSN_{APTES}.

A similar observation was reported by Aziz *et al.*, (2014) who studied the difference between MSN and MCM-41. They found that MSN had a greater pore size than MCM-41 based on the XRD peak at (100). Meanwhile, the introduction of α -FeOOH into both MSNs retained the hexagonal structure of the MSNs. However, the formation of the (100) peak was slightly inhibited, while the other two peaks

were almost eliminated, signifying a slight loss in MSN hexagonal structural ordering (Lang *et. al.*, 2002).

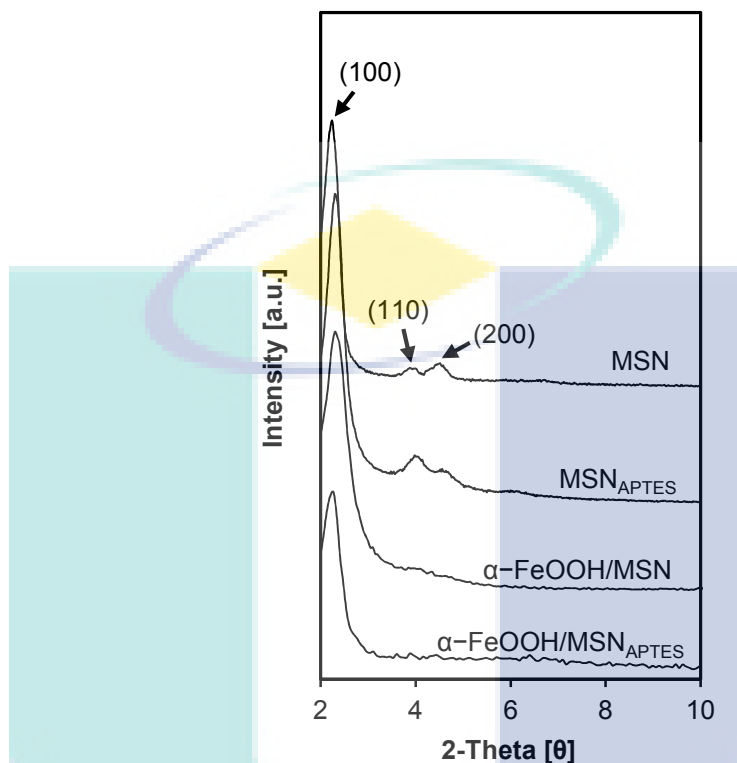


Figure 4.3 XRD patterns in region 2–10° of MSN_{APTES} and α-FeOOH/MSN_{APTES} catalysts as compared to its pristine catalysts

4.2.2 Morphological Properties

Figure 4.4 represents the TEM micrograph of the α-FeOOH nanocatalyst. Nearly spherical nanoparticles were clearly observed with a diameter range of 5–10 nm (Figure 4.4A and Figure 4.4B). The size of α-FeOOH nanoparticles was obviously much smaller than those of synthesized α-FeOOH commonly reported in the literature, which were mostly > 20 nm (Rădițoiu *et. al.*, 2012, Song and Zhang,

2009), signifying the use of cationic surfactant as electrolyte inhibited the growth of the nanoparticles.

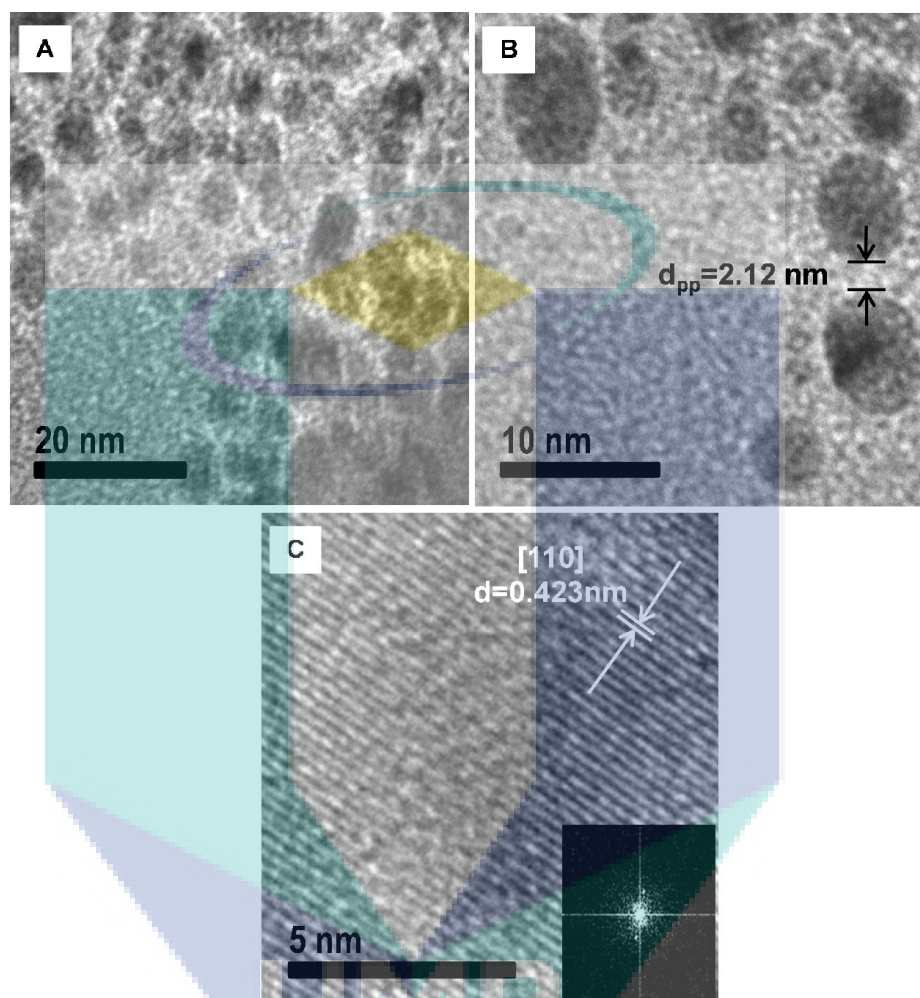


Figure 4.4 (A) and (B) TEM image of α -FeOOH nanoparticles; (C) HRTEM image and the FFT image (as inset)

Further insight into these nanoparticles in higher magnification (Figure 4.4B) shows that the α -FeOOH were partially arrayed, which might be due to average monodispersity of the α -FeOOH nanoparticles (Cheng *et. al.*, 2003a). However, the α -FeOOH nanoparticles in these arrays were still discrete and not fused into larger particles, showing that these nanoparticles have rather high stability upon electrolysis. In addition, the average particle-to-particle distance (d_{pp}) measured was ~ 2 nm (Figure 4.4B), shorter than twice the cationic surfactant molecule length,

which is 3.6 nm (Proverbio *et. al.*, 2006). This may be due to the interdigitation of alkyl chains between the two adjacent iron clusters resulting in discrete nanoparticles.

High-resolution transmission electron microscopy (HRTEM) was adopted to further identify the crystallinity of the catalyst. The HRTEM image (Figure 4.4C) demonstrates high crystallinity of α -FeOOH with an ordered crystal lattice, which can be indexed as (110) plane, whereas the value of the observed interplanar distance (d -spacing) agrees with the d -spacing value obtained from XRD analysis. The inset image in Figure 4.4C demonstrates the fast Fourier transform (FFT) for the lattice image; the bright diffraction spot confirms a single crystal of α -FeOOH.

Morphological properties of MSN and α -FeOOH /MSN were examined by TEM as presented in Figure 4.5. Figure 4.5A shows a well-defined mesostructured nanoparticles and ordered pores of MSN. Introduction of α -FeOOH onto MSN did not alter the original morphology and α -FeOOH was observed to be well deposited on the MSN surface (Figure 4.5B). Insight at higher magnification (Figure 4.5C) showed that the deposited α -FeOOH did not fuse into larger particles and retained its original particle size (5–10 nm), signifying a high stability even after introduction onto the MSN support.

The average particle-to-particle distance (d_{pp}) measured was 2 ± 0.5 nm, shorter than twice the length of the cationic surfactant molecule, which is 3.6 nm. This may suggest a retained colloidal structure of the cationic surfactant around the α -FeOOH on the MSN support (Cheng *et. al.*, 2003a). The value of the interplanar distance (d -spacing) of the lattice fringes estimated from the magnification of a selected area was 0.403 nm and it was consistent with the value of lattice spacing of α -FeOOH obtained from the XRD analysis at (110) facet (Figure 4.5D).

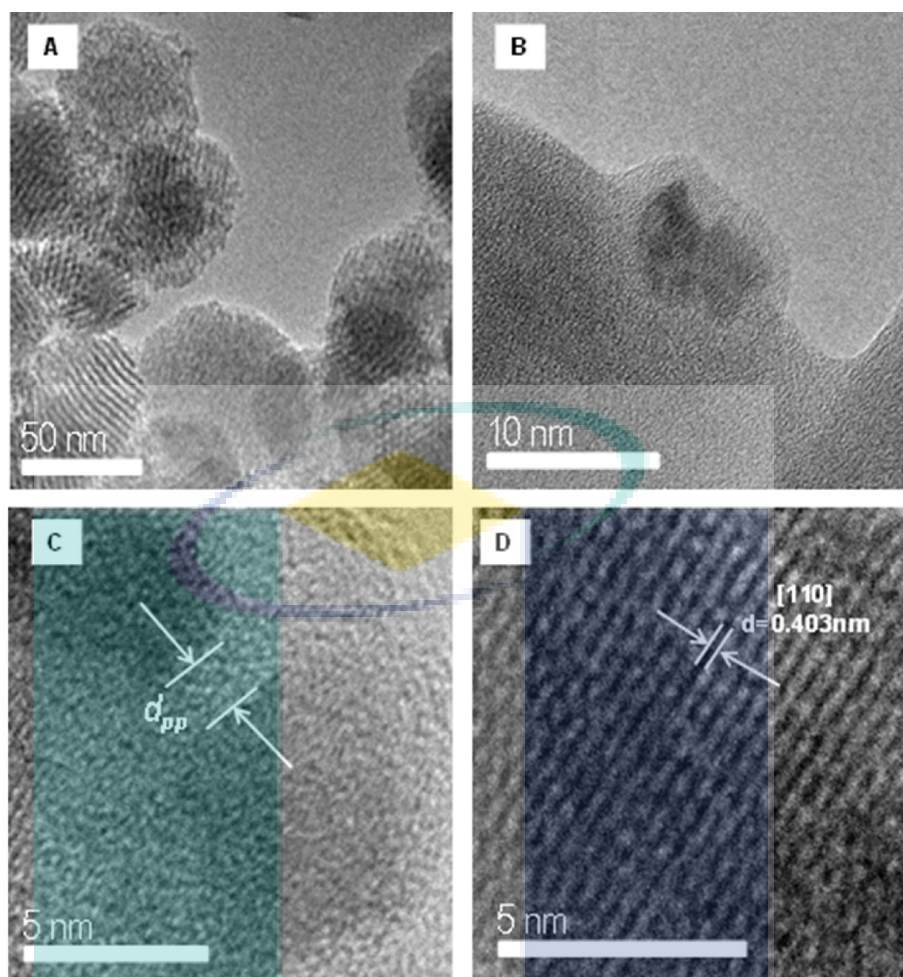


Figure 4.5 TEM image of (A) MSN; (B and C) 10 wt% α -FeOOH /MSN; (D) HRTEM image of 10 wt% α -FeOOH /MSN

UMP

4.2.3 Vibrational Spectroscopy

In order to verify the bonding between the cationic surfactant and α -FeOOH surface, the α -FeOOH was further characterized by means of FT-IR spectroscopy. The spectrum was compared with pure cationic surfactant, post-synthesized commercial α -FeOOH in cationic surfactant (P-FeOOH), and commercial α -FeOOH (C-FeOOH) spectra. A peak at around 3421 cm^{-1} in the spectra of cationic

surfactant, α -FeOOH, P-FeOOH, and C-FeOOH, could be attributed to the metal-OH stretching vibrations of the hydroxyl group (Figure 4.6A) (Wang *et. al.*, 2011a). The peak for α -FeOOH was smaller than those of P-FeOOH and C-FeOOH, implying that there were less hydroxyl groups adsorbed on the surface of α -FeOOH compared to the others. Thus, it could be concluded that cationic surfactant, which acts both as a solvent and electrolyte in the electrolysis process, restricted the adsorption of surface hydroxyl groups.

The peak at band 2989 cm^{-1} was attributed to C-H stretching vibrations of the CH_3 terminal group of the methylene chain of cationic surfactant (Cheng *et. al.*, 2003a). This peak shifted to 2996 cm^{-1} in the α -FeOOH, suggesting a higher density of gauche defects in α -FeOOH rather than in cationic surfactant. The CH_2 stretching vibrations at band 2919 and 2857 cm^{-1} shown in the cationic surfactant spectrum were also shifted to higher frequencies (2927 and 2861 cm^{-1}) in the α -FeOOH, signifying the high density of cationic surfactant defects or bond strength caused by the tethering of cationic surfactant on the α -FeOOH surface, named as colloidal metal.

Figure 4.6B shows a broad peak centered at band 1627 cm^{-1} in all of the samples, attributed to the bending vibration of the OH group. Doublet peaks observed at band 1477 and 1461 cm^{-1} in the cationic surfactant spectrum corresponded to the CH_2 scissoring mode of the cationic surfactant methylene chain. These peaks were shifted to higher frequencies (1484 and 1473 cm^{-1}), and increased in intensity for the α -FeOOH, apparently due to the increasing number of gauche conformers in the chains (Nikoobakht and El-Sayed, 2001). They also shifted to higher frequencies in the P-FeOOH spectrum with similar intensity and broadness with the cationic surfactant spectrum, suggesting an electrostatic interaction between the cationic surfactant and α -FeOOH.

A new peak was observed in the colloidal α -FeOOH spectrum at band 1430 cm^{-1} , which may correspond to head group vibrations of the cationic surfactant at the

α -FeOOH surface. Other new peaks were also observed at band 1068 and 910 cm^{-1} for α -FeOOH (Figure 4.6C), which can most probably be assigned to a stretching mode of bound C-N^+ from cationic surfactant to the α -FeOOH surface (Nikoobakht and El-Sayed, 2001). Two peaks were clearly observed at 960 and 902 cm^{-1} for all of the samples, particularly sharply emerged in colloidal α -FeOOH spectrum, indicating the C-N^+ stretching band.

A clear peak detected at band 790 cm^{-1} in P-FeOOH and C-FeOOH spectra may be attributed to a vibration of $\text{Fe}^{3+}\text{-OH}$ (Bishop and Murad, 2004). According to the literature, this peak illustrates the formation of the OH- layer around the metal core (Vollmer and Janiak, 2011). The relatively smaller appearance of this peak in the α -FeOOH spectrum suggests the rigid coordination between the iron core and the headgroup of the cationic surfactant.

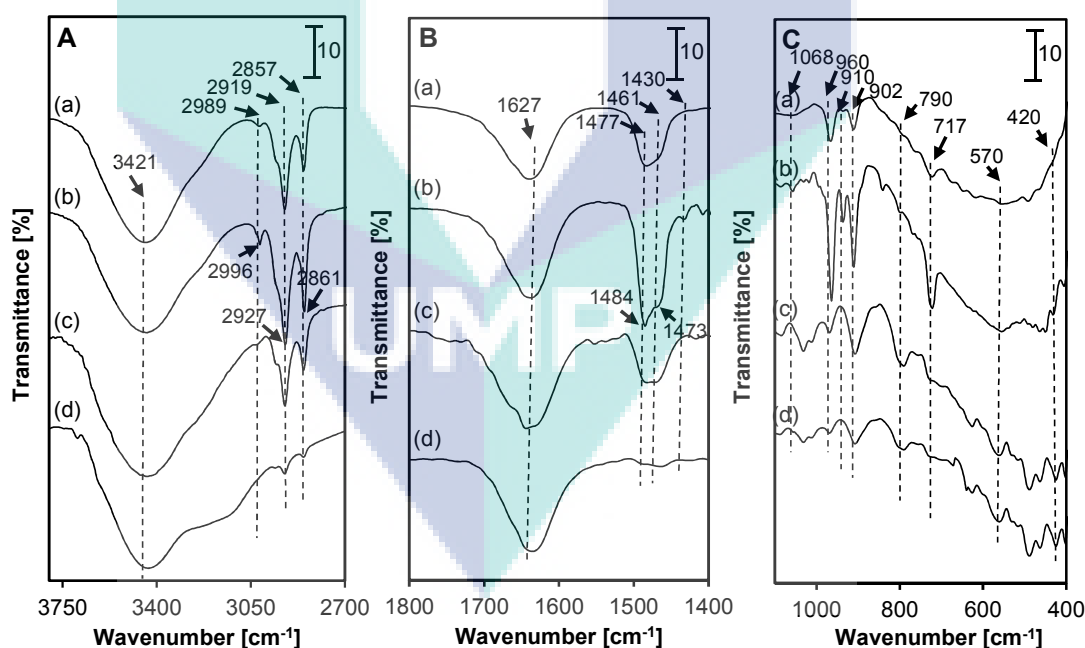


Figure 4.6 FT-IR spectra of (a) ionic surfactant, (b) α -FeOOH, (c) P-FeOOH, and (d) C-FeOOH. (A) Region 3800–2700 cm^{-1} ; (B) region 1800–1400 cm^{-1} ; (C) region 1100–400 cm^{-1}

A peak at band 717 cm^{-1} in the $\alpha\text{-FeOOH}$ spectrum may be assigned to a free rotation of the cationic surfactant methylene chain, implying the methylene chain of the ionic surfactant is pointing outward from the catalyst (Nikoobakht and El-Sayed, 2001). Two peaks obviously observed at band 570 and 420 cm^{-1} in P-FeOOH and C-FeOOH corresponded to Fe-O stretching vibration. These peaks were also slighter in the colloidal $\alpha\text{-FeOOH}$ spectrum, which may be due to the stabilization effect by cationic surfactant through the strongly protective ligand that provides electrosteric protection around the iron core (Kaur and Mehta, 2014).

For further investigation of the interfacial properties of cationic surfactant at the $\alpha\text{-FeOOH}$ surface, the $\alpha\text{-FeOOH}$ catalyst was evacuated for 1 h prior to IR measurement to remove the physisorbed water, and was subjected to a range of $303\text{--}323\text{ K}$ evacuation temperatures. It is observed in Figure 4.7A that the intensity of peak at band 3421 cm^{-1} was decreased with increasing temperature, indicating the loss of water from the catalyst surface.

The peaks at band 2996 , 2927 , and 2861 cm^{-1} , which are attributed to the CH_3 terminal group of the methylene chain and the CH_2 stretching vibrations, respectively, show no change in intensity even at 323 K , verifying the robustness of the cationic surfactant tethering on the $\alpha\text{-FeOOH}$ surface.

The peak at 1627 cm^{-1} shown in Figure 4.7B, which is assigned to the OH group bending vibration, remains unchanged with temperature, further validating the presence of OH- layer formation around the metal core. The peaks at bands 1469 , 1430 , and 1068 cm^{-1} , which correspond to the CH_2 scissoring mode of the cationic surfactant methylene chain, head group vibrations of the cationic surfactant, and stretching mode of bound C-N^+ from cationic surfactant to the $\alpha\text{-FeOOH}$ surface, respectively, were also unaffected by the elevating temperature, which confirms the stability of the colloidal $\alpha\text{-FeOOH}$. However, the peak at 960 cm^{-1} slowly decreased with increasing temperature, indicating the gradual removal of the unbound surfactant (Nikoobakht and El-Sayed, 2001).

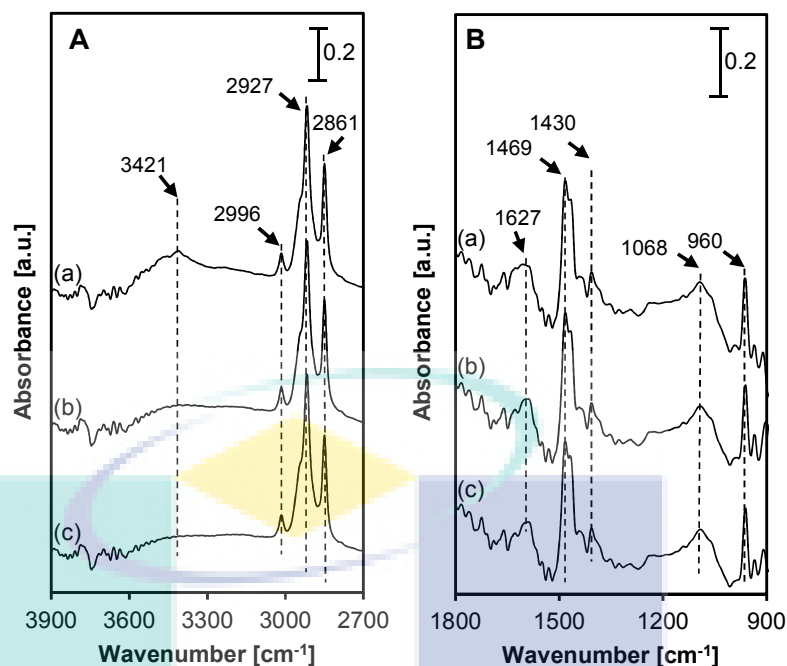


Figure 4.7 FT-IR spectra of α -FeOOH in evacuated system at (a) 303 K, (b) 313 K, and (c) 323 K. (A) Region 3900–2700 cm^{-1} ; (B) region 1800–900 cm^{-1}

All α -FeOOH supported on MSN (α -FeOOH/MSNs) catalysts were characterized by FTIR spectroscopy to verify the bonding between α -FeOOH and MSN (Figure 4.8). A broad band at 3421 cm^{-1} was observed, which could be attributed to the stretching vibrations of the hydroxyl group (Figure 4.8A) (Karim *et al.*, 2012). The CH_2 stretching vibrations of cationic surfactant at band 2927 and 2850 cm^{-1} were observed for all α -FeOOH/MSN samples, indicating the presence of colloidal α -FeOOH in the α -FeOOH/MSNs.

Figure 4.8B shows a broad band at 1621 cm^{-1} in all samples, which attributed to the bending vibration of the OH group for both α -FeOOH and MSN. Doublet peaks observed at band 1480 and 1465 cm^{-1} in the α -FeOOH spectrum correspond to the CH_2 scissoring mode of the cationic surfactant methylene chain (Nikoobakht and El-Sayed, 2001). These bands were significantly observed in α -FeOOH/MSNs, suggesting the presence of colloidal α -FeOOH. The peak at 1430 cm^{-1} , which corresponds to head group vibrations of the cationic surfactant, was observed for all

samples. This implies that the interaction of N^+ with α -FeOOH is retained for all samples.

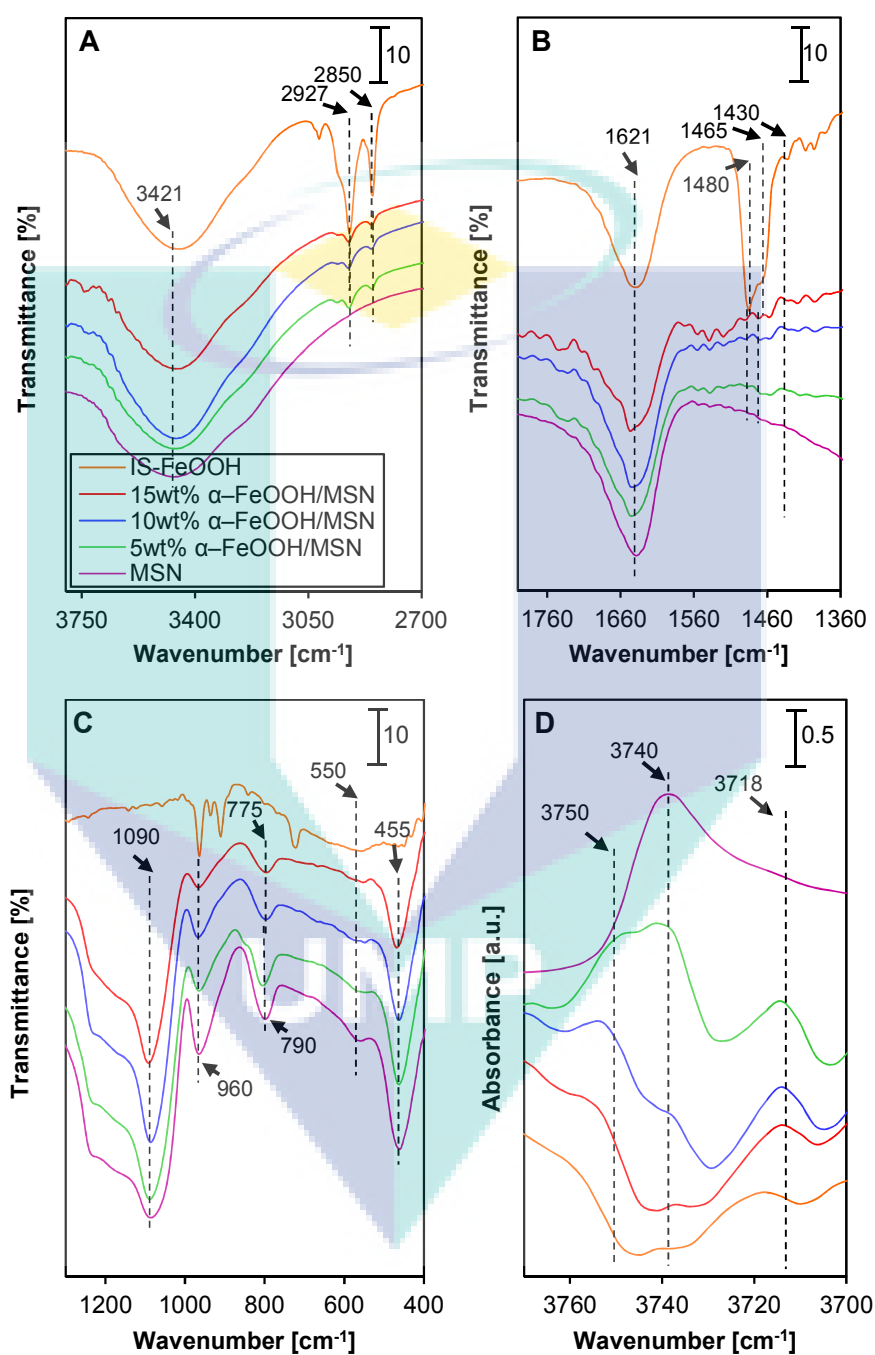


Figure 4.8 FT-IR spectra of catalysts. (A) Region 3800–2700 cm^{-1} ; (B) region 1800–1360 cm^{-1} ; (C) region 1300–400 cm^{-1} ; (D) in evacuated system for region 3770–3700 cm^{-1}

The bands at 1090, 790, and 455 cm^{-1} for MSN and α -FeOOH/MSN catalysts shown in Figure 4.8C are attributed to the characteristics of the silica structure of asymmetric stretching, symmetric stretching, and bending vibration of Si–O–Si bonds, respectively (Endud and Wong, 2007). The introduction of α -FeOOH species onto MSN decreased the intensity of all bands, implying a perturbation of silica network due to removal of silica. Meanwhile, the slight shift of the 790 cm^{-1} band to 775 cm^{-1} may be attributed to the vibration of Fe^{3+} –OH, which illustrates the formation of OH layer around the metal core (Bishop and Murad, 2004). The vibrational mode at around 960 cm^{-1} is attributed to silanol groups present at “defective sites” (Endud and Wong, 2007). The decrease of this band with increasing α -FeOOH loading also signifies its possible interaction with Fe species. Furthermore, the band at 550 cm^{-1} , which corresponds to Si–O bond (Peter *et. al.*, 2012), was also decreased with increasing α -FeOOH loading, indicating significant interaction of silica framework with Fe species from α -FeOOH.

For further investigation of α -FeOOH/MSN structural properties, the catalysts were evacuated for 1 h at 623 K prior to IR measurement to remove the physisorbed water. In Figure 4.8D, a new band at 3750 cm^{-1} appeared in all α -FeOOH/MSN samples which attributed to the geminal silanol groups (Jal *et. al.*, 2004). The band at 3740 cm^{-1} , which is ascribed to the terminal silanol groups (Xue *et. al.*, 2012), decreased with increasing α -FeOOH loading, which confirmed the perturbation of silica framework. Meanwhile, band at 3718 cm^{-1} which is assigned to hydroxyl nests (Karge, 1998), decreased with increasing α -FeOOH loading. Thus, the results suggested that introduction of α -FeOOH onto the MSN caused silica removal in the silica framework. It was also found that the colloidal α -FeOOH still retain its structure after its loading onto MSN. These may due to the strong binding of cationic surfactant molecules to the α -FeOOH nanoparticles which hinder other binding displacement to its surface (Cong *et. al.*, 2010). In a mean time, the colloidal α -FeOOH may adsorbed to the MSN surface which induced the attachment of colloidal α -FeOOH onto the MSN support (Jia and Schüth, 2011).

Meanwhile, in order to investigate the bonding of MSN framework with the Fe species, the overlapped band at 960 cm^{-1} was also further confirmed by a Gaussian curve-fitting (Figure 4.9). Significantly, a new band was observed at 955 cm^{-1} when 5 wt% α -FeOOH was added onto the MSN, which correspond to Si-O-Fe stretching vibrations (Endud and Wong, 2007). The band increased by increasing α -FeOOH loading up to 10 wt%, which confirmed the isomorphous substitution of Fe species after the removal of silica from MSN framework. This Fe species may be originated from the abundant Fe^{3+} ions in electrolysis cell which have not yet transformed to α -FeOOH. However, the increase of α -FeOOH loading up to 15 wt% showed no further increase in the band. This may be due to the saturation of Fe species-MSN interactions. The result also illustrated that the isomorphously substituted Fe species was not from the bulky colloidal structure of α -FeOOH.

Then, the α -FeOOH/MSN_{APTES} catalysts were also characterized by FTIR spectroscopy and compared with the α -FeOOH/MSN to verify bonding between α -FeOOH and different MSNs (Figure 4.10). Two bands were observed at 2915 and 2842 cm^{-1} (Figure 4.10A), attributed to the CH_2 stretching vibrations of IS, signifying the existence of cationic surfactant methylene chains in both the α -FeOOH/MSN and α -FeOOH/MSN_{APTES} catalysts (Cheng *et. al.*, 2003a). However, the intensity of both bands was lower in the latter than in the former catalyst, demonstrating that the stretching vibration in α -FeOOH/MSN_{APTES} is weaker as compared to α -FeOOH/MSN.

The band at 1430 cm^{-1} shown in Figure 4.10B for both α -FeOOH-supported catalysts might correspond to the vibrations of N^+ from the IS head group of α -FeOOH. The bands observed at 1390 and 1338 cm^{-1} were ascribed to the CH_2 wagging mode of the cationic surfactant methylene chain (Chia and Mendelsohn, 1996, Chang and Tanaka, 2002). The presence of these bands suggests that the colloidal form of α -FeOOH was retained and well-dispersed on the MSNs.

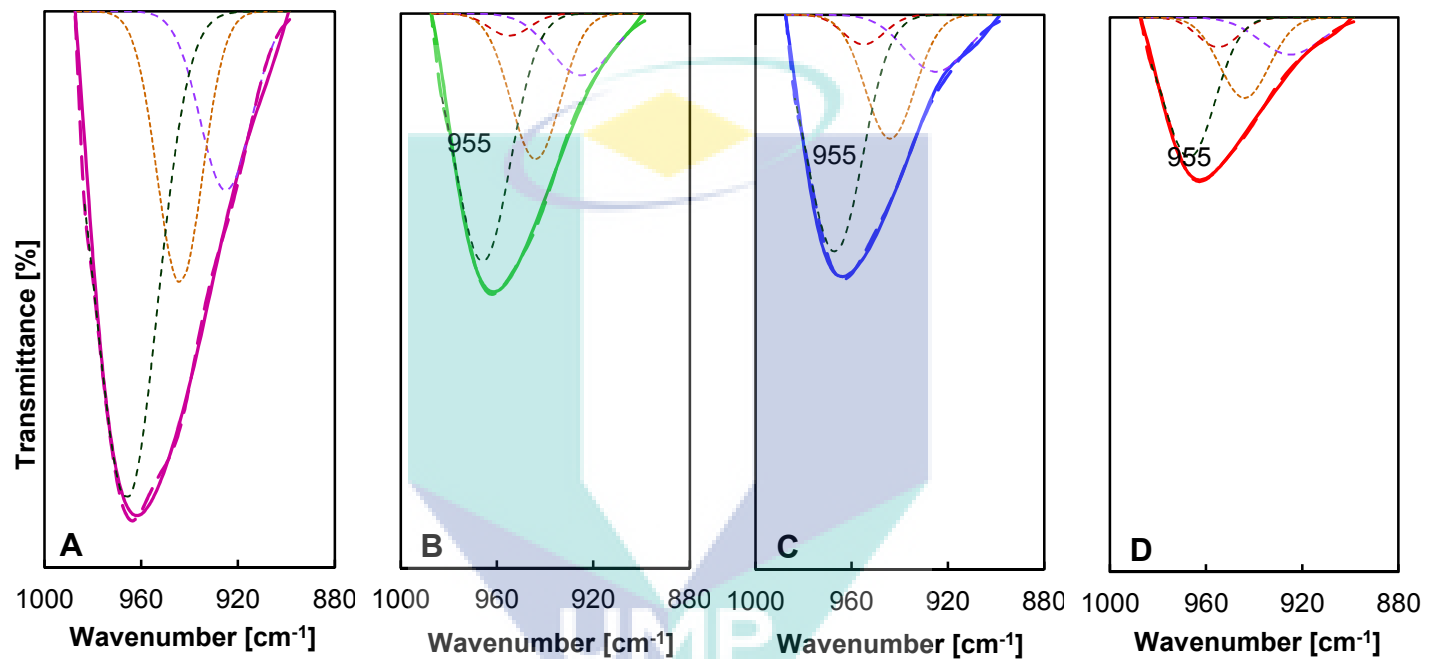


Figure 4.9 FT-IR spectra of (A) MSN, (B) 5wt% α -FeOOH /MSN, (C) 10wt% α -FeOOH /MSN and (D) 15wt% α -FeOOH /MSN and Gaussian curve-fitting of band at 960 cm^{-1}

Meanwhile, the bands at 1090 cm^{-1} for all catalysts shown in Figure 4.10C were attributed to the characteristics of the silica structure, i.e. asymmetric stretching of Si–O–Si bonds (Endud and Wong, 2007). It was observed that the introduction of colloidal α -FeOOH onto MSNs significantly decreased the band intensity, implying the possible removal of silica by an ion exchange process in the presence of the strong ammonium salt in the colloidal mixture (Kerker, 2012).

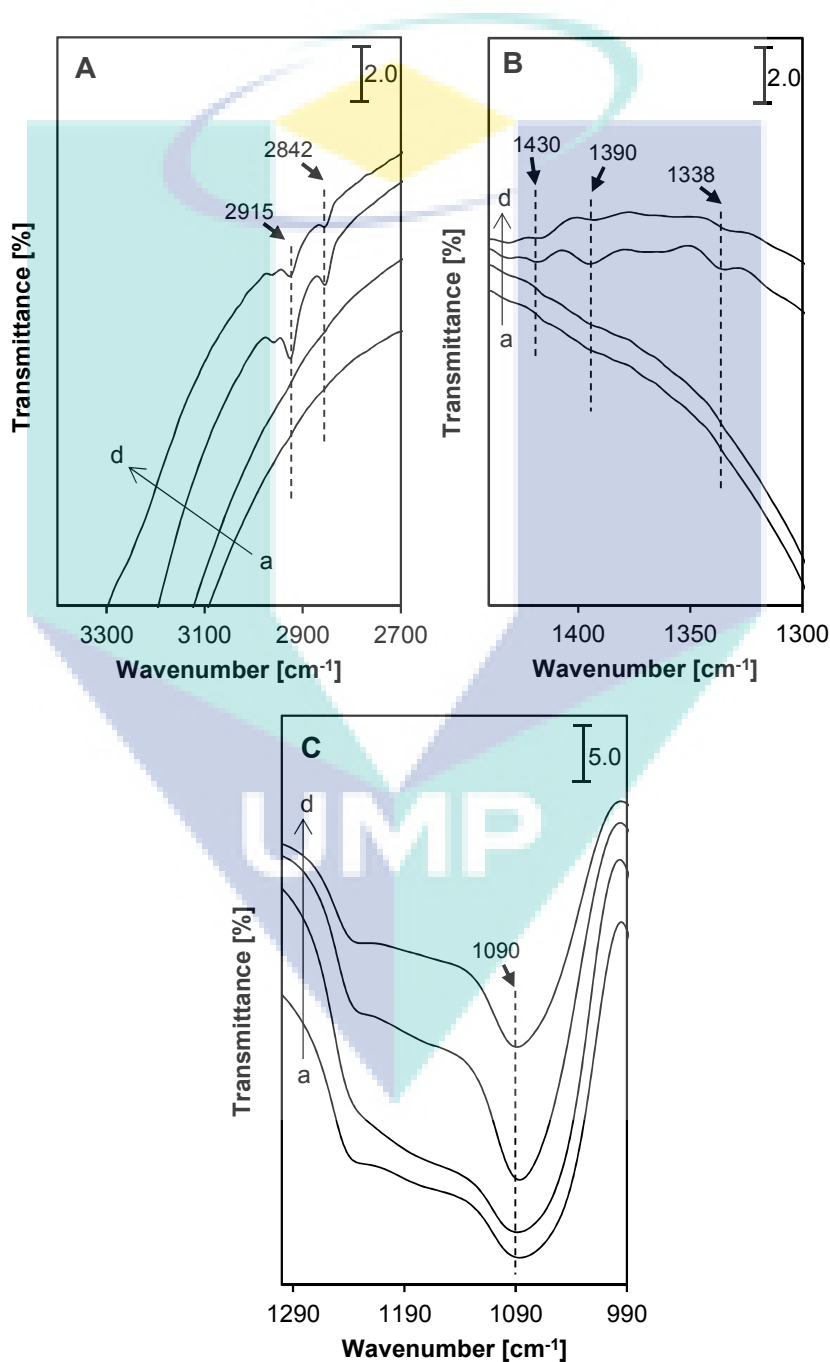


Figure 4.10 FT-IR spectra of catalysts. (a) MSN; (b) $\text{MSN}_{\text{APTES}}$; (c) α -FeOOH/MSN; (d) α -FeOOH/ $\text{MSN}_{\text{APTES}}$

4.2.4 Study of Textural Properties

Nitrogen adsorption–desorption isotherms and the corresponding pore size distribution plots of all catalysts are shown in Figure 4.11. All isotherms showed a type IV profile and type H1 hysteresis loops (IUPAC classification), representing the characteristics of mesoporous materials with highly uniform cylindrical pores (Figure 4.11A). MSNs samples showed two steps of capillary condensation with the first step at $P/P_0 = 0.3$ due to mesopores inside the MSN (intraparticles) and secondly at a higher partial pressure ($P/P_0 = 0.9$), which was attributed to interparticle textural porosity.

It could be observed that the pristine MSN showed bimodal pore size distributions that consisted of a primary pore at ~ 2.7 nm and secondary pore at ~ 3.5 nm (Figure 4.11B). The introduction of APTES into MSN maintained both pore distributions and developed larger pores 5.0–9.5 nm in size. When α -FeOOH was loaded onto pristine MSN, the intrapores decreased significantly while the interpores increased, signifying pore blockage by α -FeOOH for the former and the possible removal of silica from the MSN framework for the latter case. In contrast, the addition of α -FeOOH into $\text{MSN}_{\text{APTES}}$ completely eliminated the pores larger than 3.5 nm.

Based on the decrease in Si–O–Si bond intensity in the FTIR results, this confirmed that the additional removal of silica occurred in $\text{MSN}_{\text{APTES}}$, thus this most probably allowed the colloidal α -FeOOH with an original particles size of 5–10 nm to be located in the pore channel. However, due to the smaller pore size in pristine MSN, α -FeOOH existed only on the surface. The surface area (S_{BET}) of the samples supported this result, in the following order: $\text{MSN}_{\text{APTES}} > \text{MSN} > \alpha$ -FeOOH /MSN $> \alpha$ -FeOOH / $\text{MSN}_{\text{APTES}}$ with values of 1136, 1107, 734, and 529 $\text{m}^2 \text{g}^{-1}$, respectively.

This result is also in agreement with the XRD data, confirming the reduction of MSN crystallinity upon loading of α -FeOOH. In addition, this result may also explain the weaker CH₂ stretching vibrations in α -FeOOH/MSN_{APTES} than in α -FeOOH/MSN. Remarkably, the results show that pore size modification of the support could control the location of the introduced colloidal α -FeOOH. Similar variations in catalyst localization have been reported by Lee *et al.* (2008) using different sizes of loaded Pt particles on an SBA-15 support.

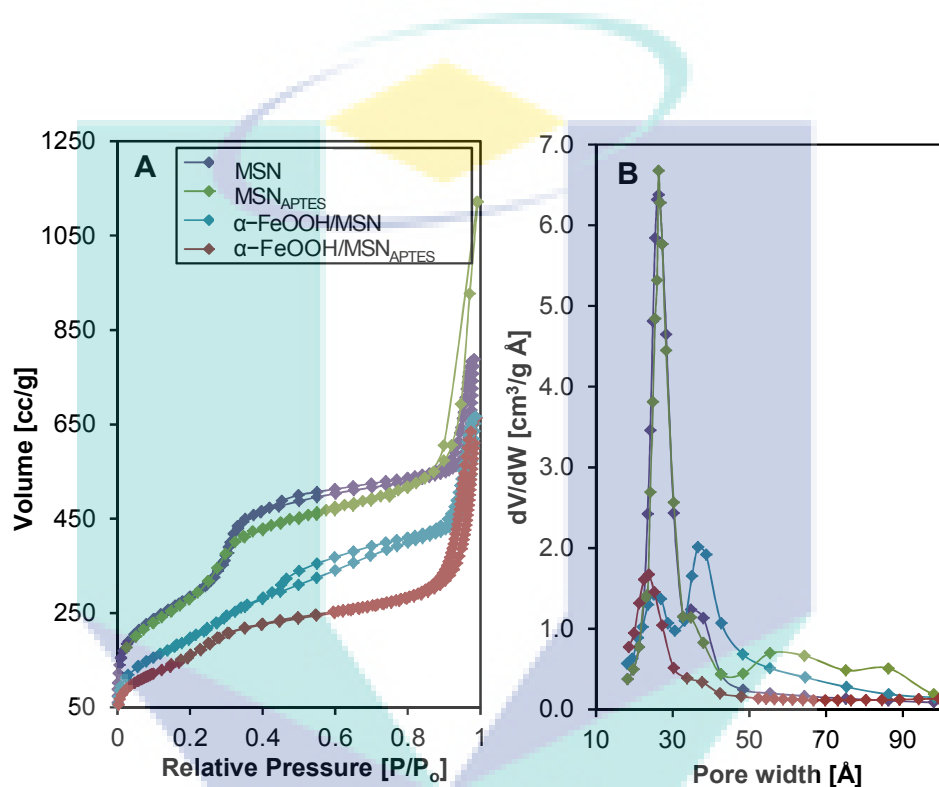


Figure 4.11 (A) N₂ adsorption-desorption isotherm; (B) pore size distributions of the catalysts

Porosity of the catalyst was then studied by the pore size distributions depicted in Figure 4.12 for different α -FeOOH loading on the MSN. MSN showed bimodal pore size distributions that consisted of a primary pore at 2.7 ± 0.9 nm and secondary pore at 3.5 ± 0.7 nm. Introduction of α -FeOOH onto MSN has successfully retained its bimodal structures, with decreasing in the intrapore and increase in the interpore distribution. However, loading of larger amount of α -

FeOOH onto MSN induced pore blockage, which subsequently reduced the pore volume of 10 and 15% α -FeOOH/MSN compared with 5% α -FeOOH/MSN.

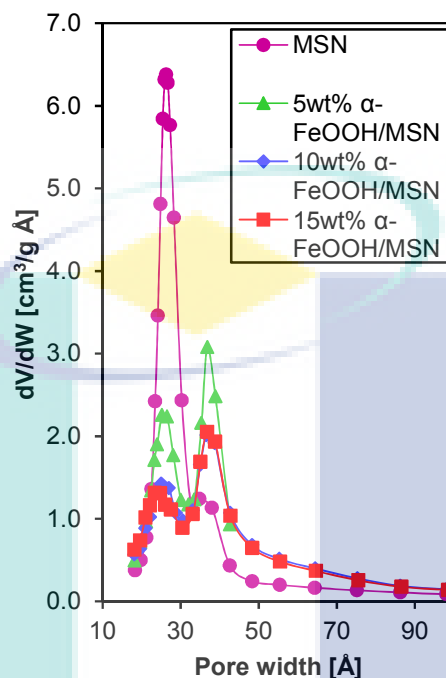


Figure 4.12 Pore distribution of MSN, 5 wt% α -FeOOH/MSN, 10 wt% α -FeOOH/MSN, and 15 wt% α -FeOOH/MSN catalysts

As shown in Table 4.1, surface area (S_{BET}) of α -FeOOH/MSN decreased from 1107 to 665 $\text{m}^2 \text{g}^{-1}$, following the order MSN > 5 wt% α -FeOOH/MSN > 10 wt% α -FeOOH/MSN > 15 wt% α -FeOOH/MSN. This suggested that a portion of the α -FeOOH was dispersed on the surface of MSN.

Average pore size of MSN was found to be increased upon the introduction of α -FeOOH, that might be due to the increase in interparticle pores, as shown in Figure 4.12. Indeed, formation of a bimodal pore structure may be related to the removal of silica from MSN framework (Groen *et. al.*, 2004a). Increasing the amount of α -FeOOH loaded may induce the silica removal rate, which then led to the reduction in pore size and increase in pore volume of the MSN (Dai *et. al.*, 2013).

Table 4.1 Textural properties of catalysts.

Sample	Surface area, S_{BET} ($\text{m}^2 \text{g}^{-1}$)	Average pore size, D_{pore} (nm)	Average pore volume, V_{pore} ($\text{cm}^3 \text{g}^{-1}$)
MSN	1107	3.00±1.20	2.14
5wt% α -FeOOH/MSN	850	3.10±1.14	0.61
10wt% α -FeOOH/MSN	734	3.09±1.27	1.04
15wt% α -FeOOH/MSN	665	3.01±1.19	0.99

4.2.5 Chemical Environment Determination

The MSN and 10 wt% α -FeOOH/MSN which was found to be the best catalyst was subjected to ^{29}Si MAS NMR to compare and elucidate their detailed structure (Figure 4.13). The dominant signal shown by MSN at approximately -112.485 ppm was assigned to $(\equiv\text{SiO})_4\text{Si}$. This peak reduced and shifted to -105.110 by the loading of α -FeOOH, indicating the alteration at $(\equiv\text{SiO})_4\text{Si}$ sites.

New shoulders were developed in the range of -90 to -100 ppm, which signified that the $(\equiv\text{SiO})_3\text{Si}$ sites were formed in consequence of silica removal in MSN framework (Setiabudi *et. al.*, 2012). This result is consistent with XRD and FTIR, which support the decreased of Si–O–Si bonds. In fact, the silica removal that occurred may be due to the presence of ammonium salt in the synthesis process (Groen *et. al.*, 2007b). The interaction between ammonium ions and silica followed by subsequent attack of the hydroxide ions on the external surface of MSN may dissociate some Si–O–Si bonds from the framework.

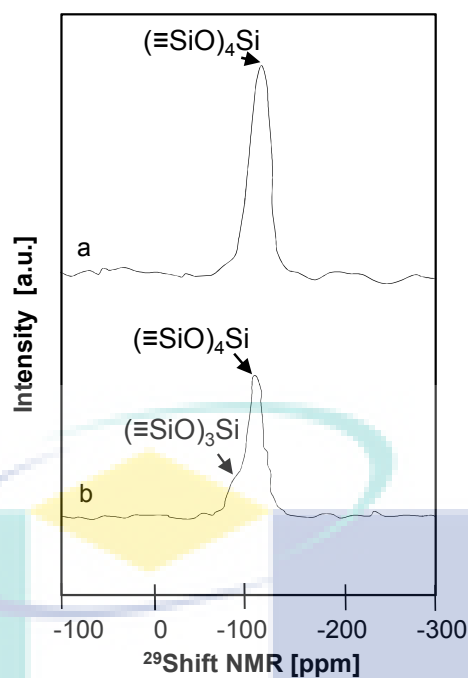


Figure 4.13 ^{29}Si MAS NMR spectra of (a) MSN and (b) 10wt% α -FeOOH/MSN

4.2.6 Chemical Oxidation State Determination

The ESR spectroscopy is a very sensitive technique for studying the nature and the crystal symmetry environment of iron in mesoporous silica. Thus, the α -FeOOH and α -FeOOH/MSN catalysts were subjected to ESR and the spectra are presented in Figure 4.14. The presence of a signal at $g = 4.3$ for all α -FeOOH/MSN samples indicate the presence of Fe^{3+} in the MSN framework (Li *et al.*, 2012c). This observation is in agreement with the FTIR results, which suggest free Fe species might take part in the isomorphous substitution step, which indicates that two types of iron are present in the α -FeOOH/MSN catalyst structure.

The normalization of peak at $g = 4.3$ (inset figure) indicates that all α -FeOOH/MSN samples have different bandwidth which suggest different

arrangement of Fe^{3+} in the MSN framework (Bourlinos *et. al.*, 2010). This is also in agreement with the FTIR result which suggests gradual silica removal step accompanied with isomorphous substitution of Fe cations at different $\alpha\text{-FeOOH}$ loading onto MSN. The $g = 1.8$ was also observed for all samples which attributes to the presence of organometallic, signifying the $\alpha\text{-FeOOH}$ is retained in the MSN framework (Rieger, 2008). Both signals show pronounced shifts after $\alpha\text{-FeOOH}$ were loaded onto MSN, which confirm the bonding of Fe species and colloidal $\alpha\text{-FeOOH}$ with the MSN support.

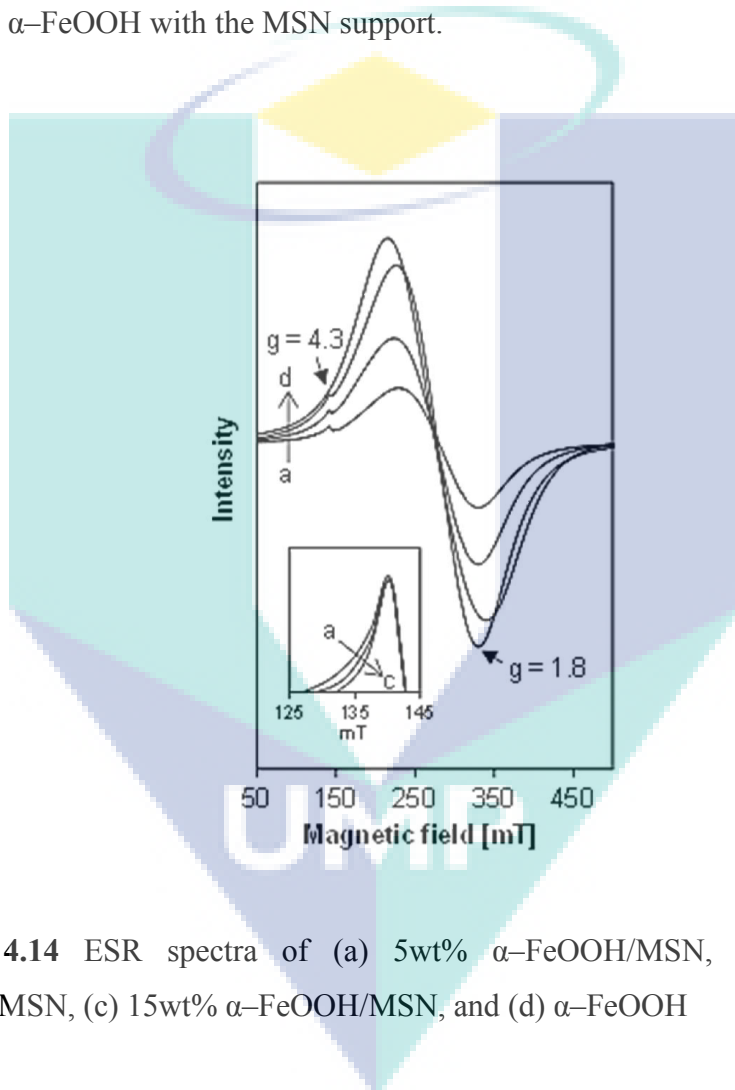


Figure 4.14 ESR spectra of (a) 5wt% $\alpha\text{-FeOOH/MSN}$, (b) 10wt% $\alpha\text{-FeOOH/MSN}$, (c) 15wt% $\alpha\text{-FeOOH/MSN}$, and (d) $\alpha\text{-FeOOH}$

The 10 wt% α -FeOOH/MSN catalyst was then subjected to XPS analysis in order to elucidate its exact structure. The Fe_{2p} doublet with binding energies of 708 and 722 eV shown in Figure 4.15A implied the presence of Fe–O bond of the α -FeOOH species (Palma *et. al.*, 2007).

Meanwhile, the three peaks at 527, 530, and 533 eV displayed by the O_{1s} (Figure 4.15B) correspond to the presence of Si–O–Si, Si–O–Fe and Si–O–H bonds, respectively, since the binding energy of electrons at the oxygen atom increases as the electron–electron repulsion decreases due to the electronegativity sequence of its adjacent atom: hydrogen > iron > silica (Simonsen *et. al.*, 2009). Therefore, it was confirmed that Si–O–Fe groups were present in the α -FeOOH/MSN catalyst and this was in agreement with FTIR results.

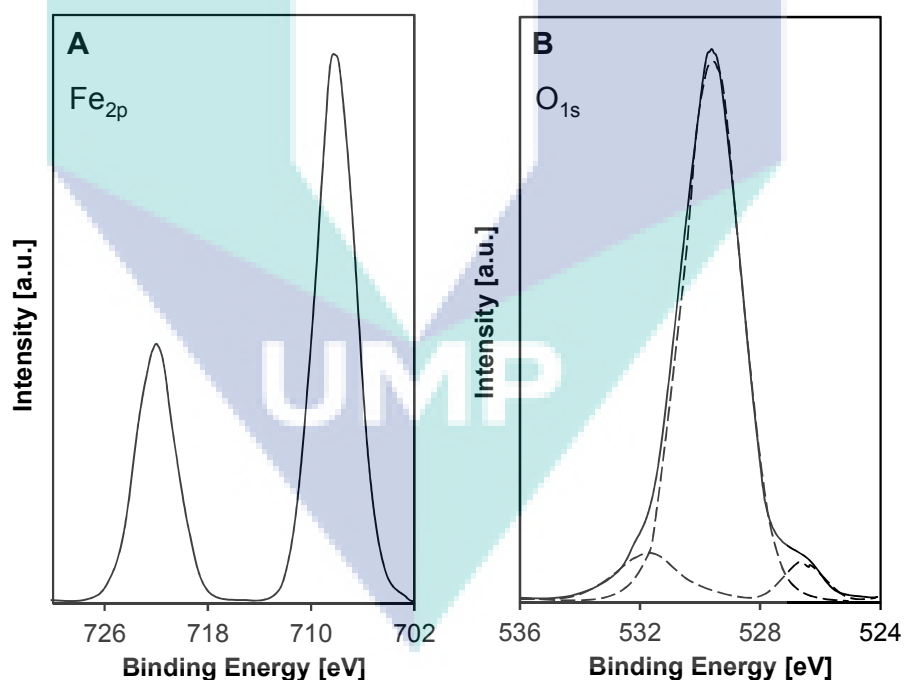


Figure 4.15 XPS spectra of (B) Fe_{2p} and (C) Si_{2p} for 10 wt% α -FeOOH/MSN catalyst

4.2.7 Proposed Structure of Photocatalysts

According to the previous studies, the reaction pathway for the formation of colloidal α -FeOOH was proposed as follows (Figure 4.16). Electrolysis of cationic surfactant solution with a platinum cathode and an iron anode resulted in anodic dissolution of Fe metal to give Fe^{2+} ions (Eq. 4.1). At the cathode, two-electron reduction of water molecules occurs to produce hydroxyl ions OH^- (Eq. 4.2) (Gupta, 2003b), which then reacts with Fe^{2+} ion in the system to give iron hydroxide $Fe(OH)_2$ (Eq. 4.3). Oxidation of this species produces $Fe(OH)_3$ and subsequent dehydrolysis gives the α -FeOOH (Eq.4.4–4.5) (Hu *et. al.*, 2011a, Krehula *et. al.*, 2002).



Based on the characterization results, it could be proposed that the α -FeOOH was formed in a reverse micelle structure bound on the α -FeOOH surface (Figure 4.16). FTIR analysis confirmed that the headgroups of cationic surfactant were attached to hydroxyl anion groups around the iron core with a free swinging alkane tail point outward from the catalyst.

The interdigitation of alkane chains between two adjacent α -FeOOH units, which was verified by TEM analysis, led to the discrete and high curvature of the nanoparticles surface. Thus, the colloidal α -FeOOH catalyst is very stable and robust, as proved by the evacuated FTIR at elevated temperature.

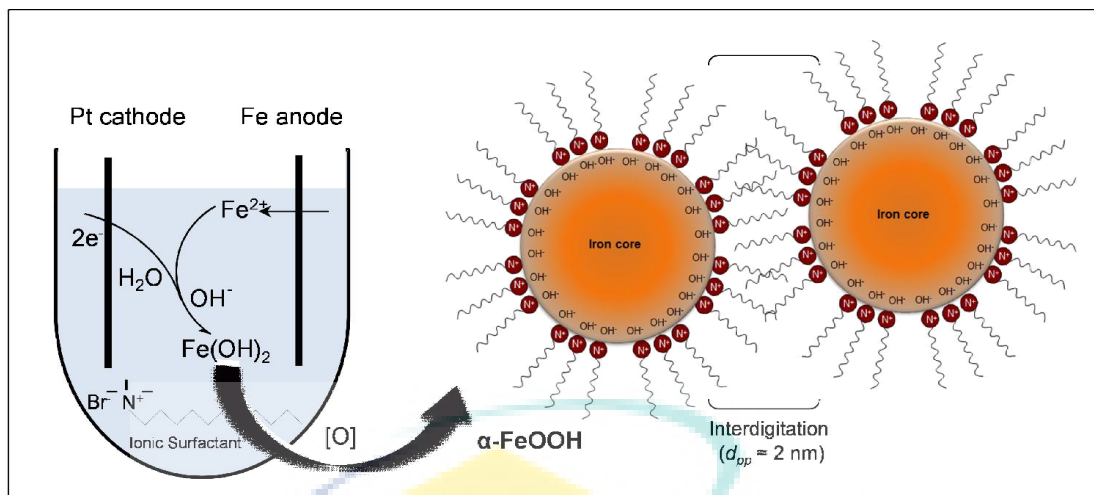


Figure 4.16 The proposed reaction pathways for electrosynthesis of α -FeOOH

Based on the characterization results for the α -FeOOH supported MSN catalysts, a probable α -FeOOH/MSN structure is proposed as shown in Figure 4.17. The presence of cationic surfactant ammonium groups in α -FeOOH/MSN system during the preparation step caused removal of silica, which then induced the isomorphous substitution of free Fe^{3+} species in the system, as proven by the presence of Si-O-Fe bond in FTIR and XPS data. The XRD, surface area analyses, and NMR also supported the silica removal process.

The colloidal form of α -FeOOH was also found to be retained and dispersed well on the MSN support as verified by the TEM and FTIR results. The decrease in intraparticle pores and simultaneous increase in interparticle pores with increasing α -FeOOH/MSN loading, as shown by the pore size distribution result, as well as the ESR results, also clarified the isomorphous substitution of Fe^{3+} species and the retainment of colloidal α -FeOOH structure on the MSN. Remarkably, the results show that two types of Fe species could be formed when using MSN as a support in the cationic surfactant system.

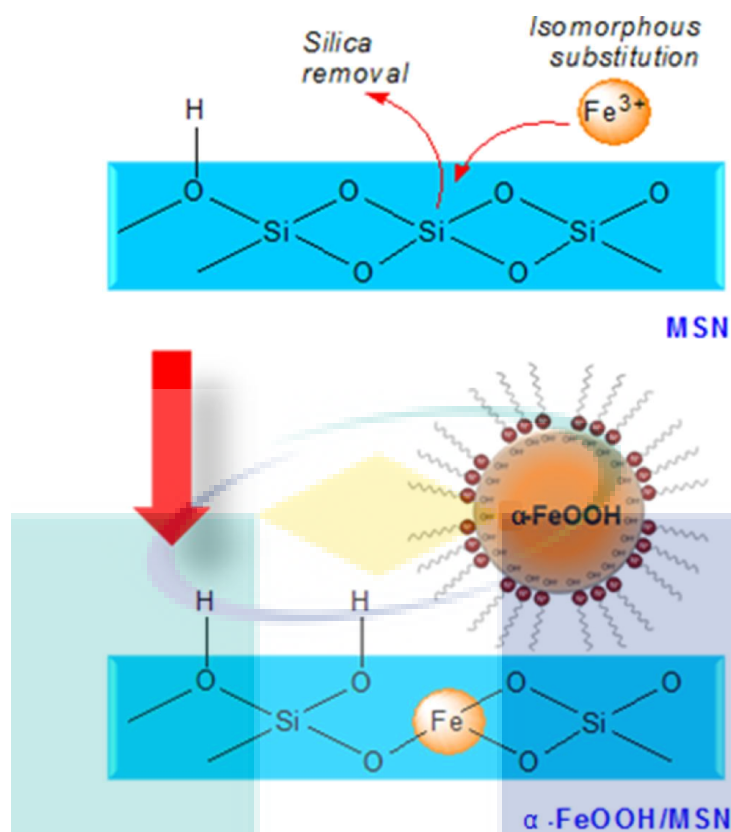


Figure 4.17 Proposed structure of α -FeOOH/MSN

4.3 Photodegradation Performance Evaluations

The photocatalytic activity of the prepared catalysts was tested for the photo-Fenton-like degradation of 2-CP under several conditions. Control experiments under dark conditions were conducted to investigate the importance of visible light irradiation for this system under pH 5, H_2O_2 concentration 0.156 mM; catalyst dosage 0.30 g L^{-1} ; initial concentration 50 mg L^{-1} ; temperature 303K. The result shows that less than 5% of 2-CP degradation was achieved after 8 h of contact time for α -FeOOH while, less than 15% when using α -FeOOH/MSN, which indicates the importance of visible light irradiation in this study. The performances of the catalysts were studied under effect of pH, metal loading, catalyst dosage, initial dye concentration, and temperature. The related characterization such as UV-DRS and PL analysis were conducted. The stability

of catalysts was investigated and the catalytic photodegradation mechanisms were also proposed.

4.3.1 Performance of the Photocatalysts

The performance of the α -FeOOH was examined on the degradation of 2-CP photo-Fenton-like reaction and compared with the C-FeOOH and P-FeOOH (Figure 4.18). It is well-known that α -FeOOH is a practically inactive photocatalyst for the degradation of such organic contaminants in the absence of any oxidizing agent (e.g., H_2O_2) that plays an important role in providing hydroxyl radicals ($\cdot\text{OH}$) for the reaction. However, as can be seen in Figure 4.18, the synthesized α -FeOOH was able to give 56% of 2-CP degradation under visible light irradiation even in the absence of H_2O_2 . This capability is significantly higher than those reported in the literature, which can only degraded less than 10% of 2-CP in the similar reaction system (Bandara *et. al.*, 2001a).

In fact, the production of $\cdot\text{OH}$ can be enhanced drastically by combining the photocatalytic system (UV/metal oxide) with the Fenton-like system (metal oxide/ H_2O_2), a so-called photo-Fenton-like system. As shown in Figure 4.18, the 2-CP was successfully degraded up to 85% when using this system. It is presumed that the headgroups of reverse micelle cationic surfactant that bound at the α -FeOOH surface have trapped the photogenerated electrons at the conduction band (CB) and simultaneously decreased the recombination rate of photo-induced electron-hole pairs at the valence band (VB), which resulted in the enhancement of the 2-CP degradation.

However, the absence of reverse micelle structure in P-FeOOH and C-FeOOH catalysts only produced 73% and 63% of the degradation, respectively.

The electrostatic interaction between the cationic surfactant and α -FeOOH of P-FeOOH, which was confirmed by FTIR analysis, could explain the relatively higher degradation percentage of P-FeOOH compared to C-FeOOH.

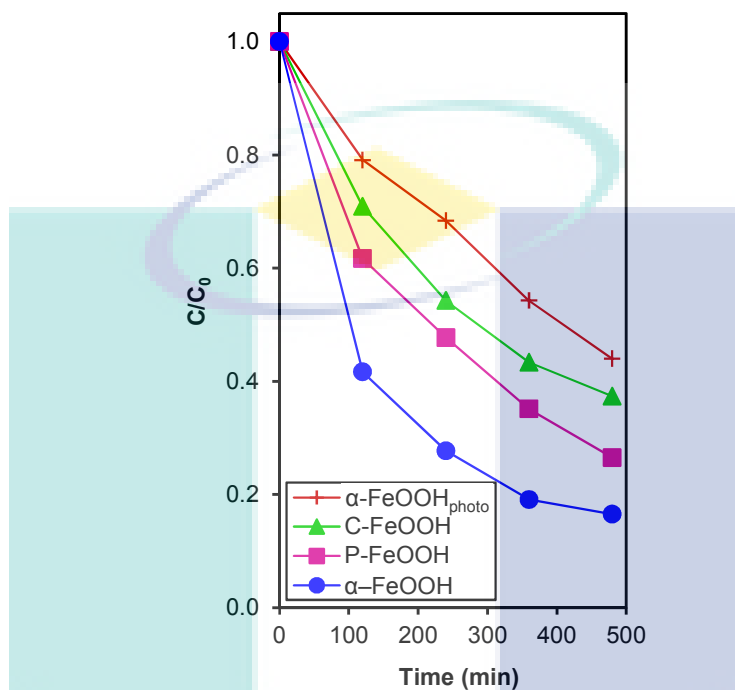


Figure 4.18 The performance of catalysts under light irradiation for photocatalysis of α -FeOOH, photo-Fenton-like reaction of C-FeOOH, P-FeOOH, and α -FeOOH catalysts [pH 5; H₂O₂ concentration 0.156 mM; catalyst dosage 0.30 g L⁻¹; initial concentration 50 mg L⁻¹; temperature 303K].

In order to examine the role of cationic surfactant in the photo-Fenton-like reaction, an excess cationic surfactant was added to the 2-CP solution containing C-FeOOH, and this system was denoted as CS+FeOOH. As shown in Figure 4.19, the CS+FeOOH showed similar catalytic performance with pure C-FeOOH, in which 65% of maximum degradation percentage of 2-CP has been achieved after 480 min of reaction. From this result, it could be stated that the excess cationic surfactant in solution has no significant effect on the photo-Fenton-like activity of α -FeOOH. This result supports that the photo-Fenton-like activity enhancement was due to the electrosynthesized α -FeOOH but not due to

the simple electrostatic attraction between $[N]^+$ of cationic surfactant and negatively charged chlorine $[Cl]^-$ from the 2-CP.

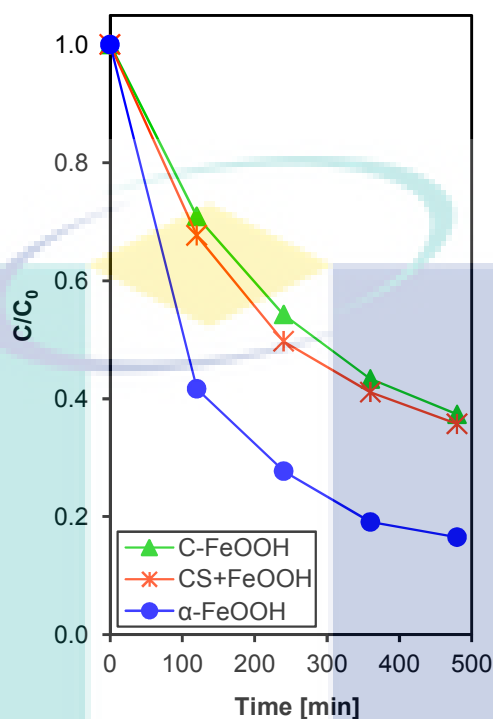


Figure 4.19 Effects of cationic surfactant on the photo-Fenton-like activity [pH 5; H_2O_2 concentration 0.156 mM ; catalyst dosage 0.30 g L^{-1} ; initial concentration 50 mg L^{-1} ; temperature 303K].

The performance of $\alpha\text{-FeOOH}$ supported both pristine MSN and modified MSN was also examined for the photodegradation of 2-CP under visible light conditions (Figure 4.20). Only 17.5% and 38.7% of the 2-CP was degraded when using the pristine MSN and MSN_{APTES} , respectively. However, the degradation percentage was increased up to 92.2% when using $\alpha\text{-FeOOH/MSN}$.

The distribution of $\alpha\text{-FeOOH}$ nanoparticles on the surface of MSN might have facilitated their surface contact with light, which led to higher efficiency of degradation. A lower degree of degradation of 2-CP was shown by $\alpha\text{-}$

FeOOH/MSN_{APTES} (77.6%), possibly due to the location of colloidal α -FeOOH in the pores of MSN_{APTES} which hindered visible light accessibility of α -FeOOH.

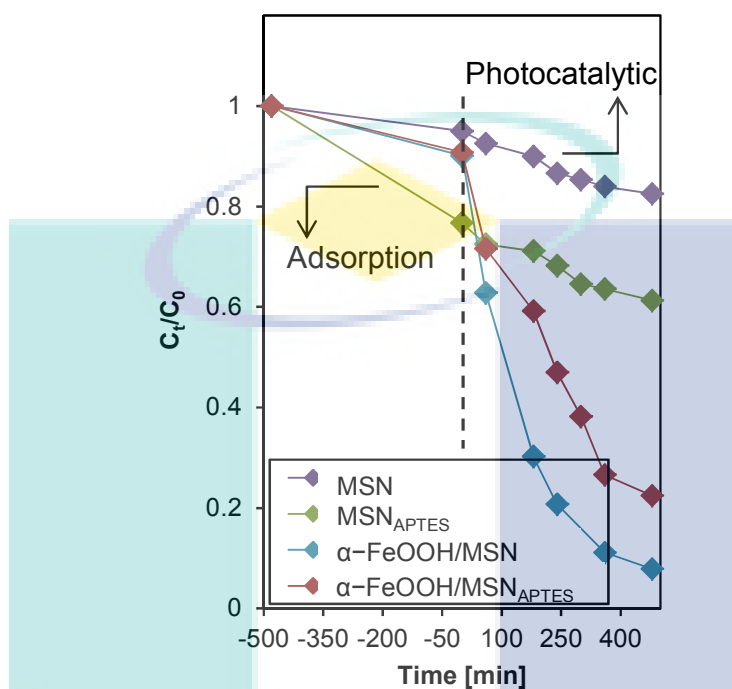


Figure 4.20 The 2-CP photodegradation performance of the catalysts [pH 5; H₂O₂ concentration 0.156 mM; catalyst dosage 0.30 g L⁻¹; initial concentration 50 mg L⁻¹; temperature 303K].

UMP

4.3.2 Effect of Metal Loading

The performance of α -FeOOH/MSN at different α -FeOOH loading was then examined for photodegradation of 2-CP. The results are shown in Figure 4.21. Only 14.2% of the 2-CP was removed when using the bare MSN, most probably due to the generated \cdot OH via direct photoconversion of the added H₂O₂.

However, the removal percentage increased up to 73.1% and 92.2% by using the 5 wt% α -FeOOH/MSN and 10 wt% α -FeOOH/MSN, respectively. Proper distribution of α -FeOOH nanoparticles on the surface of MSN might facilitate their surface contact with light, which led to higher efficiency of degradation (Sapawe *et. al.*, 2012). In contrast, further increase in α -FeOOH/MSN loading give no significant effect on the degradation.

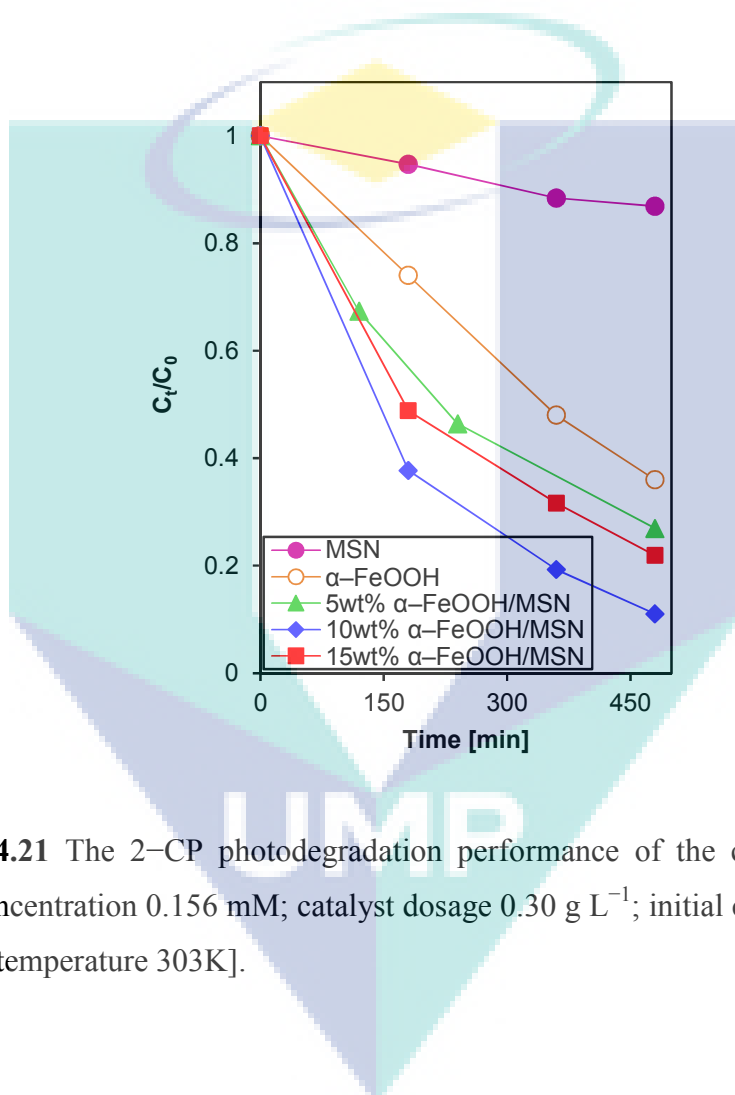


Figure 4.21 The 2-CP photodegradation performance of the catalysts [pH 5; H₂O₂ concentration 0.156 mM; catalyst dosage 0.30 g L⁻¹; initial concentration 50 mg L⁻¹; temperature 303K].

The α -FeOOH/MSN catalysts were also subjected to photoluminescence (PL) analysis at an excitation wavelength of 650 nm in visible region (Figure 4.22). 5 wt% α -FeOOH/MSN showed highest peak intensity, followed by the 15 wt% and 10 wt% α -FeOOH/MSN. Addition of α -FeOOH decreased the content of surface oxygen vacancies and/or defect sites, which affected the intensity and response range of PL signals (Hariharan, 2006). Indeed, the oxygen vacancies and

defect sites are important to trap the electrons to keep the e^-h^+ pairs separate in order to enhance photocatalytic activity.

It has been reported that the lower the peak intensity, the lower the recombination rate of the photoinduced electron–hole pair, which results in higher photocatalytic activity (Jusoh *et. al.*, 2013). This fact may explain why the photocatalytic activity was in the following order: 10 wt% α -FeOOH/MSN > 15 wt% α -FeOOH/MSN > 5 wt% α -FeOOH/MSN. The limitation of increasing α -FeOOH loading to 15 wt% may be because of the accumulation of excess α -FeOOH on the surface of the α -FeOOH/MSN catalysts, which led to the lower rate constant and photoactivity (Li *et. al.*, 2012c).

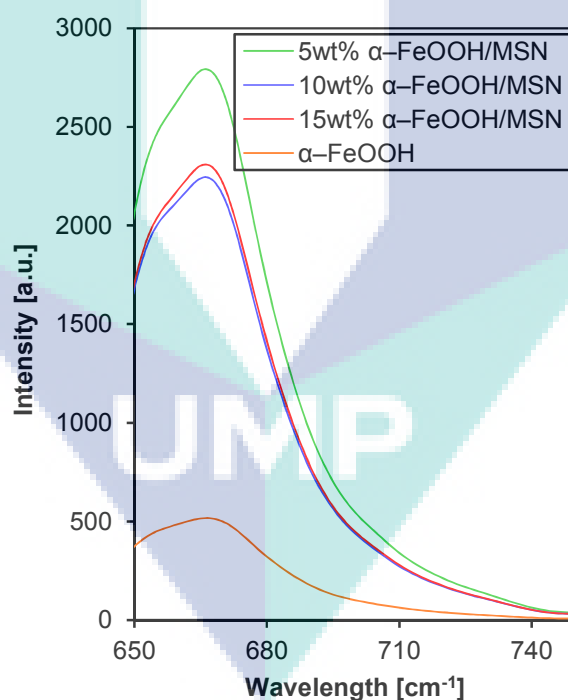


Figure 4.22 Photoluminescence spectra for α -FeOOH/MSN catalysts

This result is in agreement with the band gap determination results shown in Table 4.2. The band gap energy of α -FeOOH and α -FeOOH/MSNs was

determined using Kubelka–Munk (K–M) spectrum. The results show a reduction in band gap energy with increase in α -FeOOH loading up to 15wt%.

It was known that low band gap energy results in efficient performance of photocatalyst. However, the aforementioned possibility of the α -FeOOH accumulation on 15wt% α -FeOOH surface may hinder its effective performance towards the 2-CP degradation, regardless of the low band gap energy value.

Table 4.2 Calculated band gap value for each catalyst.

Catalysts	Band gap ^a (eV)
α -FeOOH	2.75
5wt% α -FeOOH/MSN	3.25
10wt% α -FeOOH/MSN	3.00
15wt% α -FeOOH/MSN	2.90

^a Derived from plotted graph K–M versus $h\nu$

4.3.3 Effect of pH

The influence of initial pH solutions on the degradation of 2-CP over α -FeOOH and α -FeOOH/MSN was studied in the pH range of 3.0 – 7.0 and the result was shown in Figure 4.23 and 4.24. The result revealed a maximum efficiency at pH 5 for both catalysts as α -FeOOH and α -FeOOH exhibits a positive zeta potential at pH values below pH_{pzc} (Wu *et al.*, 2011). This is in agreement with the results reported by Bandara *et al.*, (2007b) in degradation of 4-chlorophenol. At low pH ($pH < 3.0$), H_2O_2 could stay stable probably by solvating a proton which later form an oxonium ion ($H_3O_2^+$) as presented by Eq. 4.6. H_2O_2 enhanced its stability since $H_3O_2^+$ makes it to become electrophilic and

presumably reduce significantly the reactivity with ferrous ion (Hassan and Hameed, 2011), thus reduced the degradation of 2-CP.



In case of $pH > 5.0$, the photodegradation efficiency decreased due to the decreases of dissolved fraction of α -FeOOH species (Kwon *et al.*, 1999). Also, the oxidation potential of the OH radical is known to decrease with increasing pH and the stability of H_2O_2 starts to decompose (Eisenhauer, 1964).

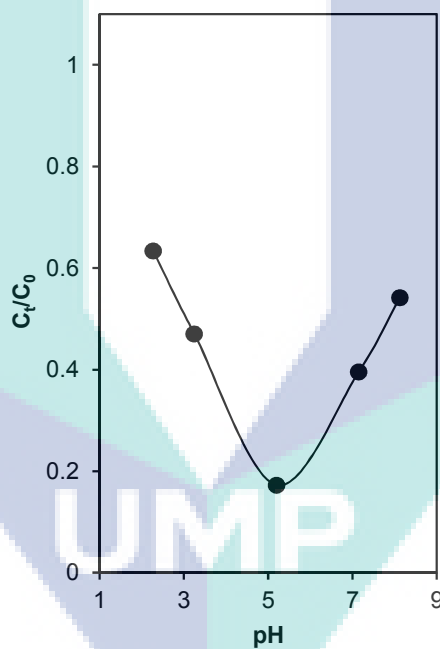


Figure 4.23 Influence of pH on 2-CP photodegradation over α -FeOOH (H_2O_2 molar concentration is 0.156 mM; catalyst dosage 0.375 g L⁻¹; initial concentration is 10 mg L⁻¹; temperature 30°C).

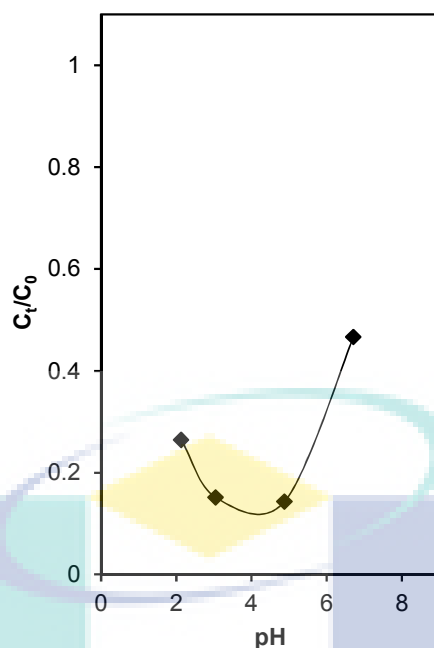


Figure 4.24 Effect of pH on 2-CP photodegradation over α -FeOOH/MSN (metal loading is 10wt%; H_2O_2 molar concentration is 0.156 mM; catalyst dosage 0.375 g L^{-1} ; initial concentration is 50 mg L^{-1} ; temperature 30°C).

4.3.4 Effect of H_2O_2 Concentration

The selection of an optimal H_2O_2 concentration for the degradation of 2-CP is important from practical point of view to its cost and toxicity (Sun *et al.*, 2007). The range of the initial concentration of H_2O_2 was varied from 1 to 10 mM and the result was shown in Figure 4.25. Meanwhile, Figure 4.26 shows the effect of the H_2O_2 concentration over α -FeOOH/MSN catalyst. It is obvious that the effect of increasing initial concentration from 0.1 to 0.5 mM was first positive for the degradation of 2-CP. This is due to the increasing OH radical amount obtained from the decomposition of H_2O_2 which improved the oxidation power. However, with further increase in H_2O_2 concentration for more than 0.156 mM, the degradation of 2-CP was decreased. This may explained by the resulting

generation of less reactive OOH radical which due to the consuming of very reactive OH radical by H_2O_2 (Kang *et al.*, 2002).

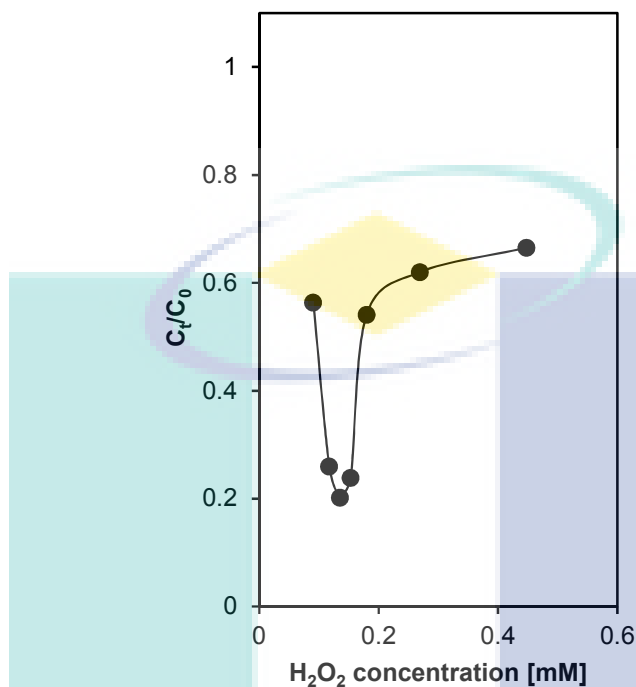


Figure 4.25 Influence of H_2O_2 molar concentration on 2-CP photodegradation over $\alpha\text{-FeOOH}$ (pH 5; catalyst dosage 0.375 g L^{-1} ; initial concentration is 10 mg L^{-1} ; temperature 30°C).

UMP

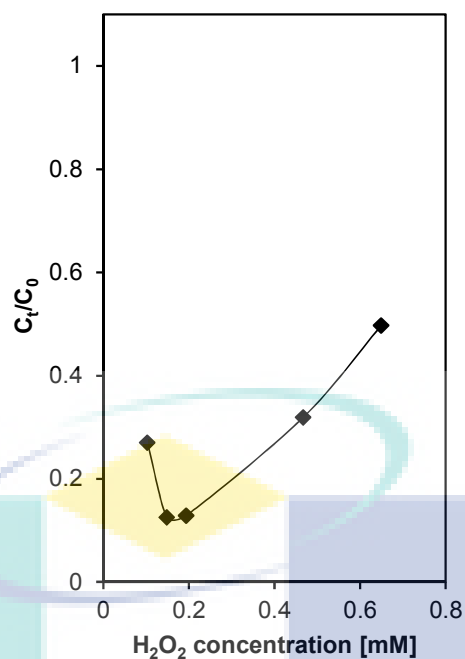


Figure 4.26 Effect of H₂O₂ molar concentration on 2-CP photodegradation over α -FeOOH/MSN (metal loading is 10wt%; catalyst dosage 0.375 g L⁻¹; initial concentration is 50 mg L⁻¹; temperature 30°C).

4.3.5 Effect of Catalyst Dosage

Figure 4.27 depicts the influence of catalyst dosage on 2-CP degradation over colloidal α -FeOOH. The result indicates the optimum dosage for 2-CP degradation was observed at 0.3 g L⁻¹ of α -FeOOH. An increase in the amount of α -FeOOH dosage will provide additional iron sites which thus accelerating the decomposition of H₂O₂. In turn, the number of hydroxyl radical was increase significantly. However, the degradation of 2-CP was declining with further increase in α -FeOOH dosage. This nature is due to the screening effect since the turbidity of the reaction mixture was increases hence subsequently reducing the optical path (Zanjanchi *et al.*, 2010b). This is in agreement with the results observed by Zhang *et al.*, (2009a).

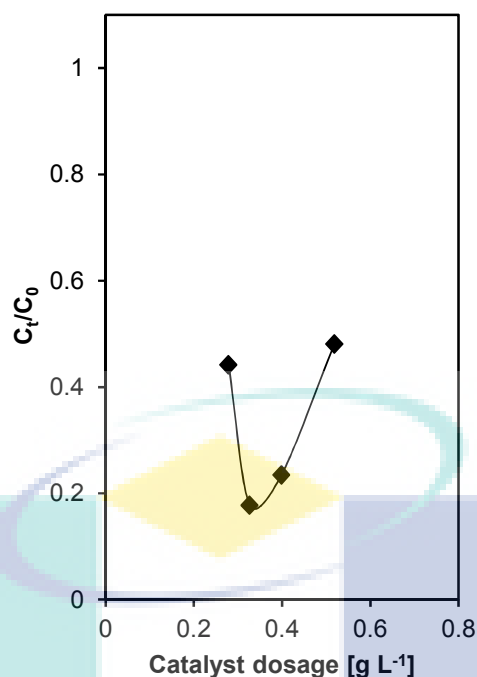


Figure 4.27 Influence of α -FeOOH dosage on 2-CP photodegradation over α -FeOOH (pH 5; H_2O_2 molar concentration is 0.156 mM; initial concentration is 10 mg L^{-1} ; temperature 30°C).

Meanwhile, Figure 4.28 shows a plot of the degradation percentage of 2-CP for 10wt% α -FeOOH/MSN catalyst. The degradation increased with increasing catalyst dosage up to 0.40 g L^{-1} , but further addition of the catalyst did not produce any significant effect on the degradation. This result was due to the increased turbidity of the suspension, which reduces light penetration and inhibits photodegradation. The increase in the catalyst dosage led to an increase in the active surface area and enhanced the degradation up to 92% (Sapawe *et al.*, 2012)

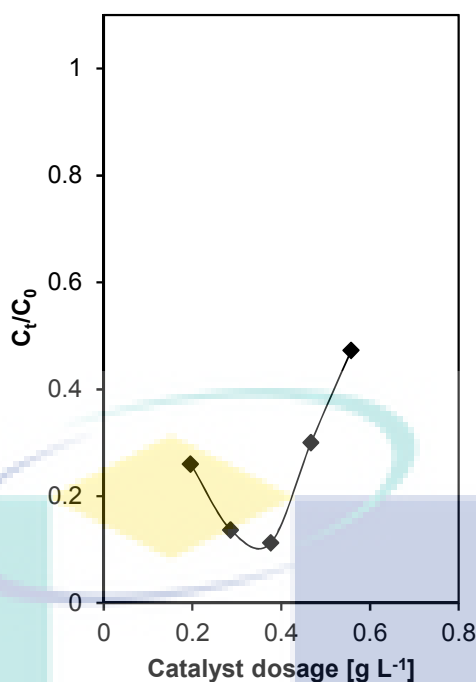


Figure 4.28 Effect of catalyst dosage on 2-CP photodegradation over α -FeOOH/MSN (metal loading is 10wt%; H₂O₂ molar concentration is 0.156 mM; initial concentration is 50 mg L⁻¹; temperature 30°C).

4.3.6 Effect of 2-CP Initial Concentration

The effectiveness of the experimental process as a function of initial concentration of 2-CP was investigated. Figure 4.29 and 4.30 shows the changes of 2-CP degradation percentage with different initial concentration of 2-CP over α -FeOOH and α -FeOOH/MSN, respectively. The results indicate that the 2-CP degradation was firstly increased with increased in initial concentration until 50 mg/L. This may due to the increased in the frequency of collisions between 2-CP molecules. Subsequently, the effective collisions frequency that causes a reaction to occur will also be high. The lifetime of hydroxyl radicals is very shorts and they can only react where they are formed. Therefore, the probability of collision between organic matter and oxidizing species will be enhanced with increasing

quantity of 2-CP molecules per volume unit, which then leading to an increase in the degradation efficiency (Kitis *et al.*, 2007).

As initial concentration of 2-CP increased to 70 mg L^{-1} , the degradation percentage of 2-CP was reduced may be due to the saturation on $\alpha\text{-FeOOH}$ surface. The generation of hydroxyl radical which important in 2-CP degradation process will be reduced since fewer active sites is available on the $\alpha\text{-FeOOH}$ surface (Laoufi and Bentahar, 2008). Similar observation was also reported by Kasiri *et al.*, (2008) in their investigation by using Fe-ZSM5 zeolite as photo-Fenton catalyst.

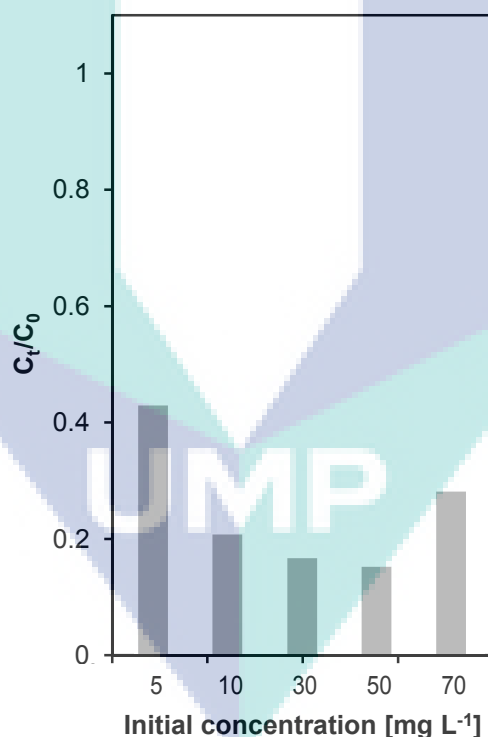


Figure 4.29 Influence of initial concentration of 2-CP on 2-CP photodegradation over $\alpha\text{-FeOOH}$ (pH 5; H_2O_2 molar concentration is 0.156 mM; catalyst dosage 0.3 g L^{-1} ; temperature 30°C).

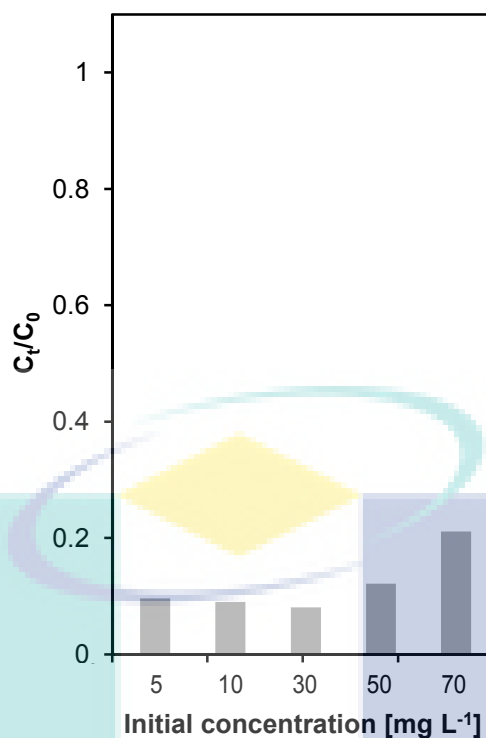


Figure 4.30 Effect of initial 2-CP concentration on 2-CP photodegradation over α -FeOOH/MSN (metal loading is 10wt%; catalyst dosage 0.4 g L⁻¹, H₂O₂ molar concentration is 0.156 mM; temperature 30°C).

4.3.7 Effect of Reaction Temperature

The influence of reaction temperature on the 2-CP degradation was investigated by varying temperature from 30°C to 50°C. The result is illustrated in Figure 4.31. It can be seen that raising the temperature has a notable positive impact on the 2-CP degradation. The degradation of 2-CP increased from 79% to 99% as the temperature increased from 30°C to 50°C.

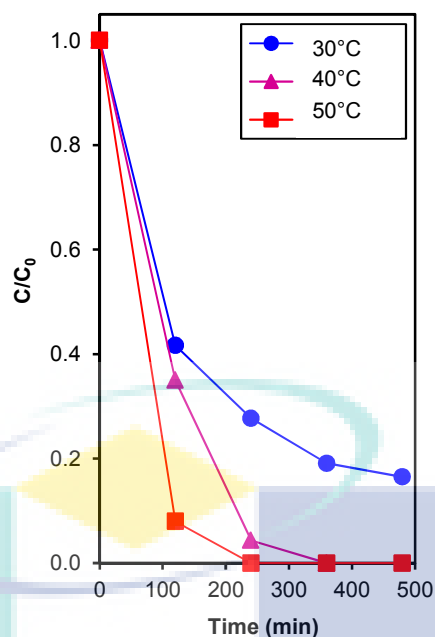


Figure 4.31 Influence of reaction temperature on 2-CP photodegradation over α -FeOOH (pH 5; H_2O_2 molar concentration is 0.156 mM; catalyst dosage 0.3 g L^{-1} ; initial concentration is 50 mg L^{-1}).

The time period required for degrading 2-CP was much shorter at 50°C which is only within 180 min compared to 30°C which required more than 480 min to achieved nearly complete degradation of 2-CP. This may due to the fact that the generation rate of oxidizing species will be accelerated since higher temperature increased the reaction rate between hydrogen peroxide and the catalyst (Sun *et al.*, 2007). Besides, more energy will be provided at higher temperature for the reactant molecules to overcome reaction activation energy (Xu *et al.*, 2009).

The influence of reaction temperature on the 2-CP degradation over α -FeOOH/MSN was investigated by varying temperature from 30 °C to 50 °C. The result is illustrated in Figure 4.32. It can be seen that raising the temperature has a notable positive impact on the 2-CP degradation. The degradation of 2-CP increased to 99% as the temperature increased from 30 to 50°C. The time period required for degrading 2-CP was much shorter at 50°C which is only within 240

min compared to 30°C which required more than 480 min to achieved nearly complete degradation of 2-CP.

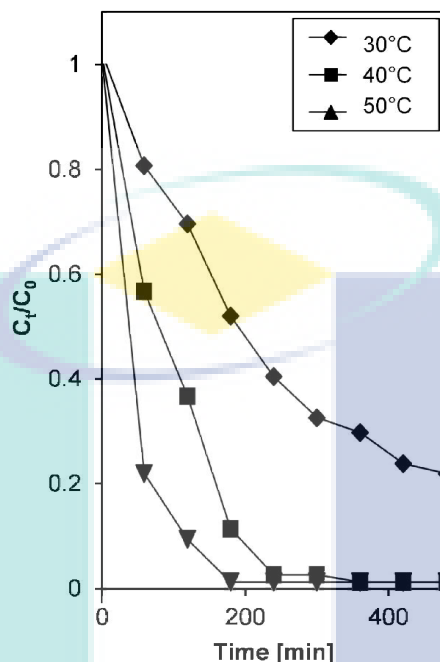


Figure 4.32 Effect of reaction temperature on 2-CP photodegradation over α -FeOOH/MSN (metal loading is 10wt%; pH is 5; catalyst dosage 0.4 g L^{-1} , H_2O_2 molar concentration is 0.156 mM ; initial concentration is 50 mg L^{-1}).

Arrhenius model often used to identify the activation energy of the catalysts. From the Arrhenius equation, a linear plot of $\ln k_{app}$ and $1/T$ would give an apparent activation energy (E_a , J mol^{-1});

$$\ln k_{app} = -\frac{E_a}{R} \frac{1}{T} + \ln A \quad (4.7)$$

where k_{app} (h^{-1}) is the apparent rate constant, A is the frequency factor, R is the gas constant ($8.314 \text{ J K mol}^{-1}$) and T is the solution temperature (K). It was observed the calculated E_a for 10 wt% α -FeOOH/MSN (Figure 4.33) is $35.57 \text{ kJ mol}^{-1}$ which is lower than 5, 10, and 15 wt% α -FeOOH loading onto MSN, signifying the effectiveness of 10 wt% α -FeOOH/MSN in this study.

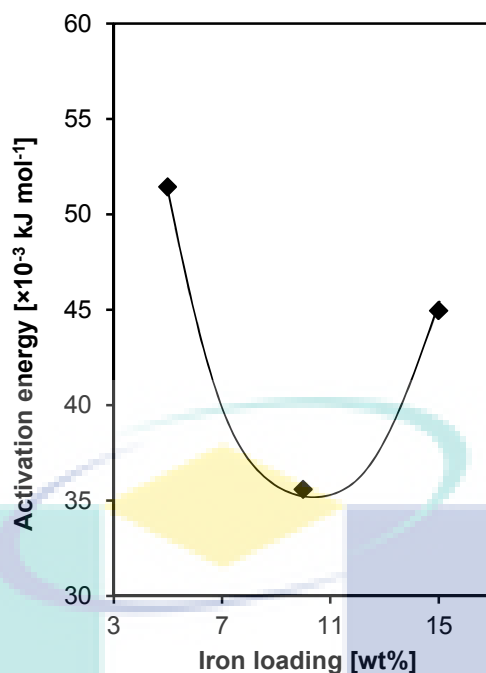


Figure 4.33 Plot of activation energy as a function of metal loading for 2-CP degradation (pH is 5; catalyst dosage 0.4 g L^{-1} , H_2O_2 molar concentration is 0.15 mM ; initial concentration is 50 mg L^{-1})

4.3.8 Proposed Catalytic Photodegradation Mechanism

Next, with the purpose of investigating the degradation mechanism of 2-CP via colloidal $\alpha\text{-FeOOH}$, the effect of scavenging agents was studied and compared with C-FeOOH . Three types of scavengers were used for both systems: potassium dichromate (PD), isopropanol (IP), and sodium oxalate (SO), with the role as a scavenger of photogenerated electrons, hydroxyl radicals ($\cdot\text{OH}$), and photogenerated holes (H^+), respectively. Figure 4.34 shows that PD underwent a similar trend of 2-CP degradation with the system using colloidal $\alpha\text{-FeOOH}$, with the highest degradation percentage of 77% after 480 min of the reaction. The degradation efficiency was reduced by half (55%) in the presence of IP, while the addition of SO had significantly decreased the degradation efficiency of 2-CP,

confirming the photogenerated hole is the main oxidation species for degrading the 2-CP.

For the case of PD, although the photo-induced electrons at the conduction band have been captured, $\cdot\text{OH}$ could still be produced via direct photoconversion of H_2O_2 (Eq. 4.8) to degrade the 2-CP.



In addition, the high oxidation potential of the holes at the valence band (h^+_{VB}) in the $\alpha\text{-FeOOH}$ also permits the direct oxidation of 2-CP to reactive intermediates (Eq. 4.9),



The addition of IP to the system shows a rather lower degradation percentage than PD. In fact, $\cdot\text{OH}$ could be generated via direct photoconversion of H_2O_2 (Eq. 4.8) or photogenerated electron-induced multistep reduction of O_2 (Eq. 4.10–4.12).



Thus, trapping the important source $\cdot\text{OH}$ in the reaction leaving the direct oxidation shown in Eq. 4.8 was the only way to degrade the 2-CP.

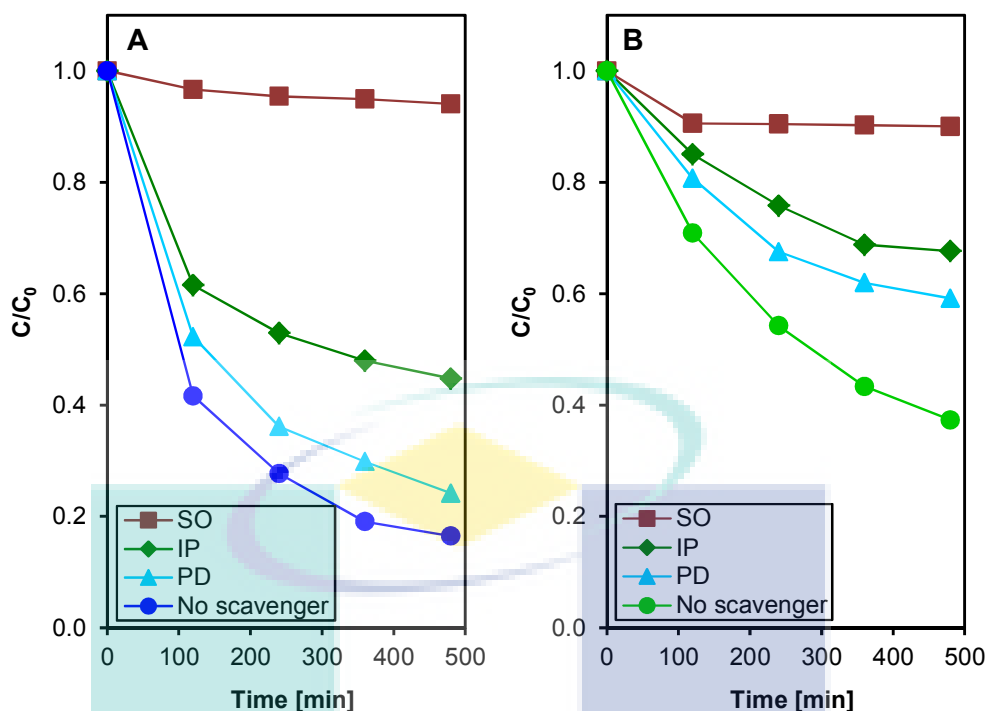


Figure 4.34 Photodegradation efficiencies of 2-CP in the presence of hole scavenger, \bullet OH scavenger, and electron scavenger by (A) α -FeOOH and (B) C-FeOOH [pH 5, H_2O_2 concentration 0.156 mM; catalyst dosage 0.30 g L⁻¹; initial concentration 50 mg L⁻¹; temperature 303 K].

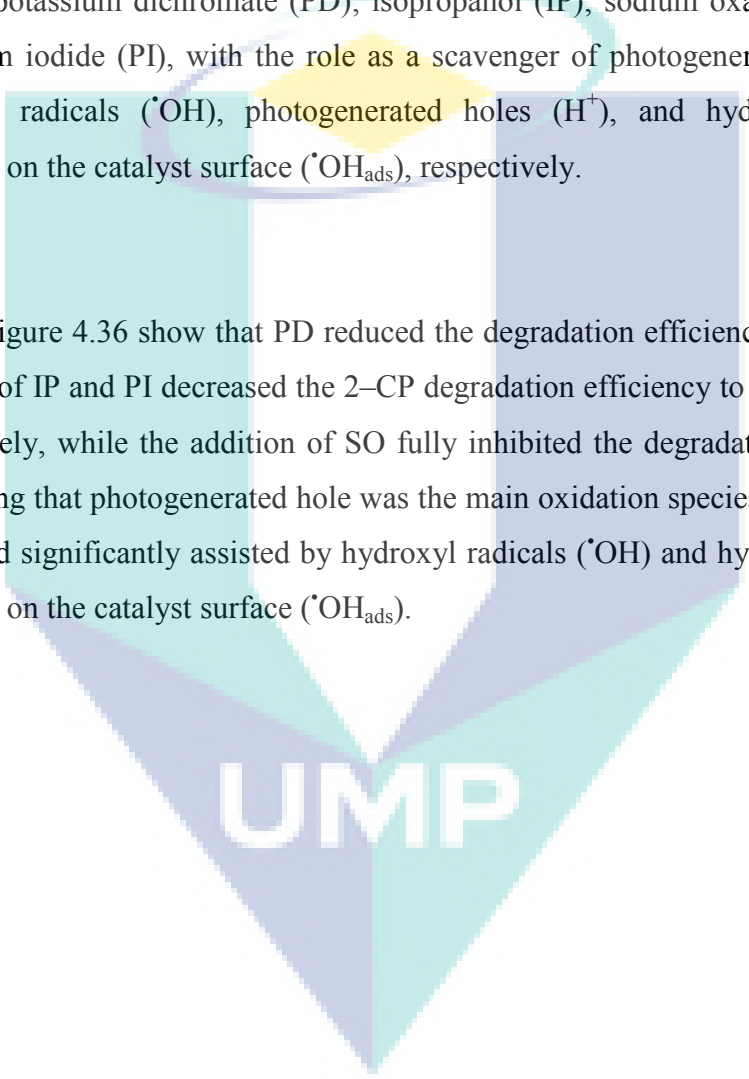
From the above results, it can be concluded that photogenerated holes play the most important role in the 2-CP degradation via α -FeOOH catalyst. It was verified that the headgroups of cationic surfactant reverse micelle inhibited the recombination of photo-induced electron-hole pairs in the system. Wang and his co-workers also reported a similar phenomenon on visible light photocatalysis using bismuth oxyiodide (BiOI) modified by cationic surfactant solution.

Figure 4.34B shows that a similar trend was also observed when using the C-FeOOH, but with a comparatively lower degradation percentage of 2-CP in all cases of scavengers studied. The absence of cationic surfactant in the system might be the main reason for the lower effectiveness of the C-FeOOH. It could be seen that the photogenerated holes also play an important role in this study,

followed by $\cdot\text{OH}$ and photogenerated electrons. The proposed electron trapping occurrences for both catalysts are illustrated in Figure 4.35.

Next, with the purpose of investigating the mechanism of 2-CP degradation via $\alpha\text{-FeOOH/MSN}$, the effect of scavenging agents was studied by using 10 wt% $\alpha\text{-FeOOH/MSN}$. Four types of scavengers were used for the system: potassium dichromate (PD); isopropanol (IP); sodium oxalate (SO); and potassium iodide (PI), with the role as a scavenger of photogenerated electrons, hydroxyl radicals ($\cdot\text{OH}$), photogenerated holes (h^+), and hydroxyl radicals adsorbed on the catalyst surface ($\cdot\text{OH}_{\text{ads}}$), respectively.

Figure 4.36 show that PD reduced the degradation efficiency to 59%. The addition of IP and PI decreased the 2-CP degradation efficiency to 16% and 18%, respectively, while the addition of SO fully inhibited the degradation efficiency, confirming that photogenerated hole was the main oxidation species for degrading 2-CP and significantly assisted by hydroxyl radicals ($\cdot\text{OH}$) and hydroxyl radicals adsorbed on the catalyst surface ($\cdot\text{OH}_{\text{ads}}$).



UMP

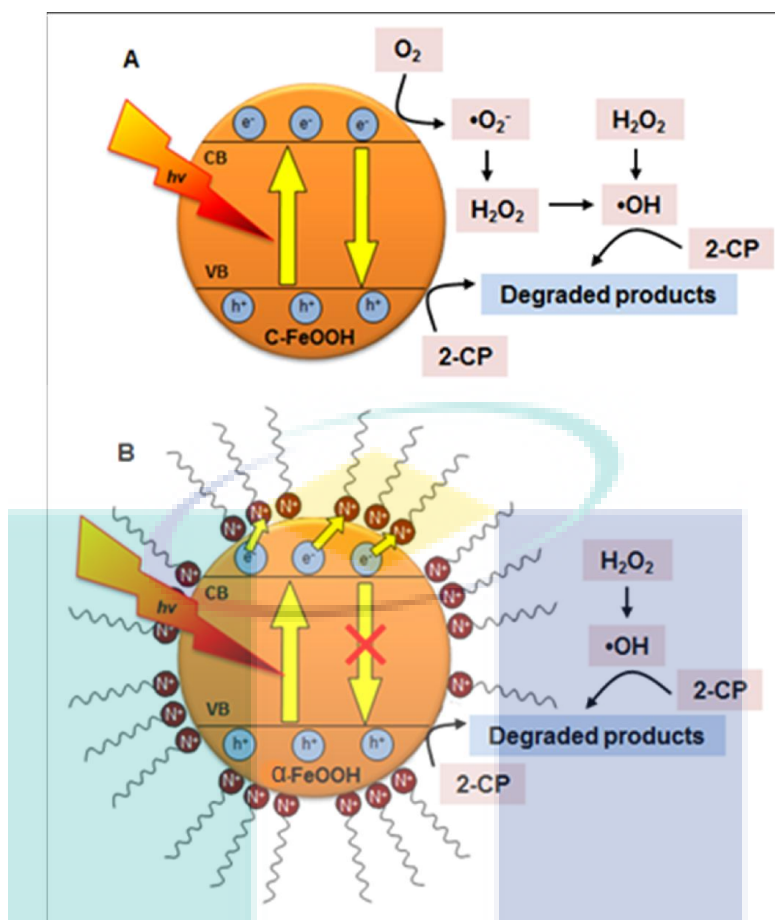


Figure 4.35 Schematic illustration of 2-CP photodegradation over (A) C-FeOOH, and (B) photogenerated electron trapping by cationic surfactant headgroups of α -FeOOH

As proposed in Figure 4.37, both type of the iron species played role in the photocatalytic process. The α -FeOOH could trap the photogenerated electron by the colloidal structure around the α -FeOOH. Meanwhile, the substituted Fe species may inhibit the electron-hole recombination by transferring the photoinduced electron to the support as MSN could also acts as stable electron acceptors. As proven by SO, the photogenerated holes (h^+_{VB}) at the valence band, which have high oxidation potential, play two important roles in this degradation. Firstly, they permit the direct oxidation of 2-CP to reactive intermediates (Eq. 4.13):



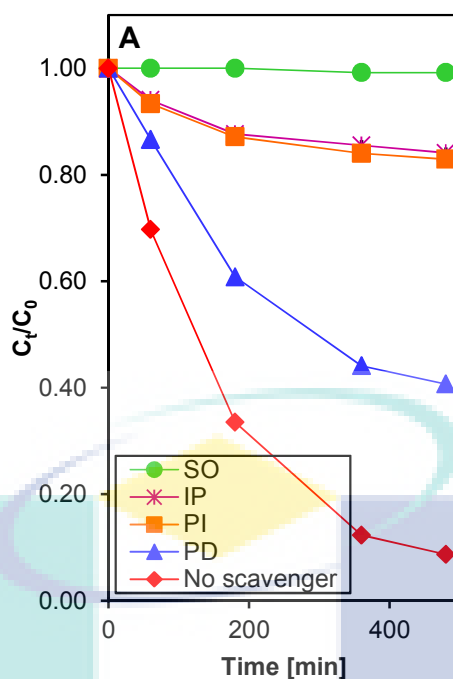
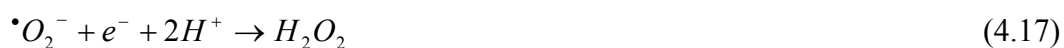


Figure 4.36 Photodegradation efficiencies of 2-CP in the presence of hole scavenger, $\cdot\text{OH}$ scavenger, electron scavenger, and $\cdot\text{OH}_{\text{ads}}$ scavenger by 10 wt% $\alpha\text{-FeOOH/MSN}$ catalyst [pH 5; H_2O_2 concentration is 0.156 mM, catalyst dosage 0.40 g L⁻¹; initial concentration is 50 mg L⁻¹]

Secondly, h^+_{VB} also react with surface-adsorbed hydroxyl groups (OH^-) or water to yield surface-adsorbed hydroxyl radicals ($\cdot\text{OH}_{\text{ads}}$), which subsequently degrade the 2-CP, as shown by the decrease in degradation efficiency by PI (Eq. 4.14):



The addition of IP showed a rather lower degradation percentage, indicating a significant role of $\cdot\text{OH}$ in the system. In fact, $\cdot\text{OH}$ could be generated via direct photoconversion of H_2O_2 (Eq. 4.15) or by photogenerated electron-induced multistep reduction of O_2 (Eqs. 4.16–4.18) to degrade the 2-CP:



In the case of PD, although the photo-induced electrons at the conduction band have been captured by PD, $\cdot OH$ could still be produced by direct photoconversion of H_2O_2 (Eq. 4.15). Therefore, this mechanism demonstrates the significant role of the silica support as an acceptor of photo-induced electrons to efficiently inhibit the recombination of electron-hole pairs that leads to enhanced degradation of 2-CP.

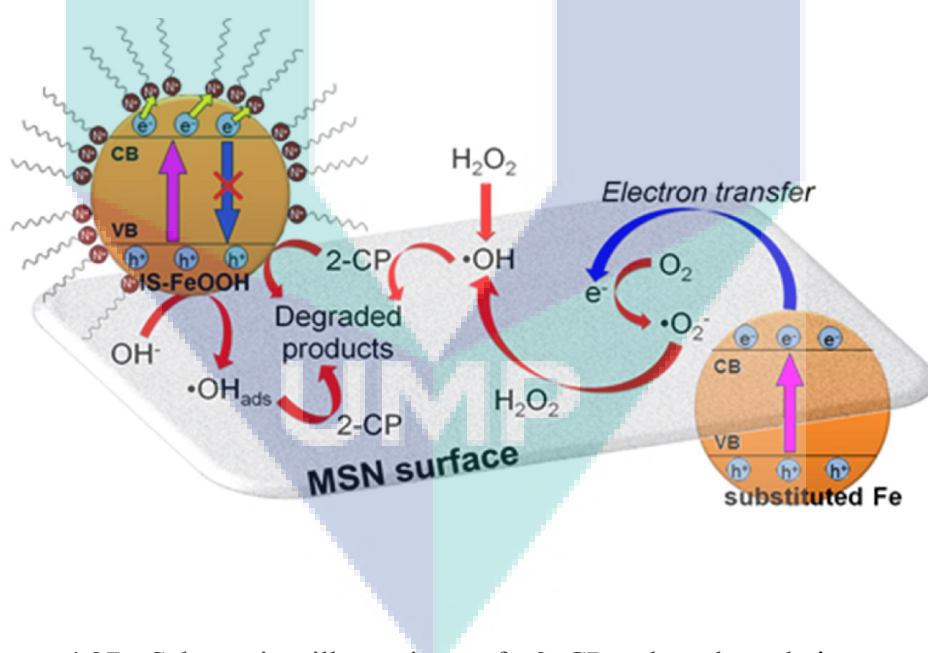


Figure 4.37 Schematic illustration of 2-CP photodegradation over α -FeOOH/MSN

4.4 Response Surface Methodology

Optimization on photocatalytic activity of α -FeOOH was studied using sequential response surface methodology (RSM). To determine the optimum operating variables, it is necessary to perform a factorial experiment that is more likely a screening process. There are a total 20 runs (Table 4.3) for factorial experiments with 4 variables which are temperature (X_1), catalyst dosage (X_2), $H_2O_2/2$ -CP ratio (X_3), and pH (X_4).

Table 4.3 Response for two-level factorial of four variables (X_1 – X_4)

Run	Variables				Response (%)
	X_1	X_2	X_3	X_4	
1	50	0.25	0.2	3	75.33
2	40	0.31	0.4	5	98.64
3	40	0.31	0.4	5	95.00
4	30	0.38	0.2	7	40.91
5	50	0.25	0.2	7	75.65
6	30	0.38	0.2	3	36.21
7	50	0.25	0.6	7	88.55
8	50	0.38	0.6	7	72.33
9	30	0.25	0.2	3	49.54
10	40	0.31	0.4	5	98.97
11	30	0.38	0.6	7	24.07
12	30	0.38	0.6	3	25.7
13	30	0.25	0.6	7	59.13
14	50	0.38	0.6	3	78.59
15	50	0.38	0.2	7	84.3
16	50	0.25	0.6	3	85.22
17	30	0.25	0.2	7	62.75
18	30	0.25	0.6	3	52.61
19	40	0.31	0.4	5	97.67
20	50	0.38	0.2	3	85.03

From ANOVA analysis, it was determined that the model F-value is 76.74 which implies the model is significant. There is only a 0.01 % chance that the F-value may occur due to noise. Other than that, the values of Prob>F less than 0.0500 indicate model terms are significant. In this study, catalyst dosage and temperature is the significant factor. There is also a significant interaction between catalyst dosage and $H_2O_2/2-CP$ ratio and also between catalyst dosage and temperature.

From the full factorial experiments, it can be seen that pH is not an influential factor in this study. In addition, it was observed that there is no interaction between pH and other variables. This is in agreement with the fact that $\alpha-FeOOH$ have a wide operating pH in nature (Ortiz de la Plata, 2008). Therefore, it is possible that pH is not giving much influence on the photocatalytic reaction.

Other than that, the curvature value of 221.71 implies that there is a significant curvature in the design space. Moreover, the R^2 value of 0.97 indicates that the model is significant. Therefore, it is confirmed that the region of the optimum conditions is within the parameters such as catalyst dosage, $H_2O_2/2-CP$ ratio, and temperature. In order to obtain more precise estimate of optimum operating conditions, second experiment was performed.

The objective of this second experiment is to develop an empirical model of the process and to obtain a more precise estimate of the optimum operating conditions. This second experimental design is called central composite design (CCD). There were a total of 29 runs for optimizing the three individual parameters in the CCD which are catalyst dosage, $H_2O_2/2-CP$ ratio, and temperature, after the elimination of pH due to its insignificant effects (Table 4.4).

Table 4.4 Response for central composite design (CCD)

Run	Variables			Response (%)
	X ₁	X ₂	X ₃	
1	30	0.38	0.6	25.7
2	50	0.38	0.2	85.03
3	50	0.25	0.6	85.22
4	30	0.38	0.2	36.01
5	30	0.25	0.6	52.61
6	40	0.31	0.4	95.00
7	40	0.31	0.4	98.64
8	30	0.38	0.6	24.07
9	30	0.25	0.2	49.54
10	30	0.38	0.2	40.91
11	40	0.31	0.4	97.67
12	50	0.38	0.6	78.59
13	50	0.25	0.6	88.55
14	40	0.31	0.4	98.97
15	50	0.25	0.2	75.33
16	50	0.38	0.6	72.33
17	30	0.25	0.2	62.57
18	50	0.38	0.2	84.3
19	30	0.25	0.6	59.13
20	50	0.25	0.2	75.65
21	30	0.31	0.4	79.31
22	40	0.25	0.4	85.31
23	40	0.31	0.6	86.54
24	40	0.31	0.4	87.52
25	40	0.31	0.4	93.49
26	40	0.31	0.4	96.70
27	40	0.38	0.4	87.54
28	40	0.31	0.2	85.04
29	50	0.31	0.4	96.76

The analysis of variance (ANOVA) for the response surface model was shown in Table 4.5. The significance of the regression model was checked by F-test and p-value. The p-values were used to check the significance of each coefficient. The more significant the corresponding coefficient will be indicates

by smaller p-value. The determination coefficient ($R^2 = 0.9596$), showed by ANOVA of the regression model, indicating that within the range of experimental variables, the model was adequate for prediction.

Table 4.5 ANOVA of photodegradation of 2-CP by α -FeOOH

Source	Sum of Squares	df	Mean Square	F Value	p-value Prob > F
Model	201828768.79	8	25228596.10	59.35	< 0.0001
A- Temp	74835855.32	1	74835855.32	176.04	< 0.0001
B-CD	3961116.00	1	3961116.00	9.32	0.0063
C-Ratio	35541.89	1	35541.89	0.08	0.7754
AB	3395411.04	1	3395411.04	7.99	0.0104
BC	3860933.35	1	3860933.35	9.08	0.0069
A ²	4550411.19	1	4550411.19	10.70	0.0038
B ²	7296855.96	1	7296855.96	17.16	0.0005
C ²	8279246.06	1	8279246.06	19.48	0.0003
Residual	8502082.40	20	425104.12		
Total	210330851.20	28			

The important information on the model performance is summarized in residuals providing a clear view for any discrepancy in fit to the model. Hence, the normal probability plot of residuals and the plot of internally studentized residuals vs. predicted values are presented in Figure 4.38 and Figure 4.39, respectively. It can be seen that points or point clusters are placed closely to the diagonal line in Figure 4.38, leading to the conclusions that there are no serious violations in the assumptions that errors are normally distributed and independent of each other, which the error variances are homogeneous and that residuals are independent (Idris *et al.*, 2006a).

The plot presented in Figure 4.39 tests the assumption of constant variance. The points are randomly scattered and all values lie within the range of -3 and +3. The high correlation between observed and predicted data can be seen from the graphical interpretation given in Figure 4.40. It is evident that the points or point clusters are placed very closely to the diagonal line as a result of their low

discrepancies. According to the layouts of the plots presented in Figure 4.38 to 4.40, it was concluded that there was no apparent problem with normality, and that the model is successful in capturing the correlation between the influencing parameters of studied system.

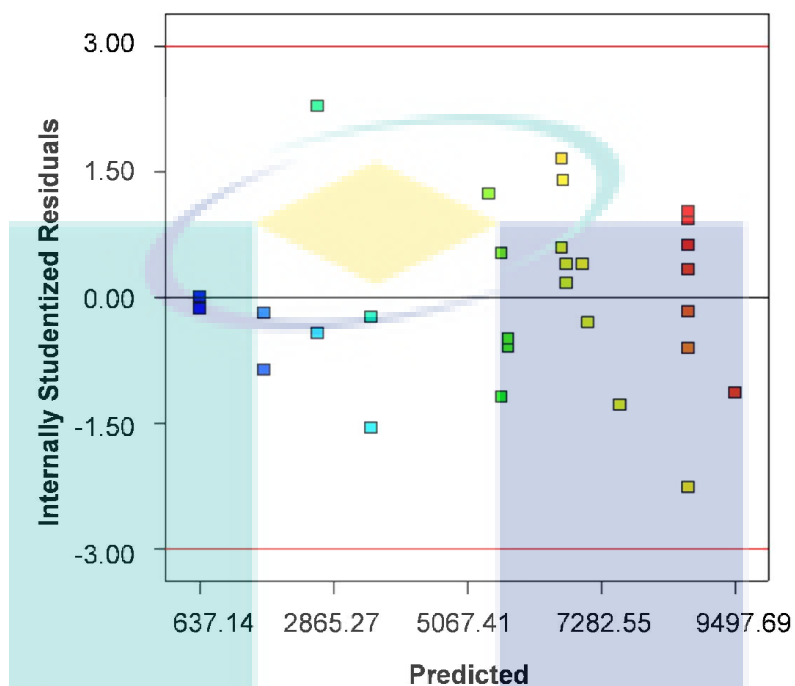


Figure 4.38 The studentized residuals and predicted response plot for 2-CP photodegradation.

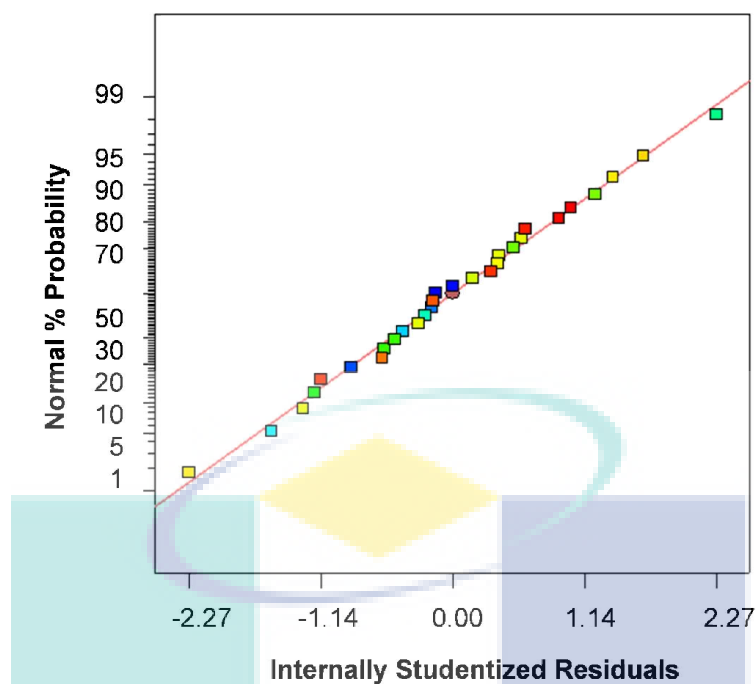


Figure 4.39 Normal % probability and studentized residual plot for 2-CP photodegradation

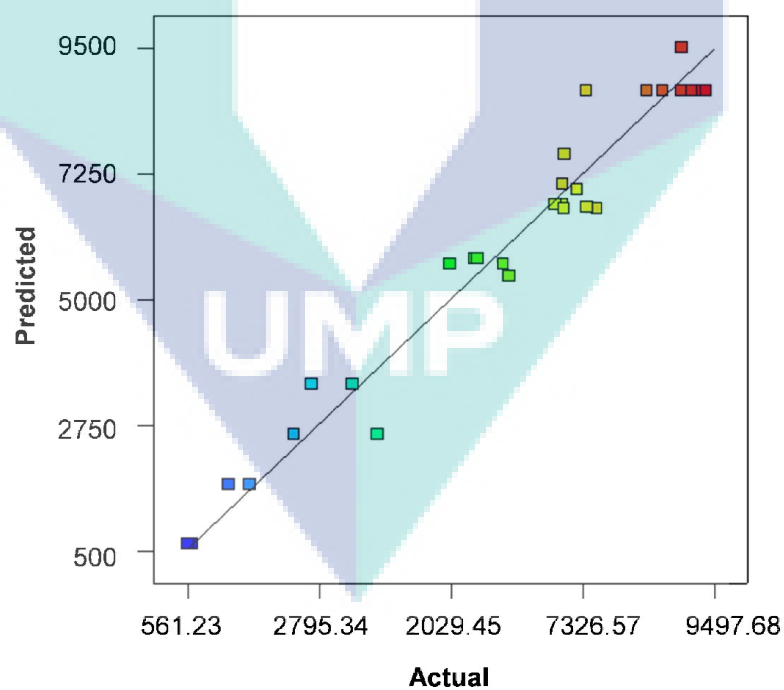


Figure 4.40 The actual and predicted plot for 2-CP photodegradation.

The 3-D response surface plot were developed for the 2-CP photodegradation by α -FeOOH as shown in Figure 4.41 with varying catalyst

dosage and reaction temperature. It indicated that the maximum 2-CP photodegradation can be achieved when catalyst dosage and temperature were at the threshold level of 0.33 g L^{-1} and 40°C , respectively.

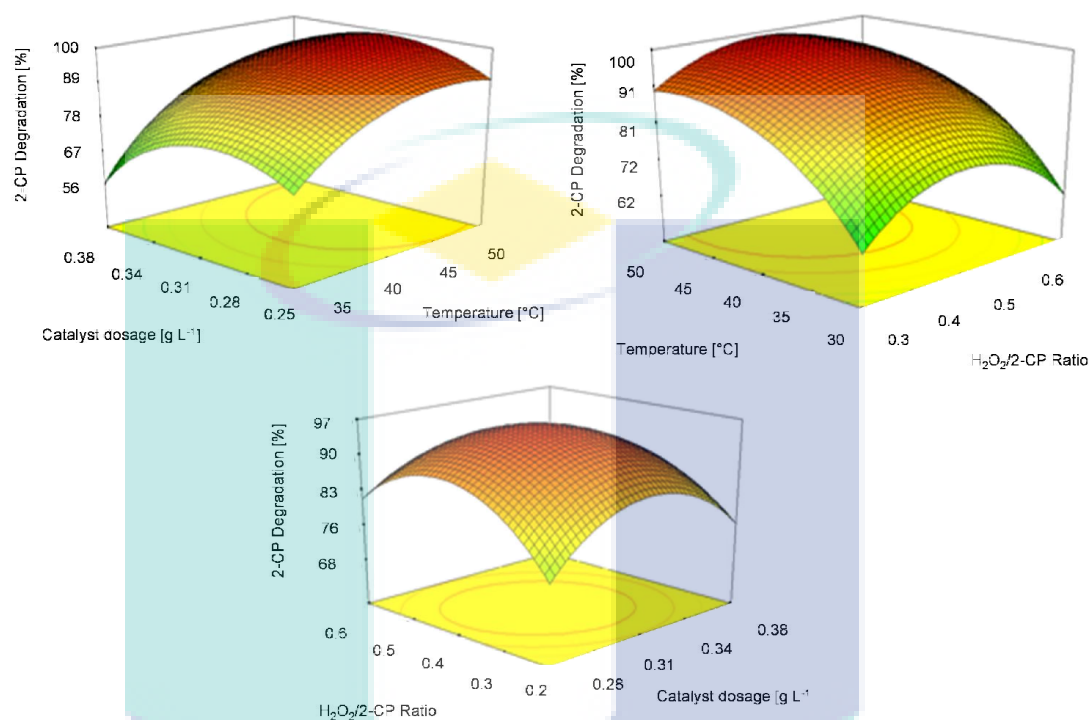


Figure 4.41 3D response plot showing effect of temperature, catalyst dosage, and $\text{H}_2\text{O}_2/2\text{-CP}$ ratio at fixed pH.

The generated relationship between response and operating variables are as follows:

$$Y = -59986.25 + 988.28X_1 + 1178608.39X_2 + 46276.62X_3 + 3685.33X_1X_2 - 196492.58X_2X_3 - 12.68X_1^2 - 10279624.83X_2^2 - 42772.52X_3^2 \quad (4.19)$$

where Y is the percentage of 2-CP photodegradation, X_1 is temperature, X_2 is catalyst dosage, and X_3 is $\text{H}_2\text{O}_2/2\text{-CP}$ ratio.

The optimum operating variables for the α -FeOOH/MSN was determined using the same method. There are a total 36 runs (Table 4.6) for factorial experiments with 5 variables which are metal loading (*A*), pH (*B*), catalyst dosage (*C*), H₂O₂ concentration (*D*), and temperature (*E*).

Table 4.6 Response for two-level factorial of five variables

Run	Variables					Response (%)
	A	B	C	D	E	
1	5	3	0.1	0.2	30	61.52
2	15	3	0.1	0.2	30	55.35
3	5	7	0.1	0.2	30	72.00
4	15	7	0.1	0.2	30	61.44
5	5	3	0.2	0.2	30	37.75
6	15	3	0.2	0.2	30	71.31
7	5	7	0.2	0.2	30	68.89
8	15	7	0.2	0.2	30	79.56
9	5	3	0.1	0.6	30	61.4
10	15	3	0.1	0.6	30	44.32
11	5	7	0.1	0.6	30	76.00
12	15	7	0.1	0.6	30	79.33
13	5	3	0.2	0.6	30	37.89
14	15	3	0.2	0.6	30	45.53
15	5	7	0.2	0.6	30	81.33
16	15	7	0.2	0.6	30	81.44
17	5	3	0.1	0.2	50	92.25
18	15	3	0.1	0.2	50	95.76
19	5	7	0.1	0.2	50	98.67
20	15	7	0.1	0.2	50	98.50
21	5	3	0.2	0.2	50	98.36
22	15	3	0.2	0.2	50	96.90
23	5	7	0.2	0.2	50	94.11
24	15	7	0.2	0.2	50	97.78
25	5	3	0.1	0.6	50	96.35
26	15	3	0.1	0.6	50	91.95
27	5	7	0.1	0.6	50	93.89
28	15	7	0.1	0.6	50	95.78
29	5	3	0.2	0.6	50	96.14

Continued

Run	Variables					Response (%)
	A	B	C	D	E	
30	15	3	0.2	0.6	50	70.23
31	5	7	0.2	0.6	50	92.89
32	15	7	0.2	0.6	50	98.67
33	10	5	0.15	0.4	40	95.71
34	10	5	0.15	0.4	40	94.73
35	10	5	0.15	0.4	40	90.25
36	10	5	0.15	0.4	40	89.51
30	15	3	0.2	0.6	50	70.23
31	5	7	0.2	0.6	50	92.89
32	15	7	0.2	0.6	50	98.67
33	10	5	0.15	0.4	40	95.71
34	10	5	0.15	0.4	40	94.73
35	10	5	0.15	0.4	40	90.25
36	10	5	0.15	0.4	40	89.51

From ANOVA analysis, it was determined that the model F-value is 18.40 which implies the model is significant. There is only a 0.01 % chance that the F-value may occur due to noise. Other than that, the values of Prob>F less than 0.0500 indicate model terms are significant. In this study, pH and temperature is the significant factor. There is also a significant interaction between pH and temperature and also between metal loading, H₂O₂ concentration, and temperature.

Other than that, the curvature value of 10.70 implies that there is a significant curvature in the design space. Moreover, the R² value of 0.89 indicates that the model is significant. In order to obtain more precise estimate of optimum operating conditions, second experiment was performed.

The objective of this second experiment is to develop an empirical model of the process and to obtain a more precise estimate of the optimum operating conditions. This second experimental design is called central composite design (CCD). There were a total of 48 runs for optimizing the three individual parameters in the CCD which are metal loading (*A*), pH (*B*), H₂O₂ concentration (*C*), and temperature (*D*), after the elimination of catalyst dosage due to its insignificant effects (Table 4.7).

Table 4.7 Central composite design of experiments of four variables

Run	Variables				Response (%)
	A	B	C	D	
1	5	3	0.1	30	61.52
2	5	3	0.1	30	61.40
3	15	3	0.1	30	55.35
4	15	3	0.1	30	44.32
5	5	7	0.1	30	72.00
6	5	7	0.1	30	76.00
7	15	7	0.1	30	61.44
8	15	7	0.1	30	79.33
9	5	3	0.2	30	37.75
10	5	3	0.2	30	37.89
11	15	3	0.2	30	71.31
12	15	3	0.2	30	45.53
13	5	7	0.2	30	68.89
14	5	7	0.2	30	81.33
15	15	7	0.2	30	79.56
16	15	7	0.2	30	81.44
17	5	3	0.1	50	92.25
18	5	3	0.1	50	96.35
19	15	3	0.1	50	95.76
20	15	3	0.1	50	91.95
21	5	7	0.1	50	98.67
22	5	7	0.1	50	93.89
23	15	7	0.1	50	98.50
24	15	7	0.1	50	95.78
25	5	3	0.2	50	98.36

Continued

Run	Variables				Response (%)
	A	B	C	D	
26	5	3	0.2	50	96.14
27	15	3	0.2	50	96.9
28	15	3	0.2	50	70.23
29	5	7	0.2	50	94.11
30	5	7	0.2	50	92.89
31	15	7	0.2	50	97.78
32	15	7	0.2	50	98.67
33	10	5	0.15	40	95.71
34	10	5	0.15	40	94.73
35	10	5	0.15	40	90.25
36	10	5	0.15	40	89.51
37	5	5	0.15	40	85.92
38	15	5	0.15	40	90.90
39	10	3	0.15	40	77.04
40	10	7	0.15	40	57.14
41	10	5	0.1	40	74.57
42	10	5	0.2	40	88.59
43	10	5	0.15	30	91.29
44	10	5	0.15	50	97.50
45	10	5	0.15	40	94.61
46	10	5	0.15	40	92.78
47	10	5	0.15	40	92.51
48	10	5	0.15	40	95.80

In order to ensure a good model, tests for the significance of the regression model and individual model coefficients as well as for lack-of-fit were performed. The summary of the tests is tabulated in an analysis of variance (ANOVA) table shown in Table 4.8. The value of “Prob.>F” for the model is less than 0.05, indicating that the terms in the model have a significant effect on the response. In the same manner, the main effects of pH (*B*), reaction temperature (*D*), the two-level interaction of pH and reaction temperature (*BD*), and the second-order effect of pH (B^2) and reaction temperature (D^2) were significant model terms. The least significant model term, the H₂O₂ concentration (*C*), was

removed to generate an improved model. Additionally, the value of lack-of-fit was found to be insignificant, indicating that desirable fitness of the model was achieved.

Table 4.8 Analysis of variance (ANOVA) for central composite design for α -FeOOH /MSN catalyst

Source	Sum of Squares	df	Mean Square	F Value	p-value Prob > F
Model	6104.280513	14	436.0200366	26.53897534	< 0.0001
A	29.57423824	1	29.57423824	1.800077779	0.1891
B	354.7186	1	354.7186	21.59044858	< 0.0001
C	0.008261765	1	0.008261765	0.000502864	0.9822
D	4467.566694	1	4467.566694	271.9247566	< 0.0001
AB	47.50687813	1	47.50687813	2.891573233	0.0987
AC	24.48250313	1	24.48250313	1.490162131	0.2311
AD	38.65402812	1	38.65402812	2.352732015	0.1349
BC	7.210503125	1	7.210503125	0.438877456	0.5124
BD	118.6185031	1	118.6185031	7.219882724	0.0113
CD	0.219453125	1	0.219453125	0.013357324	0.9087
A ²	0.009982146	1	0.009982146	0.000607577	0.9805
B ²	687.5321298	1	687.5321298	41.84761411	< 0.0001
C ²	3.538667861	1	3.538667861	0.215386017	0.6457
D ²	109.4211964	1	109.4211964	6.660075662	0.0147
Residual	525.7415176	32	16.42942243		
Lack of Fit	266.2185676	10	26.62185676	2.256759368	0.0536
Pure Error	259.52295	22	11.79649773		
Cor Total	6811.485381	47			

Table 4.9 shows the ANOVA table for the reduced quadratic model of 2-CP degradation by selecting the backward elimination procedure to automatically reduce the terms that are not significant. The results shows that the model is still significant with the main effects of pH (B), reaction temperature (D), the two-level interaction of pH and reaction temperature (BD), and the second-order effect of pH (B^2) and reaction temperature (D^2). The main effect of α -FeOOH metal loading (A) was additionally added to support the model hierarchy. It was found that both pH (B) and reaction temperature (D) were the most significant factors for the removal of 2-CP.

Table 4.9 Analysis of variance (ANOVA) for central composite design for α -FeOOH /MSN catalyst (reduced)

Source	Sum of Squares	df	Mean Square	F Value	p-value Prob > F
Model	6029.976	7	861.4252	55.98839	< 0.0001
A	29.57424	1	29.57424	1.922179	0.1735
B	354.7186	1	354.7186	23.05496	< 0.0001
D	4467.567	1	4467.567	290.3698	< 0.0001
AB	47.50688	1	47.50688	3.087713	0.0867
BD	118.6185	1	118.6185	7.709617	0.0084
B^2	916.8986	1	916.8986	59.59388	< 0.0001
D^2	121.2125	1	121.2125	7.878212	0.0078
Residual	600.0456	39	15.38578		
Lack of Fit	340.5226	17	20.03074	1.698025	0.1209
Pure Error	259.523	22	11.7965		
Cor Total	6811.485	47			

The R^2 value calculated for the model was 0.909, implying that about 90.9% of the variability in the data is explained by the model. The predicted R^2 was

found to be in reasonable agreement with the adjusted R^2 , as the adjusted R^2 value is particularly useful when comparing models with different numbers of terms. This comparison is, however, done in the background when model reduction is taking place. Meanwhile, adequate precision compares the range of the predicted values at the design points to the average prediction error. The ratios obtained for this model were greater than 4, indicating adequate model discrimination. The final empirical model in terms of actual factors is depicted in Eq. 4.20.

$$\begin{aligned}
 &2-CP \text{ degradation (\%)} \\
 &= 15.21759578 - 0.422689338 A + 46.34192434 B - 3.270061968 D \\
 &+ 0.12184375 AB - 0.096265625 BD - 4.20947368 A^2 \\
 &+ 0.061221053 D^2
 \end{aligned} \tag{4.20}$$

The normal probability plot of the residuals and the plot of the residuals versus the predicted response for 2-CP degradation are shown in Figure 4.42. The result reveals that the residuals generally fall on a straight line, implying that the errors are distributed normally; this supports the adequacy of the least-square fit. Figure 4.43 indicates no obvious pattern and unusual structure, besides showing equal scatter above and below the x -axis. This implies that the proposed model is adequate and there is no reason to suspect any violation of the independence or constant variance assumption.

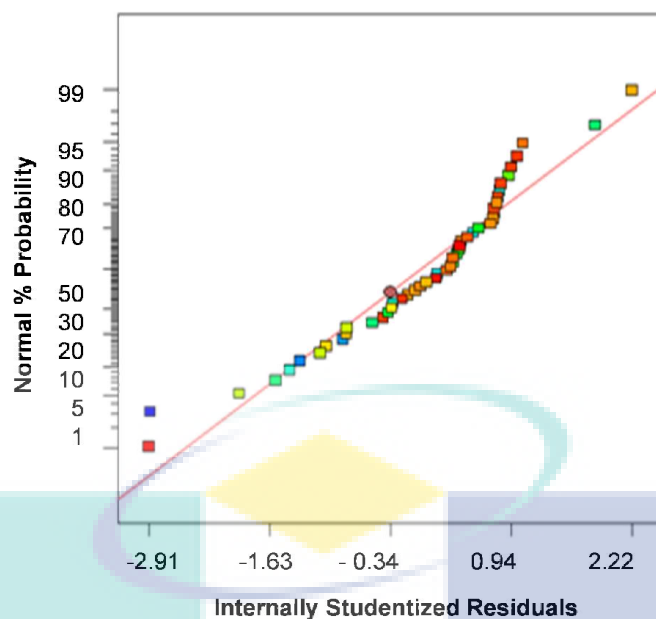


Figure 4.42 Residual diagnostics for 2-CP photodegradation of normal probability plot

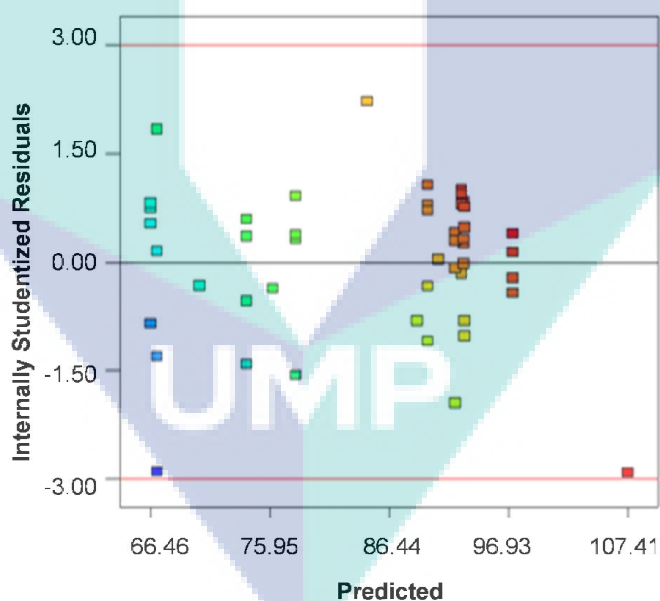
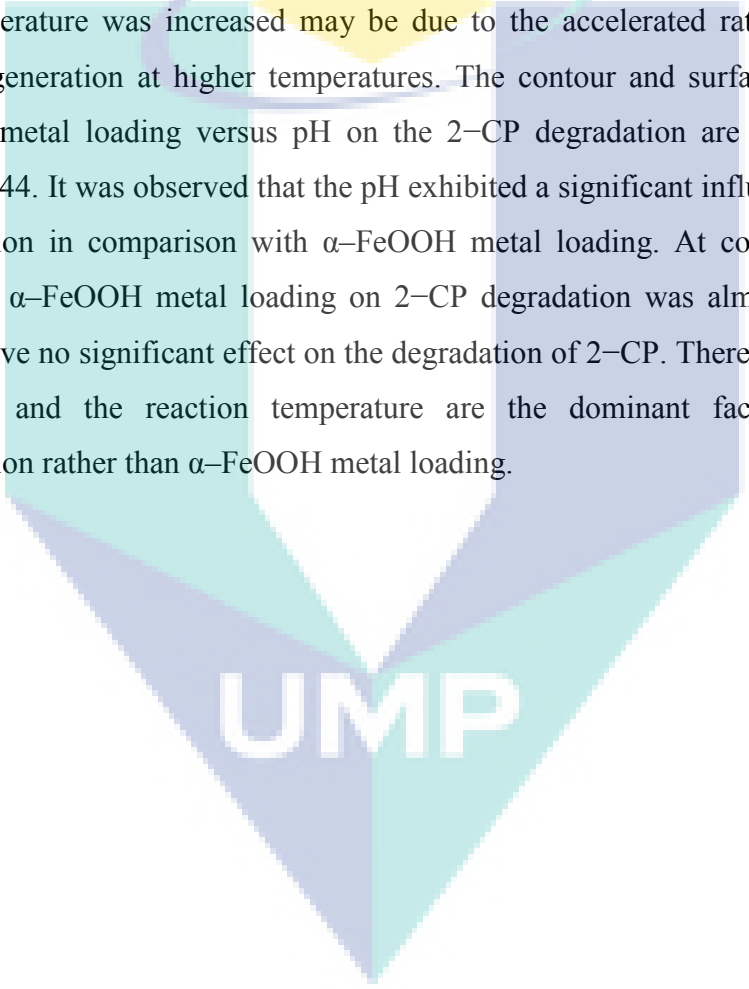


Figure 4.43 Residual diagnostics for 2-CP photodegradation of residual vs. predicted response plot.

The three dimensional surface plots demonstrate the effect of different process variables on 2-CP degradation (Figure 4.44). The effect of pH (*B*) and temperature (*D*), while keeping α -FeOOH loading (*A*) at the middle level (10

wt%), is clearly seen in Figure 4.36A and Figure 4.36B. The degradation of 2-CP increased when the pH changed from 3 to 5.11 and the temperature increased from 30 to 49.94°C. The maximum 2-CP degradation of 99.99% was observed when the pH was 5.11 and temperature was 49.94°C.

This result could be explained by the decomposition of H_2O_2 at elevated pH. Furthermore, the oxidation potential of $\cdot OH$ was found to be decrease with increasing pH. Meanwhile, a significant enhancement in 2-CP degradation when the temperature was increased may be due to the accelerated rate of oxidizing species generation at higher temperatures. The contour and surface plots of α -FeOOH metal loading versus pH on the 2-CP degradation are represented in Figure 4.44. It was observed that the pH exhibited a significant influence on 2-CP degradation in comparison with α -FeOOH metal loading. At constant pH, the effect of α -FeOOH metal loading on 2-CP degradation was almost negligible, which gave no significant effect on the degradation of 2-CP. Therefore, it appears that pH and the reaction temperature are the dominant factors in 2-CP degradation rather than α -FeOOH metal loading.

The logo for UMP (Universiti Malaysia Perlis) is a large, downward-pointing triangle. It is composed of four smaller triangles meeting at the center: a light blue triangle on the top-left, a light green triangle on the top-right, a purple triangle on the bottom-left, and a teal triangle on the bottom-right. The letters 'UMP' are written in white, bold, sans-serif font across the center of the triangle.

UMP

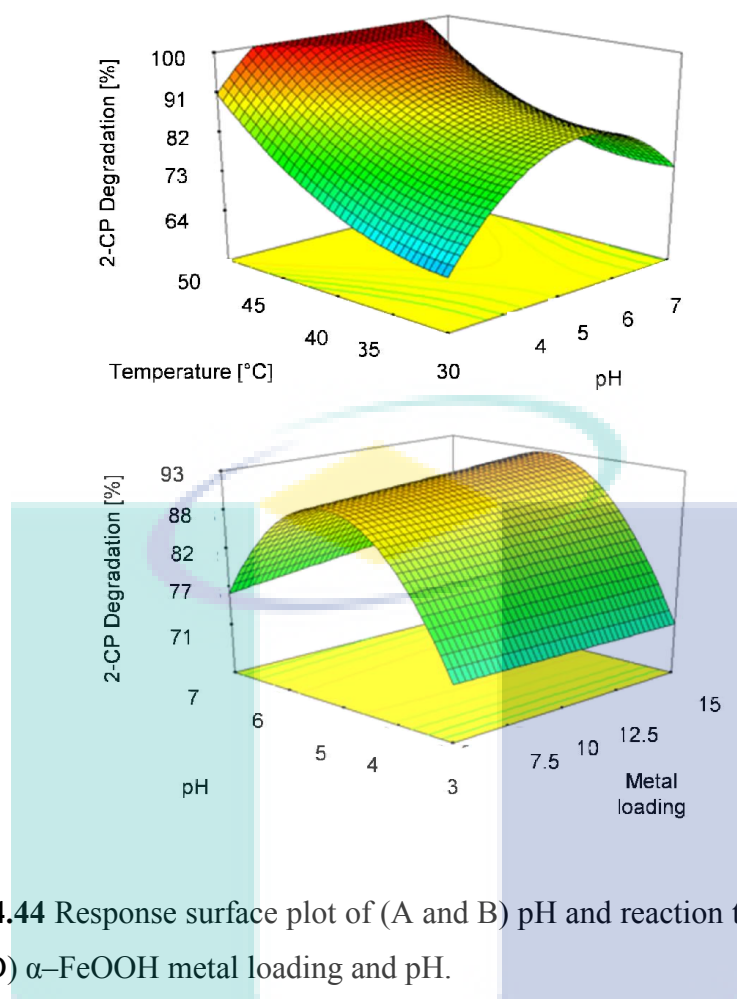


Figure 4.44 Response surface plot of (A and B) pH and reaction temperature; and (C and D) α -FeOOH metal loading and pH.

The regression equations obtained using experimental data can be used to predict 2-CP degradation at any particular α -FeOOH metal loading, pH and reaction temperature within the limits tested. In order to validate the adequacy of the model, four confirmation runs were performed (Table 4.10). Utilizing the point prediction capability of the software enabled the prediction of 2-CP degradation in the selected experiments within a 95% prediction interval. The predicted values and the actual experimental values were compared and the percentage errors were found to be ~ 0.6 – 3.5% . Thus, it can be said that the developed empirical models were reasonably accurate for 2-CP degradation as all actual values for the confirmation runs were within the 95% prediction interval.

Table 4.10 Confirmation experiments.

Operating conditions				2-CP Degradation (%)		
A (wt%)	B	C (mM)	D (°C)	Predicted	Experimental	Error (%)
9.09	5.11	0.14	49.94	99.99	99.39	0.60
12.48	5.09	0.16	34.56	87.19	90.28	3.54
13.07	6.45	0.14	47.36	95.73	97.14	1.47
14.10	5.25	0.11	40	91.59	88.94	2.89

4.5 Kinetic Analysis

The Langmuir–Hinshelwood equation has often been used for modeling of photocatalytic degradation kinetics of many organic compounds. The model also covers the adsorption properties on the photocatalyst surface. The initial degradation rate of 2-CP over α -FeOOH was studied as a function of the initial 2-CP concentration in the range 5 to 70 mg L⁻¹. A plot of $\ln(C_0/C_t)$ versus illumination time signifies a straight line as depicted in Figure 4.45, while the slope of which upon linear regression represent the apparent first order rate constant, k_{app} . Table 4.11 lists the values of k_{app} and the initial reaction rate obtained for the different initial concentrations.

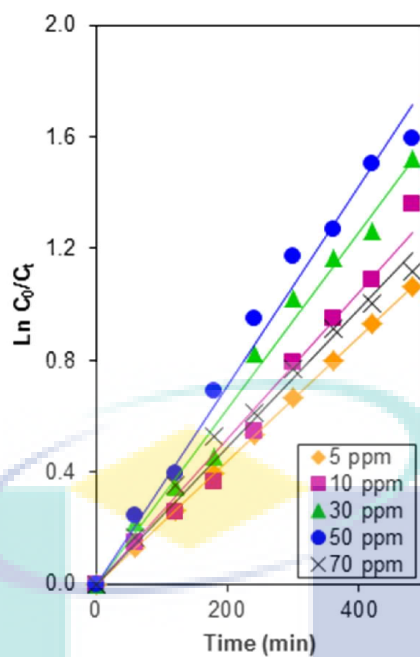


Figure 4.45 Linear transform $\ln C_0/C_t = f(t)$ of 2-CP photodegradation over α -FeOOH.

Table 4.11 Pseudo-first order apparent constant values for 2-CP photodegradation for α -FeOOH.

Initial 2-CP concentration, C_0 (mg L ⁻¹)	Reaction rate, k_{app} (min ⁻¹)	Initial reaction rate, r_0 (mg L ⁻¹ min ⁻¹)
5	0.002	0.01
10	0.003	0.03
30	0.004	0.12
50	0.005	0.25
70	0.003	0.21

The following relationship was obtained when original model is linearized:

$$\frac{1}{r_0} = \left(\frac{1}{k_r K_{LH}} \right) \left(\frac{1}{C_0} \right) + \frac{1}{k_r} \quad (4.21)$$

Based on the tabulated data in Table 4.11, $1/r_0$ was plotted against $1/C_0$. Figure 4.46 shows that $1/r_0$ correlates well to $1/C_0$ proves that the degradation of 2-CP by α -FeOOH nanoparticles fitted with Langmuir–Hinshelwood kinetics model. The values for k_r and K_{LH} obtained from the straight line fitted in Figure 4.46 are 8.7 mg/L min and 2.2×10^{-4} L/mg, respectively. Similar with α -FeOOH, the result obtained shows that $k_r > K_{LH}$ suggesting a surface reaction which indicates that 2-CP absorbed was the controlling step of the process.

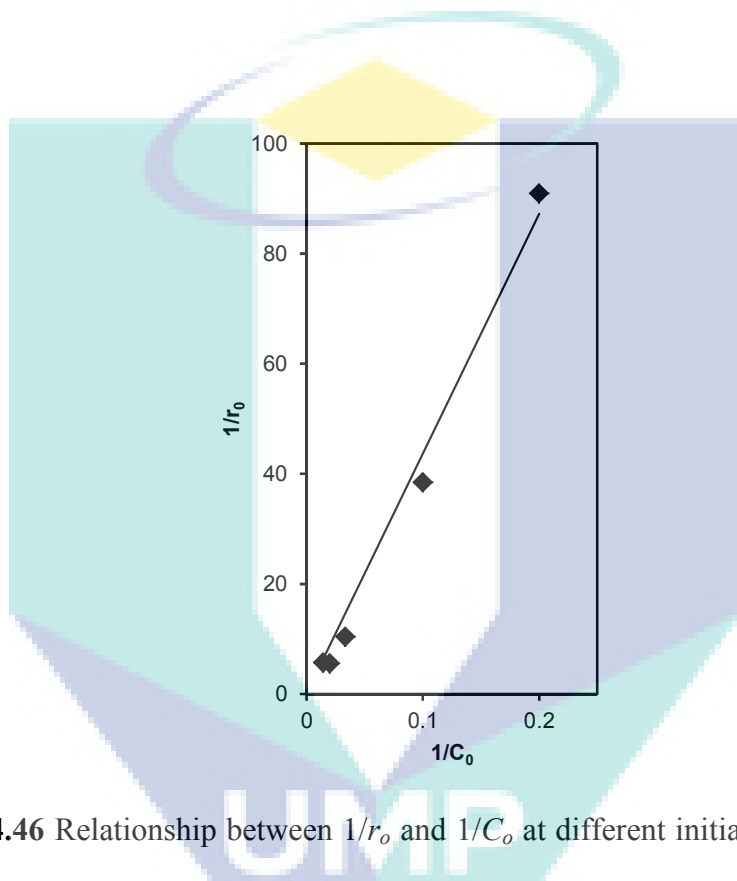


Figure 4.46 Relationship between $1/r_0$ and $1/C_0$ at different initial concentrations of 2-CP.

Then, the kinetic study for the α -FeOOH/MSN was investigated. A plot of $\ln(C_0/C_t)$ versus illumination time signifies a straight line as depicted in Figure 4.47, while the slope of which upon linear regression represent the apparent first order rate constant, k_{app} . Table 4.12 lists the values of k_{app} and the initial reaction rate obtained for the different initial concentrations.

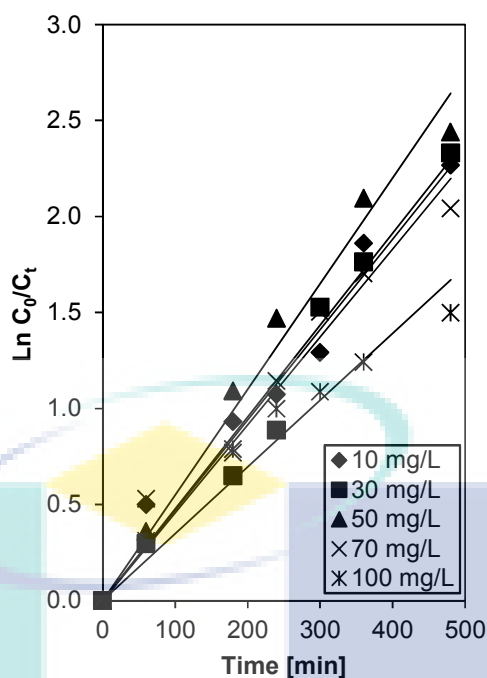


Figure 4.47 Plot of $\ln C_0/C_t$ as a function of time (t).

Table 4.12 Pseudo-first order apparent constant values for 2-CP photodegradation for 10wt% α -FeOOH/MSN.

Initial 2-CP concentration, C_0 (mg L ⁻¹)	Reaction rate, k_{app} (min ⁻¹)	R ²	Initial reaction rate, r_0 (mg L ⁻¹ min ⁻¹)
10	0.0048	0.9729	0.048
30	0.0047	0.9715	0.141
50	0.0055	0.9809	0.275
70	0.0046	0.9628	0.322
100	0.0035	0.9431	0.35

Based on the tabulated data in Table 4.12, $1/r_0$ was plotted against $1/C_0$. Figure 4.48 shows that $1/r_0$ correlates well to $1/C_0$ proves that the degradation of 2-CP by α -FeOOH nanoparticles fitted with Langmuir-Hinshelwood kinetics model. The values for k_r and K_{LH} obtained from the straight line fitted in Figure 4.48 are 5.04 mg/L min and 9.64×10^{-4} L/mg, respectively. The result obtained shows that $k_r > K_{LH}$ suggesting a surface reaction which indicates that 2-CP absorbed was the controlling step of the process. This finding is in similar with

the study reported by Idris *et al.*, (2011b) which using $\gamma\text{-Fe}_2\text{O}_3$ beads for degradation of Cr (VI).

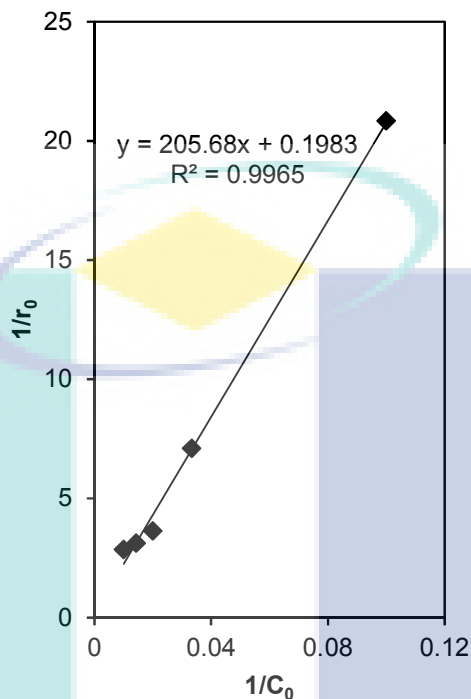


Figure 4.48 Plot of $1/r_0$ as a function of $1/C_0$.

According to the literature (Ilisz *et al.*, 2002), the decay of 2-CP involved several steps before total removal of all organic intermediates was achieved. The proposed degradation of 2-CP in this study was shown in Figure 4.49. Since direct hole oxidation was the main reacting process in this system, direct electron transfer from 2-CP to the catalysts gives a positive radical which can be converted into a chlorodihydroxycyclohexadienyl radical (CIDHCHDR) after nucleophilic water addition, or into chlorophenoxy radical (CPR) after deprotonation.

For CIDHCHDR, $\bullet\text{OH}$ addition in the para position to 2-CP followed by H-abstraction leads to 2-chlorohydroquinone (a), while addition in ortho position followed by Cl-abstraction gives catechol (b). Meanwhile, for CPR, the presence of dissolved O_2 may lead to the formation of chlorobenzoquinone (c). Further

oxidation of the aromatic intermediates (a, b, and c) leads to ring opening and may induce the formation of carboxylic acids, later to the total mineralization of 2-CP to H_2O and CO_2 .

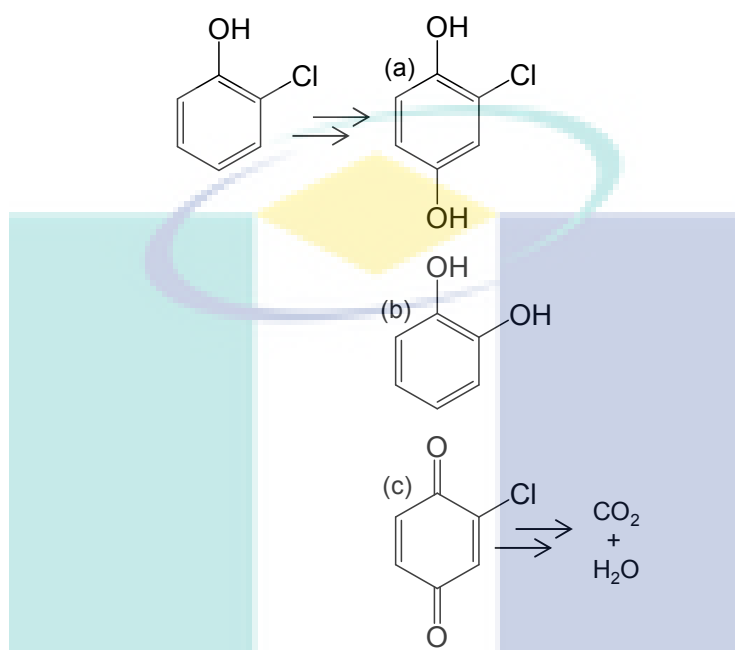


Figure 4.49 Proposed degradation mechanism of 2-CP over the catalysts

4.6 Reusability Study

Reusability is an important issue to be considered when dealing with photocatalyst. Repeated experiments were carried out using $\alpha\text{-FeOOH}$ in order to study the reusability of the catalyst for the degradation of 2-CP (Figure 4.50). It can be observed that after three repeated cycles, the catalyst was still active with just a small decrease in 2-CP degradation percentage from 98% to 88%. However, a relatively significant decrease of degradation was observed after the fourth cycle (85%). The results suggest that the reverse micelle bound on the catalyst most probably gradually detached from the catalyst surface after three

cycles and induced the catalyst aggregation, which therefore reduced the 2-CP degradation efficiency.

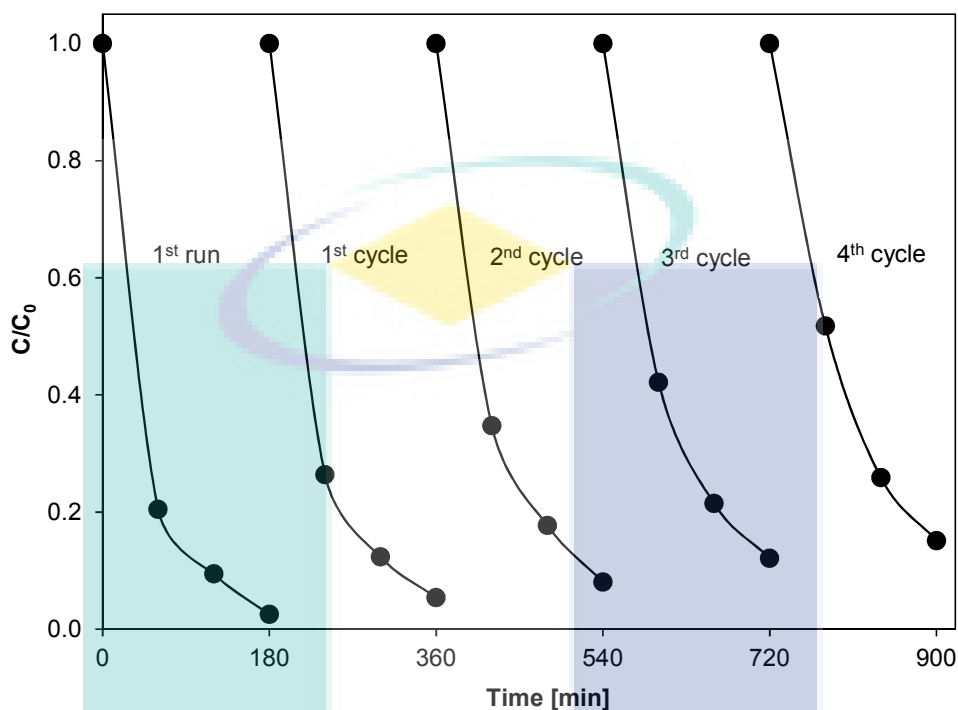


Figure 4.50 Stability of α -FeOOH catalyst after subsequent reactions [pH 5; H_2O_2 concentration 0.156 mM, catalyst dosage 0.30 g L^{-1} ; initial concentration 50 mg L^{-1} , temperature is 323 K].

Meanwhile, repeated experiments were carried out using 10 wt% α -FeOOH/MSN in order to study the stability of the catalyst for the degradation of 2-CP (Figure 4.51). It can be observed that after four repeated cycles, the catalyst was still active with just a small decrease in 2-CP degradation percentage from 92% to 87%.

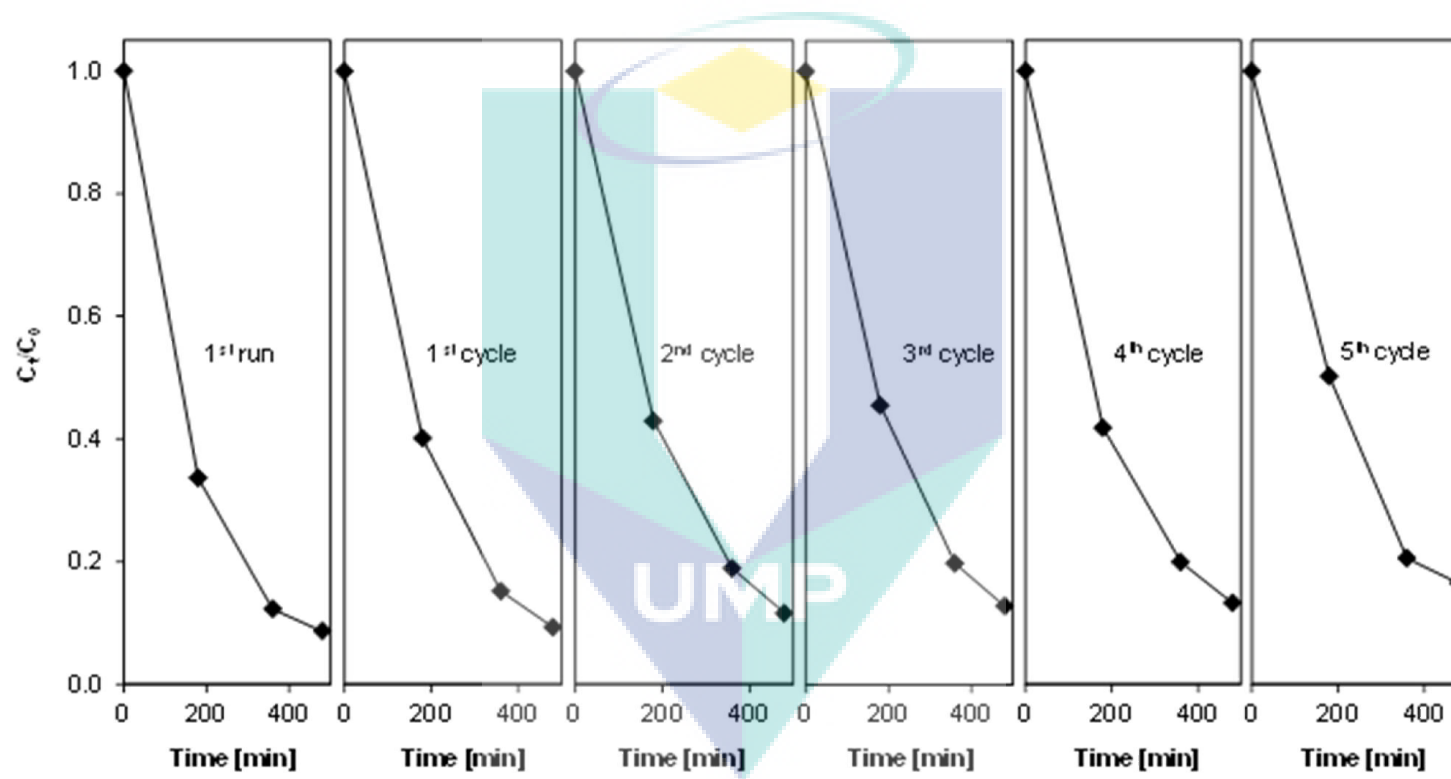


Figure 4.51 Stability of α -FeOOH catalyst after subsequent reactions [pH 5; H_2O_2 concentration 0.156 mM, catalyst dosage 0.30 g L^{-1} ; initial concentration 50 mg L^{-1} , temperature is 323 K].

However, a relatively significant decrease of degradation was observed after the fifth cycle (83%). The results suggest gradual detachment of the colloidal formation on the α -FeOOH after fifth cycles. In addition, the bonding of the adsorbed pollutant onto the support material may hinder the availability of active sites, which therefore reduced the 2-CP degradation efficiency.

The stability test shows that the α -FeOOH/MSN catalyst is stable up to five cycles. Ferroudj and his co-workers has synthesized similar catalyst which is a maghemite iron supported on a silica and was shown to remarkably degrade dyes and nitrophenol (Ferroudj *et al.*, 2013). Meanwhile, a catalyst consists of iron species and MCM-41 as a support material was synthesized by Li and co-workers for desulfurization of dibenzothiophene (Li *et al.*, 2012c). Both Ferroudj *et al.* and Li *et al.* reported high stability upon catalyst reusability up to 5 and 4 cycles, respectively, which is comparable with the reusability result of the catalyst in this study.

4.7 Scaling Up System

In this study, two models has been developed from the response surface methodology analysis including the model for α -FeOOH catalyst (Eq. 4.19) and α -FeOOH/MSN (Eq. 4.20). Both model were employed to study the feasibility of these models with the respective photocatalysts which generated using the laboratory system to be used in the pilot scale system. The optimum conditions were inserted with these model with the enhancement to the pilot scale system with 10-fold.

The results were then compared with the 2-CP degradation by using the laboratory scale (Figure 4.52). The results showed that the scale-up system employing the generated model is to degrade 2-CP as comparable as the laboratory scale system. The errors were compared as shown in Table 4.13. The system

employing α -FeOOH in large scale shows ~12% of error as compared to the laboratory system. However, supported α -FeOOH on the MSN showed remarkable performance even in the pilot scale system, with the error of ~6%, indicating the feasibility of the supported colloidal metal catalyst and the system model to be used in the scaled-up system. The remarkable performance in the 10-fold scale-up system may provide insight to the viability of this system in larger scale, which appropriate with the aim to develop a laboratory system that compatible be used in the industrial system.

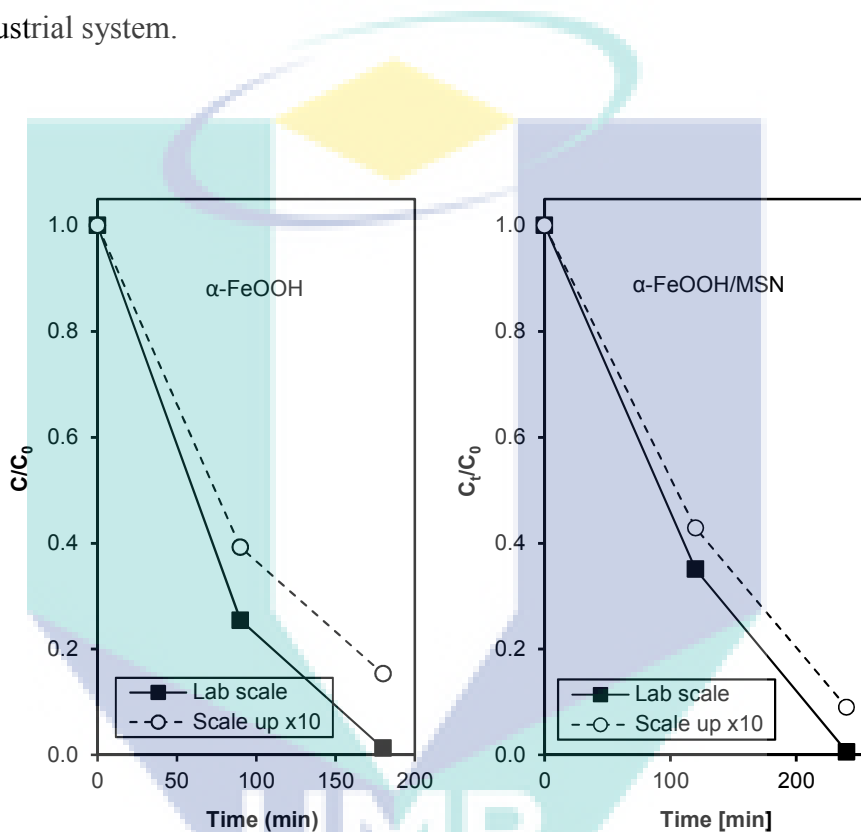


Figure 4.52 Scale-up performance of the catalysts in 10-fold pilot scale system

Table 4.13 Comparison of the catalysts performances in the scale-up system

Catalysts	2-CP degradation (%)		
	Lab scale	Scale-up ($\times 10$)	Error
α -FeOOH/MSN	99.39	91.00	6.23%
α -FeOOH	98.71	84.65	12.45%

4.8 Application to Various Pollutants

In order to study the proficiency of the α -FeOOH and α -FeOOH/MSN catalysts towards various applications, different target pollutants were selected to observe the performance of the catalysts. The target pollutants are including anionic dye (methyl orange), cationic dye (Congo red), and a simple phenolic compound (phenol). The degradation of these pollutants was tested under similar conditions of 2-CP degradation and results are shown in Figure 4.53. A high degradation percentage (>85%) of various types of dye was obtained, with the photodegradation percentage of 90%, 99%, and 85% of methyl orange, Congo red, and phenol, respectively for α -FeOOH. Meanwhile, the performance tested using α -FeOOH/MSN shows remarkable result of 99%, 99%, and 88% of methyl orange, Congo red, and phenol, respectively.

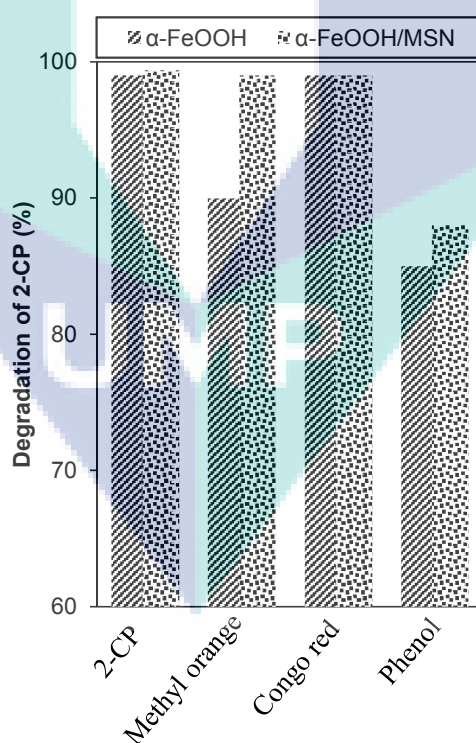
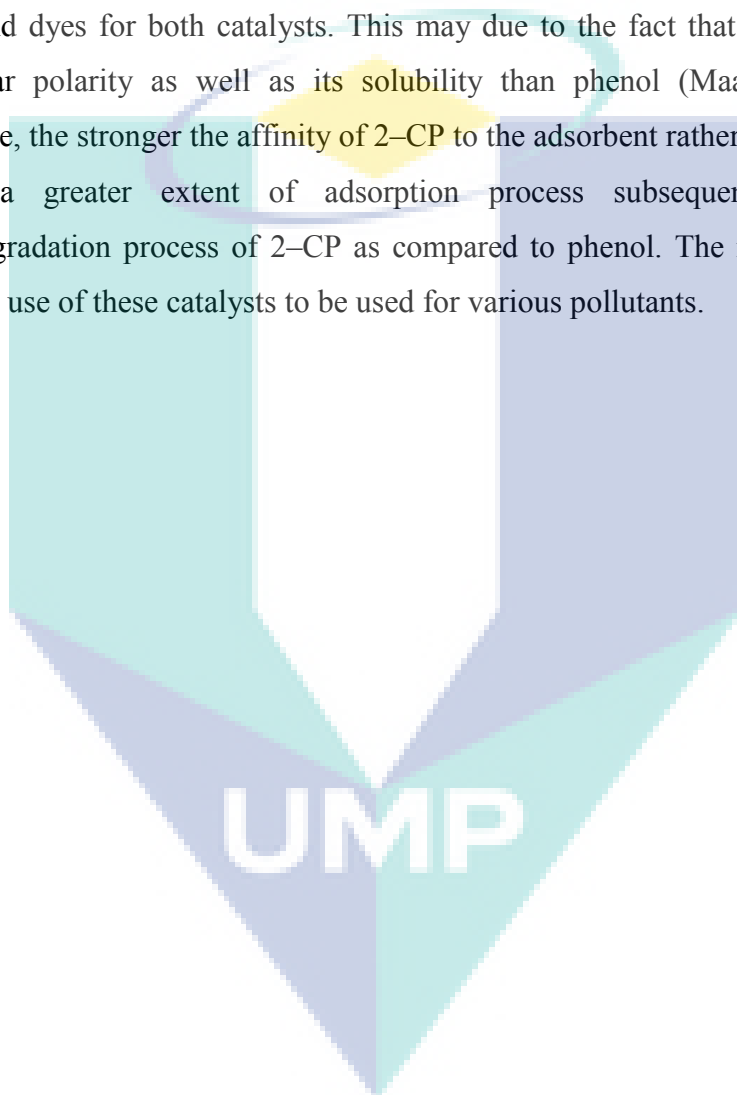


Figure 4.53 Performance of catalysts for various pollutants (pH 5, H_2O_2 molar concentration is 0.156 mM; catalyst dosage 0.4 g L^{-1} ; initial concentration is 50 mg L^{-1} ; temperature 30°C).

It can be observed that α -FeOOH gives lower degradation of methyl orange as compared to α -FeOOH/MSN. This may be due to the possible agglomeration of α -FeOOH that hinders light accessibility towards the catalyst, thus decreasing its catalytic activity. The degradation of Congo red is comparable for both catalysts (both are 99%), indicating good photodegradation activity of the catalysts towards cationic dye. This may be due to the possible entrapment of cationic dye towards the colloidal structure of the catalysts. Meanwhile, the degradation of phenol is lower than those of 2-CP and dyes for both catalysts. This may be due to the fact that 2-CP has a lower molecular polarity as well as its solubility than phenol (Maarof *et al.*, 2004). Therefore, the stronger affinity of 2-CP to the adsorbent rather than water/solvent results in a greater extent of adsorption process subsequently followed by photodegradation process of 2-CP as compared to phenol. The result indicates the potential use of these catalysts to be used for various pollutants.



CHAPTER 5

CONCLUSION AND RECOMMENDATIONS

5.1 Result Summary

In this section, it covers the result summary of the study such as the synthesis and characterization and the photodegradation performance evaluation.

5.1.1 Synthesis and Characterization

The results reveal the feasibility to synthesize well-dispersed α -FeOOH nanoparticles in a diameter range of 5–10 nm via a facile electrosynthesis in cationic surfactant. Cationic surfactant was successfully demonstrated to play a dual role as electrolyte and solvent. Reverse micelle formation bound on the α -FeOOH surface in which the cationic surfactant retained around α -FeOOH surface with a free swinging alkane tail pointing outward from the catalyst was found to stabilize and miniaturize the nanoparticles.

Meanwhile, the characterization results also verified the retention of the α -FeOOH colloidal structure even after being loaded onto MSN. The loading of α -FeOOH onto MSN significantly induced the silica removal followed by isomorphous substitution of free Fe species. It was also observed that the colloidal α -FeOOH was distributed on different locations on the MSN, depending on the pore size of the MSN. Therefore, it can be concluded that the synthesis method is capable in altering and re-structuring the catalysts.

5.1.2 Catalytic Performance Evaluation

The colloidal α -FeOOH were verified to positively serve as a photo-Fenton-like catalyst for complete degradation of 2-CP under mild operating conditions, which induced the inhibition of the photo-induced electron-hole pairs recombination where the photogenerated electron could be trapped by the reverse micelle bound on the catalyst surface. Nearly neutral conditions of pH 5 were able to completely degrade 2-CP within 180 min with a small amount of H_2O_2 (0.156 mM).

Meanwhile, the performance of α -FeOOH/MSN indicates the degradation of 2-CP with removal percentage of 92.2, 79.3, 73.1, and 14.2%, with the loading of α -FeOOH in the following order: 10 wt% > 15 wt% > 5 wt% > MSN, respectively. It was found that the retention of colloidal metal over MSN support could trap the photogenerated electron. In the meantime, the substituted Fe species (Si-O-Fe) may inhibit the electron-hole recombination by transferring the photoinduced electron to the MSN support. The synergic effect between the dual types Fe species with the MSN was able to occur in regards to the support material that acts as a stable electron acceptor.

Response surface methodology (RSM) analysis for α -FeOOH and α -FeOOH/MSN showed good significance of model with low probability values (<0.0001) and a high coefficient of determination (R^2). Meanwhile, the kinetic studies of both catalysts illustrated that a surface reaction was the controlling step of the process. Reusability study showed that α -FeOOH are still stable after 4 subsequent reactions while α -FeOOH/MSN maintained its robustness up to 5 subsequent cycles. The model generated for both catalysts were employed in the upscale system. The upscaling study using 10-fold upscale system employing both catalysts indicate superior performance of the catalysts with almost complete degradation of 2-CP. In addition, the employment of the catalysts on degradation of anionic dye, cationic dye, and phenol had also showed remarkable performance of the catalytic system.

5.2 Future Study

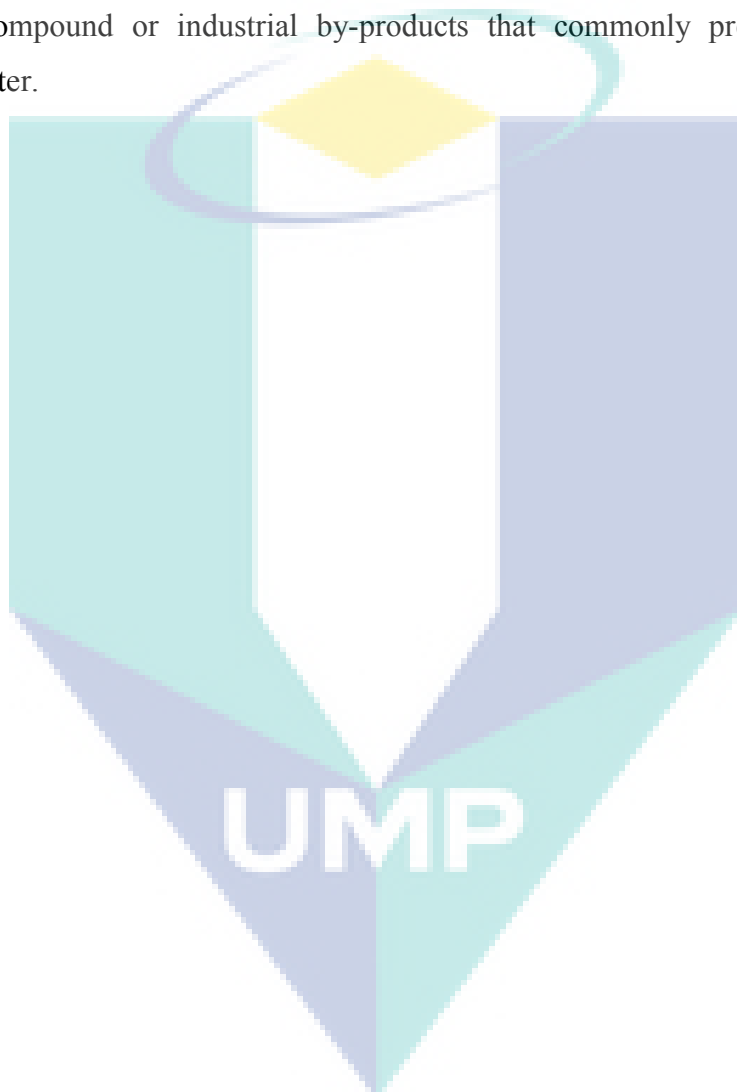
This section covers the recommendation for future study in term of synthesis and characterization, and also photodegradation process.

5.2.1 Synthesis and Characterization

The simple process of preparing the catalyst and the low amount of metal loading required make this system exhibits great potential for improving the quality of wastewater discharged from the target industries. It is believed to be extendable to the synthesis of other metal oxide such as Zn, Zr, and Cu or other support material such as SBA-15 and zeolites which have different characteristics and structural properties.

5.2.2 Photodegradation of Organic Pollutants

In the current study, synthesis of nanoparticles and the retainment of cationic surfactant by electrolysis method were demonstrated to improve the photodegradation of 2-chlorophenol. For the extending of this work, the system should be applied for degradation of other organic compounds such as herbicides-based compound or industrial by-products that commonly present in industrial wastewater.



REFERENCES

- Abbott, A. P. and McKenzie, K. J. (2006). Application of Ionic Liquids to the Electrodeposition of Metals. *Physical Chemistry Chemical Physics*. 8: 4265–4279.
- Akpan, U. G., and Hameed, B. H. (2009). Parameters Affecting the Photocatalytic Degradation of Dyes using TiO₂-based Photocatalysts: A Review. *Journal of Hazardous Materials*. 170(2–3): 520–529.
- Aishah, A. J., Kurono, N., and Tokuda, M. (2002). Facile Synthesis of Ethyl 2-Arylpropenoates by Cross-Coupling Reaction using Electrogenerated Highly Reactive Zinc. *Tetrahedron*. 58(37): 7477–7484.
- Al Duri, B. (1995). *Reviews in Chemical Engineering*. 11(2): 101.
- Annachhatre, A. P., and Gheewala, S. H. (1996). Biodegradation of Chlorinated Phenolic Compounds. *Biotechnology Advances*. 14(1): 35–56.
- Annadurai, G., Juang, R. S., and Lee, D. J. (2002). Factorial Design Analysis of Adsorption of Activated Carbon on Activated Carbon Incorporated with Calcium Alginate. *Advanced Inorganic Environmental Research*. 6: 191–199.
- Anpo, M. (1989). Photocatalysis on Small Particle TiO₂ Catalysts. Reaction Intermediates and Reaction Mechanisms. *Research on Chemical Intermediates*. 11(1): 67–106.
- Aziz, M. A. A., Jalil, A. A., Triwahyono, S., Mukti, R. R., Taufiq-Yap, Y. H., and Sazegar, M. R. (2014). Highly Active Ni-Promoted Mesoporous Silica Nanoparticles for CO₂ Methanation. *Applied Catalysis B: Environmental*. 147: 359–368.
- Bandara, J., Mielczarski, A., Lopez, A. and Kiwi, J. (2001a). 2. Sensitized Degradation of Chlorophenols on Iron Oxides Induced by Visible Light:

- Comparison with Titanium Oxide. *Applied Catalysis B: Environmental*, 34(4): 321–333.
- Bandara, J., Klehm, U., and Kiwi, J. (2007b). Raschig Rings–Fe₂O₃ Composite Photocatalyst Activate in the Degradation of 4–Chlorophenol and Orange II Under Daylight Irradiation. *Applied Catalysis B: Environmental*. 76(1–2): 73–81.
- Bayarri, B., Giménez, J., Maldonado, M. I., Malato, S., and Esplugas, S. (2013). 2,4-Dichlorophenol Degradation by Means of Heterogeneous Photocatalysis. Comparison Between Laboratory and Pilot Plant Performance. *Chemical Engineering Journal*. 232: 405–417.
- Bertelli, M. and Selli, E. (2006). Reaction Paths and Efficiency of Photocatalysis on TiO₂ and of H₂O₂ Photolysis in the Degradation of 2–Chlorophenol. *Journal of Hazardous Material*. 138(1): 46–52.
- Bishop, J. L. and Murad, E. (2004). Characterization of Minerals and Biogeochemical Markers on Mars: A Raman and IR Spectroscopic Study of Montmorillonite. *Journal of Raman Spectroscopy*. 35: 480–486.
- Bourlinos, A. B., Karakassides, M. A., and Petridis, D. (2000). Synthesis and Characterization of Iron–Containing MCM–41 Porous Silica by the Exchange Method of the Template. *Journal of Physical Chemistry B*. 104: 4375–4380.
- Burbano, D. D., Suidam, M., Richardson, T. (2003). Chemical Destruction of MTBE using Fenton's reagent: Effect of Ferrous Iron/Hydrogen Peroxide Ratio. *Water Science and Technology*. 47: 165–171.
- Carey, F. A. (2000). *Organic Chemistry*, 4th Edition, McGraw–Hill, USA.
- Chang, M. C. and Tanaka, J. (2002). FT–IR Study for Hydroxyapatite/Collagen Nanocomposite Cross–Linked by Glutaraldehyde. *Biomaterials*. 23: 4811–4818.
- Chen, H. F., Wei, G. D., Han, X., Li, S., Wang, P. P., Chubik, M., Gromov, A., Wang, Z. P., and Han, W. (2011). Large-Scale Synthesis of Hierarchical Alpha-FeOOH Flowers by Ultrasonic-Assisted Hydrothermal Route. *Journal of Materials Science: Materials in Electronics*. 22: 252–259.
- Cheng, W., Dong, S., and Wang, E. (2003a). Synthesis and Self–Assembly of Cetyltrimethylammonium Bromide–Capped Gold Nanoparticles. *Langmuir*. 19(22): 9434–9439.

- Cheng, Y., Sun, H., Jin, W., and Xu, N. (2007b). Photocatalytic Degradation of 4-Chlorophenol with Combustion Synthesized TiO_2 under Visible Light Irradiation. *Chemical Engineering Journal*. 128(2–3): 127–133.
- Chia, N–C. and Mendelsohn, R. (1996). Conformational Disorder in Unsaturated Phospholipids by FTIR Spectroscopy. *BBA–Biomembranes*. 1283: 141–150.
- Cho, I.–H., and Zoh, K.–D. (2007). Photocatalytic Degradation of Azo Dye (Reactive Red 120) in TiO_2 /UV System: Optimization and Modeling using a Response Surface Methodology (RSM) Based on the Central Composite Design. *Dyes and Pigments*. 75(3): 533–543.
- Christensen, A. N., Jensen, T. R., Bahl, C. R. H., and DiMasi, E. (2007). Nano Size Crystals of Goethite, $\alpha\text{-FeOOH}$: Synthesis and Thermal Transformation. *Journal of Solid State Chemistry*. 180(4): 1431–1435.
- Cong, H., Toftegaard, R., Arnbjerg, J., and Ogilby, P. R. (2010). Silica–Coated Gold Nanorods with a Gold Overcoat: Controlling Optical Properties by Controlling the Dimensions of a Gold–Silica–Gold Layered Nanoparticle, *Langmuir*. 26: 4188–4195.
- Cornell, R.M. and Schwertmann, U. (2003). *The Iron Oxides: Structure, Properties, Reactions, Occurrences and Uses*. 2nd Edition: Wiley–VCH.
- Dai, C., Zhang, A., Li, L., Hou, K., Ding, F., Li, J., Mu, D., Song, C., Liu, M., and Guo, X. (2013). Synthesis of Hollow Nanocubes and Macroporous Monoliths of Silicalite–1 by Alkaline Treatment. *Chemistry of Materials*. 25: 4197–4205.
- Daneshvar, N., Rabbani, M., Modirshahla, N., and Behnajady, M. A. (2004). Kinetic modeling of Photocatalytic Degradation of Acid Red 27 in UV/ TiO_2 Process. *Journal of Photochemistry and Photobiology A: Chemistry*. 168(1–2): 39–45.
- Das, S., and Hendry, M. J. (2011). Changes of Crystal Morphology of Aged Goethite Over a Range of pH (2–13) at 100°C. *Applied Clay Science*. 51(1–2): 192–197
- Deng, Y., Cai, Y., Sun, Z., and Zhao, D. (2011). Magnetically responsive Ordered Mesoporous Materials: A Burgeoning Family of Functional Composite Nanomaterials. *Chemical Physics Letters*. 510(1–3): 1–13.
- Dorfman, L., M., and Adams, G., E. (1973). Reactivity of the Hydroxyl Radical in Aqueous Solutions. *National Standard Reference Data System, National Bureau of Standards*. 46: 1.

- Durand, A.-P. Y., and Brown, R. G. (1995). Photoreactions of 4-Chlorophenol in Aerated and Deaerated Aqueous Solution: Use of LC-MS for Photoproduct Identification. *Chemosphere*. 31(7): 3595-3604.
- Eisenhauer, H. R. (1964). Oxidation of phenolic wastes. *Journal of Water Pollution Control*. 36: 1117-1127.
- Elghniji, K., Hentati, O., Mlaik, N., Mahfoudh, A., and Ksibi, M. (2012). Photocatalytic Degradation of 4-Chlorophenol under P-Modified TiO₂/UV System: Kinetics, Intermediates, Phytotoxicity and Acute Toxicity. *Journal of Environmental Sciences*. 24(3): 479-487
- Endud, S. and Wong, K-L. (2007). Mesoporous Silica MCM-48 Molecular Sieve Modified with SnCl₂ in Alkaline Medium for Selective Oxidation of Alcohol. *Microporous and Mesoporous Material*. 101: 256-263.
- Feng, J., Hu, X., and Yue, P. L. (2003). Novel Bentonite Clay-Based Fe-Nanocomposite as a Heterogeneous Catalyst for Photo-Fenton Discoloration and Mineralization of Orange II. *Environmental Science & Technology*. 38(1): 269-275.
- Ferroudj, N., Nzimoto, J., Davidson, A., Talbot D., Briot, E., Dupuis, V., Bée, A., Medjram, M.S., Abramson, S. (2013). Maghemite Nanoparticles and Maghemite/Silica Nanocomposite Microspheres as magnetic Fenton Catalysts for the Removal of Water Pollutants. *Applied Catalysis B: Environmental*. 136: 9-18.
- Gao, J. and Teplyakov, A. V. (2014b). Thermal Transformations of 2-Chlorophenol on a Surface of ZnO Powder Catalyst. *Catalysis Today*. 238: 111-117.
- Gao, Y., and Hao, J. (2009a). Electrochemical Synthesis of Zinc Nanoparticles via a Metal-Ligand-Coordinated Vesicle Phase. *The Journal of Physical Chemistry B*. 113(28): 9461-9471.
- Garrido-Ramírez, E. G., Theng, B. K. G., and Mora, M. L. (2010). Clays and Oxide Minerals as Catalysts and Nanocatalysts in Fenton-like Reactions — A Review. *Applied Clay Science*. 47(3-4): 182-192.
- Gaya, U. I., Abdullah, A. H., Zainal, Z., and Hussein, M. Z. (2009). Photocatalytic Treatment of 4-Chlorophenol in Aqueous ZnO Suspensions: Intermediates, Influence of Dosage and Inorganic Anions. *Journal of Hazardous Materials*. 168(1): 57-63

- Gordon, T.R. and Marsh, A.L. (2009). Temperature Dependence of the Oxidation of 2-Chlorophenol by Hydrogen Peroxide in the Presence of Goethite. *Catalysis Letter*. 132: 349–354
- Goswami, D., Sen, R., Basu, J. K., and De, S. (2010). Surfactant Enhanced Ricinoleic Acid Production using *Candida Rugosa* Lipase. *Bioresource Technology*. 101(1): 6–13
- Groen, J. C., Peffer, L. A. A, Moulijn, J. A, and Pérez-Ramírez, J. (2004a). Mesoporosity Development in ZSM-5 Zeolite upon Optimized Desilication Conditions in Alkaline Medium. *Colloids and Surfaces A: Physicochemical and Engineering*. 241: 53–58.
- Groen, J. C., Hamminga, G. M., Moulijn, J. A, and Pérez-Ramírez, J. (2007b). In Situ Monitoring of Desilication of MFI-type Zeolites in Alkaline Medium. *Chemistry Chemical Physics*. 9: 4822–4830.
- Guettaï, N., and Ait Amar, H. (2005). Photocatalytic Oxidation of Methyl Orange in Presence of Titanium Dioxide in Aqueous Suspension. Part I: Parametric Study. *Desalination*. 185(1–3): 427–437.
- Guo, Y., Quan, X., Lu, N., Zhao, H., and Chen, S. (2007a). High Photocatalytic Capability of Self-Assembled Nanoporous WO₃ with Preferential Orientation of (002) Planes. *Environmental Science & Technology*. 41(12): 4422–4427.
- Guo, P., Wang, X., & Guo, H. (2009b). TiO₂/Na-HZSM-5 Nano-Composite Photocatalyst: Reversible Adsorption by Acid Sites Promotes Photocatalytic Decomposition of Methyl Orange. *Applied Catalysis B: Environmental*. 90(3–4): 677–687.
- Guo, J-F., Ma, B., Yin, A., Fan, K., and Dai, W-L. (2012c). Highly Stable and Efficient Ag/AgCl@TiO₂ Photocatalyst: Preparation, Characterization, and Application in the Treatment of Aqueous Hazardous Pollutants. *Journal of Hazardous Materials*. 77: 211–212.
- Gupta, V. K., Srivastava, S. K., and Tyagi, R. (2000a). Design Parameters for the Treatment of Phenolic Waste by Carbon Columns (Obtained from Fertilizerwaste Material), *Water Research*. 34: 1543–1550.
- Gupta, C. K. (2003b). *Chemical Metallurgy Principles and Practice*. Weinheim, Germany, Wiley-VCH.

- Hariharan, C. (2006). Photocatalytic Degradation of Organic Contaminants in Water by ZnO Nanoparticles: Revisited. *Applied Catalysis A: General*. 304: 55–56.
- Hashimoto, K., and Cohen, M. (1974). Anodic Deposition of Ferric Oxy–Hydroxide Films on Platinum from Perchlorate Solutions. *Journal of The Electrochemical Society*. 121(1): 37–42.
- Hassan, H., and Hameed, B. H. (2011). Fenton–like Oxidation of Acid Red 1 Solutions Using Heterogeneous Catalyst Based on Ball Clay. *International Journal of Environmental Science and Development*. 2: 218–222.
- He, Z., Wang, C., Wang, H., Hong, F., Xu, X., Chen, J., and Song, S. (2011). Increasing the Catalytic Activities of Iodine Doped Titanium Dioxide by Modifying with Tin Dioxide for the Photodegradation of 2–Chlorophenol under Visible Light Irradiation, *Journal of Hazardous Materials*. 189(1–2): 595–602.
- Holladay, D. W., Hanchen, C. W., Scott, C. D., and Chilcote, D. D. (1978). Biodegradation of Phenolic Waste Liquors in Stirred–Tank, Packed–Bed and Fluidized–Bed Bioreactors. *Journal WPCF*. 50: 2573–2589.
- Howard, P. H., Boethling, R.S., Jarvis, W.F., Meylan, W.M., and Michaelenko, E.M. (1991). *Handbook of Environmental Degradation Rates*. Lewis Publishers, Chelsea, MI.
- Hu, P., Pan, D., Zhang, S., Tian, J., and Volinsky, A. A. (2011a). Heat Treatment Effects on Fe₃O₄ Nanoparticles Structure and Magnetic Properties Prepared by Carbothermal Reduction. *Journal of Alloys and Compounds*. 509(5): 3991–3994.
- Hu, S., Liu, G., Zhu, D., and Chen, C. (2012b). Synthesis, Characterization, and Evaluation of Boron–Doped Iron Oxides for the Photocatalytic Degradation of Atrazine under Visible Light. *International Journal of Photoenergy*. 598713.
- Huh, S., Wiench, J. W., Yoo J–C., Pruski, M., and Lin, V.S.–Y. (2003). Organic Functionalization and Morphology Control of Mesoporous Silicas via a Co–Condensation Synthesis Method. *Chemistry of Materials*. 5(22): 4247–4256.
- Idris, A., Kormin, F., and Noordin, M. Y. (2006). Application of Response Surface Methodology in Describing the Performance of Thin Film Composite Membrane. *Separation and Purification Technology*. 49: 271–280.

- Idris, A., Hassan, N., Rashid, R., and Ngomsik, A.–F. (2011b). Kinetic and Regeneration Studies of Photocatalytic Magnetic Separable Beads for Chromium (VI) Reduction Under Sunlight. *Journal of Hazardous Materials*. 186(1): 629–635.
- Ilisz, I., Dombi, A., Mogyorósi, K., Farkas, A., and Dékány, I. (2002). Removal of 2-Chlorophenol from Water by Adsorption Combined With TiO₂ Photocatalysis. *Applied Catalysis B: Environmental*. 3: 247–256.
- Imoberdorf, G. E., Cassano, A. E., Irazoqui, H. A., and Alfano, O. M. (2007). Optimal Design and Modeling of Annular Photocatalytic Wall Reactors. *Catalysis Today*. 129(1–2): 118–126.
- Jaafar, N. F., Abdul Jalil, A., Triwahyono, S., Muhd Muhid, M. N., Sapawe, N., Satar, M. A. H., and Asaari, H. (2012). Photodecolorization of Methyl Orange over α -Fe₂O₃-Supported HY Catalysts: The Effects of Catalyst Preparation and Dealumination. *Chemical Engineering Journal*. 191:112–122.
- Jal, P. K., Patel, S., and Mishra, B. K. (2004). Chemical Modification of Silica Surface by Immobilization of Functional Groups for Extractive Concentration of Metal Ions. *Talanta*. 62: 1005–1028.
- Jalil, A. A., Kurono, N., and Tokuda, M. (2001). Facile Synthesis of 2-Arylpropenoic Acid Esters by Cross-Coupling using electrogenerated Highly Reactive Zinc and a Palladium Catalyst. *Synlett*. 12: 1944–1946.
- Jia, C.–J. and Schüth, F. (2011). Colloidal Metal Nanoparticles as a Component of Designed Catalyst. *Physical Chemistry Chemical Physics*. 13: 2457–2487.
- Jiao, S., Xu, L., Hu, K., Li, J., Gao, S., and Xu, D. (2009). Morphological Control of α -FeOOH Nanostructures by Electrodeposition. *The Journal of Physical Chemistry C*. 114(1): 269–273.
- Jusoh, N. W. C., Jalil, A. A., Triwahyono, S., Setiabudi, H. D., Sapawe, N., Satar, M. A. H., Karim, A. H., Kamarudin, N. H. N., Jusoh, R., Jaafar, N. F., Salamun, N., and Efendi, J. (2013). Sequential Desilication–Isomorphous Substitution Route to Prepare Mesostructured Silica Nanoparticles Loaded with ZnO and Their Photocatalytic Activity. *Applied Catalysis A: General*. 468: 276–287.
- Joshi, S., Yadav, S. and Desai, A. J., (2008). Application of Response–Surface Methodology to Evaluate the Optimum Medium Components for the

- Enhanced Production of Lichenysin by *Bacillus Licheniformis* R2. *Biochemical Engineering Journal*. 41(2): 122–127
- Kalota, D. J., and Silverman, D. C. (1994). Behavior of Aspartic Acid as a Corrosion Inhibitor for Steel. *Corrosion*. 50: 138–145.
- Kamarudin, N. H. N., Jalil, A. A., Triwahyono, S., Artika, V., Salleh, N. F. M., Karim, A. H., Jaafar, N. F., Sazegar, M. R., Mukti, R. R., Hameed, B. H., and Johari, A. (2014). Variation of the Crystal Growth of Mesoporous Silica Nanoparticles and the Evaluation to Ibuprofen Loading and Release. *Journal of Colloid and Interface Science*. 421: 6–13.
- Kang, N., Lee, D. S., and Yoon, J. (2002). Kinetic Modeling of Fenton Oxidation of Phenol and Monochlorophenols. *Chemosphere*. 47(9): 915–924.
- Karge, H. G. (1998). Characterization by infrared spectroscopy, *Microporous and Mesoporous Material*. 22: 547–549.
- Karim, A. H., Jalil, A. A., Triwahyono, S., Sidik, S. M., Kamarudin, N. H. N., Jusoh, R., Jusoh, N. W. C., and Hameed, B. H. (2012). Amino Modified Mesostructured Silica Nanoparticles for Efficient Adsorption of Methylene Blue. *Journal of Colloid and Interface Science*. 386: 307–314.
- Kasiri, M. B., Aleboyeh, H., and Aleboyeh, A. (2008). Degradation of Acid Blue 74 using Fe–ZSM5 Zeolite as a Heterogeneous Photo–Fenton Catalyst. *Applied Catalysis B: Environmental*. 84(1–2): 9–15.
- Kaur, R. and Mehta, S. K. (2014). Self Aggregating Metal Surfactant Complexes: Precursors for Nanostructures. *Coordination Chemistry Reviews*. 62: 37–54.
- Kerker, M. (2012). *Colloid and Interface Science V3: Adsorption, Catalysis, Solid Surfaces, Wetting, Surface Tension, and Water*. Academic Press. London.
- Khalil, L. B., Mourad, W. E., and Rophael, M. W. (1998). Photocatalytic Reduction of Environmental Pollutant Cr(VI) over Some Semiconductors Under UV/Visible Light Illumination. *Applied Catalysis B: Environmental*. 17(3): 267–273.
- Khan, M. Z., Mondal, P. K., and Sabir, S. (2011). Bioremediation of 2–Chlorophenol Containing Wastewater by Aerobic Granules–Kinetics and Toxicity. *Journal of Hazardous Materials*. 190(1–3): 222–228.
- Kim, J. R. and Kan, E. (2015). Heterogeneous Photo–Fenton Oxidation of Methylene Blue using CdS–Carbon Nanotube/TiO₂ Under Visible Light. *Journal of Industrial and Engineering Chemistry*. 21: 644–652.

- Kingsley, J. J. and Patil, K. C. (1988). A Novel Combustion Process for the Synthesis of Fine Particle α -Alumina and Related Oxide Materials. *Material Letters*. 6: 427.
- Kitis, M., Kaplan, S. S., Karakaya, E., Yigit, N. O., and Civelekoglu, G. (2007). Adsorption of Natural Organic Matter from Waters by Iron Coated Pumice. *Chemosphere*. 66(1): 130–138.
- Krehula, S., Popović, S., and Musić, S. (2002). Synthesis of Acicular α -FeOOH Particles at a Very High pH. *Materials Letters*. 54(2): 108–113.
- Kwon, B. G., Lee, D. S., Kang, N., and Yoon, J. (1999). Characteristics of *p*-Chlorophenol Oxidation by Fenton's Reagent. *Water Research*. 33(9): 2110–2118.
- Lang, N., Delichere, P., and Tuel, A. (2002). Post-Synthesis Introduction of Transition Metals in Surfactant-Containing MCM-41. *Microporous and Mesoporous Materials*. 56: 203–217.
- Laoufi N. A., Tassalit, D. and Bentahar, F. (2008). The Degradation of Phenol in Water Solution by. TiO_2 Photocatalysis in a Helical Reactor, *Global NEST Journal*.
- Lee, I., Morales, R., Albiter, M. A., and Zaera, F. (2008). Synthesis of Heterogeneous Catalysts with Well Shaped Platinum Particles to Control Reaction Selectivity. *Proceedings of the National Academy of Sciences USA*. 105: 15241–15246.
- Leibenguth, J. L. and Cohen, M. (1972). The Anodic Deposition of Oxide Films on Platinum from Ferrous Sulfate Solutions. *Journal of the Electrochemistry Society*. 119(8): 987–991
- Li, N., N. (1968a). Separating Hydrocarbons with Liquid Membrane. *US Patent 3 (410)*, 794.
- Li, J.-M., Meng, X.-G., Hu, C.-W., and Du, J. (2009b). Adsorption of Phenol, *p*-Chlorophenol and *p*-Nitrophenol onto Functional Chitosan. *Bioresource Technology*. 100(3): 1168–1173.
- Li, B., Wu, K., Yuan, T., Han, C., Xu, J., and Pang, X. (2012c). Synthesis, Characterization and Catalytic Performance of High Iron Content Mesoporous Fe-MCM-41. *Microporous and Mesoporous Material*. 151: 277–281.

- Liou, M.-J., and Lu, M.-C. (2008). Catalytic Degradation of Explosives with Goethite and Hydrogen Peroxide. *Journal of Hazardous Materials*. 151(2–3): 540–546.
- Litter, M., I. (1999). Heterogeneous Photocatalysis: Transition Metal Ions in Photocatalytic Systems. *Applied Catalysis B: Environmental*. 23(2–3): 89–114.
- Liu, G., Liao, S., Zhu, D., Liu, L., Cheng, D., and Zhou, H. (2011). Photodegradation of Aniline by Goethite Doped with Boron Under Ultraviolet and Visible Light Irradiation. *Materials Research Bulletin*. 46(8): 1290–1295.
- Liu, T.-X., Li, X.-M., Li, F.-B., Zhang, W., Chen, M.-J., and Zhou, S.-G. (2011). Reduction of Iron Oxides by *Klebsiella pneumoniae* L17: Kinetics and Surface Properties. *Colloids and Surfaces A: Physicochemical and Engineering Aspects*. 379(1–3): 143–150
- Lu, M.-C. (2000a): Oxidation of Chlorophenols with Hydrogen Peroxide in the Presence of Goethite, *Chemosphere*. 40. 125–130.
- Lu, M.-C., Chen, J.-N., and Huang, H.-H. (2002b). Role of Goethite Dissolution in the Oxidation of 2-Chlorophenol with Hydrogen Peroxide, *Chemosphere*. 46: 131–136.
- Maarof, H. I., Hameed, B. H., and Ahmad, A. L. (2004). Single and Binary Adsorption of Phenol and 3-Chlorophenol onto Granular Activated Carbon.
- Maji, S. K., Sreejith, S., Mandal, A. K., Dutta, A. K., and Zhao, Y. (2014). Synthesis of Ag₂S Quantum Dots by a Single-Source Precursor: An Efficient Electrode Material for Rapid Detection of Phenol. *Analytical Methods*. 6: 2059–2065.
- Mangrulkar, P. A., Kamble, S. P., Meshram, J., and Rayalu, S. S. (2008). Adsorption of Phenol and *o*-Chlorophenol by Mesoporous MCM-41. *Journal of Hazardous Materials*. 160: 414–421.
- Martinez, L., Leinen, D., Martin, F., Gabas, M., Ramos-Barrado, J. R., and Quagliata, E. (2007). Electrochemical Growth of Diverse Iron Oxide (Fe₃O₄, alpha-FeOOH, and gamma-FeOOH) Thin Films by Electrodeposition Potential Tuning. *Journal of The Electrochemical Society*. 154(3): D126–D133.
- Mastalir, Á., Király, Z., Szöllösi, G., Bartók, M. (2001). Stereoselective Hydrogenation of 1-Phenyl-1-Pentyne over Low-Loaded Pd-Montmorillonite Catalysts. *Applied Catalysis A: General*. 213: 133–140

- Maugans, C. B. and Akgerman, A. (2003). Catalytic Wet Oxidation of Phenol in a Trickle Bed Reactor over a Pt/TiO₂ Catalyst. *Water Research*. 37(2): 319–328
- McCullagh, C., Skillen, N., Adams, M., and Robertson, P. K. J. (2011). Photocatalytic Reactors for Environmental Remediation: A Review. *Journal of Chemical Technology & Biotechnology*. 86(8): 1002–1017.
- Metz D. H., Meyer M., Dotson A., Beerendonk E., Dionysiou D. D. (2011). The Effect of UV/H₂O₂ Treatment on Disinfection By-Product Formation Potential Under Simulated Distribution System Conditions, *Water Resource*. 45: 3969–3980.
- Mohapatra, P., Samantaray, S. K. and Parida, K. (2005). Photocatalytic Reduction of Hexavalent Chromium in Aqueous Solution over Sulphate Modified Titania. *Journal of Photochemistry and Photobiology A: Chemistry*. 170(2): 189–194.
- Moza, S., Bubacz, K., Janus, M., Morawski, A. W. (2012). Decomposition of 3-Chlorophenol on Nitrogen Modified TiO₂ Photocatalysts. *Journal of Hazardous Materials*. 203: 128–136.
- Muller, F. and Caillard, L. (2011). *Chlorophenols*. Ullmann's Encyclopedia of Industrial Chemistry. John Wiley & Sons, Inc.
- Munoz M., Pedro Z. M., Casas J. A., Rodriguez, J. J., Assessment of the Generation of Chlorinated Byproducts upon Fenton-Like Oxidation of Chlorophenols at Different Conditions. *Journal of Hazardous Material*. 190: 993–1000.
- Nie, Y., Hu, C., Qu, J., and Zhao, X. (2009). Photoassisted Degradation of Endocrine Disruptors over CuOx-FeOOH with H₂O₂ at Neutral pH. *Applied Catalysis B: Environmental*. 87(1–2): 30–36.
- Nikoobakht, B., and El-Sayed, M. A. (2001). Evidence for Bilayer Assembly of Cationic Surfactants on the Surface of Gold Nanorods. *Langmuir*. 17(20): 6368–6374.
- Nuñez, N. O., Tartaj, P., Morales, M. P., Gonzalez-Carreño, T., and Serna, C. J. (2006). Correlation Between Microstructural Features and Magnetic Behavior of Fe-Based Metallic Nanoneedles. *Acta Materialia*. 54(1): 219–224.
- Ollis, D. F. (1985). Contaminant Degradation in Water, Heterogeneous Photocatalysis Degrades Halogenated Hydrocarbon Contaminants. *Environmental Science and Technology*. 19(6): 480–84.

- Ortiz de la Plata, G. B., Alfano, O. M., and Cassano, A. E. (2008a). Optical Properties of Goethite Catalyst for Heterogeneous Photo-Fenton Reactions: Comparison with a Titanium Dioxide Catalyst. *Chemical Engineering Journal*. 137(2): 396–410.
- Ortiz de la Plata, G. B., Alfano, O. M., and Cassano, A. E. (2010b). Decomposition of 2-Chlorophenol Employing Goethite as Fenton Catalyst. I. Proposal of a Feasible, Combined Reaction Scheme of Heterogeneous and Homogeneous Reactions. *Applied Catalysis B: Environmental*. 95(1–2): 1–13.
- Ortiz de la Plata, G. B., Alfano, O. M., and Cassano, A. E. (2010c). Decomposition of 2-Chlorophenol Employing Goethite as Fenton Catalyst II: Reaction Kinetics of the Heterogeneous Fenton and photo-Fenton Mechanisms. *Applied Catalysis B: Environmental*. 95(1–2): 14–25.
- Ortiz de la Plata, G. B., Alfano, O. M., and Cassano, A. E. (2010d). The Heterogeneous Photo-Fenton Reaction Using Goethite As Catalyst. *Water Science and Technology*. 258: 3019–3116.
- Palma, R. D., Peeters, S., Van Bael, M. J., den Rul, H. V., Bonroy, K., Laureyn, W., Mullens, J., Borghs, G., and Maes, G. (2007). Silane Ligand Exchange to Make Hydrophobic Superparamagnetic Nanoparticles Water-Dispersible. *Chemistry of Materials*. 19: 1821–1831.
- Park, J., Joo, J., Soon, G. K., Jang, Y., and Hyeon, T. (2007). Synthesis of Monodisperse Spherical Nanocrystals. *Angewandte Chemie-International Edition*. 46(25): 4630–4660.
- Pavia, D. L., Lampman, G. M., and Kriz, G. S. (2001). *Introduction to spectroscopy: a guide for students of organic chemistry*. Fort Worth, Tex: Harcourt College Publishers.
- Pera-Titus, M., García-Molina, V., Baños, M. A., Giménez, J., and Esplugas, S. (2004). Degradation of Chlorophenols by Means of Advanced Oxidation Processes: A General Review. *Applied Catalysis B: Environmental*. 47(4): 219–256.
- Pereira, J. H. O. S., Vilar, V. J. P., Borges, M. T., González, O., Esplugas, S., and Boaventura, R. A. R. (2011). Photocatalytic Degradation of Oxytetracycline using TiO₂ Under Natural and Simulated Solar Radiation. *Solar Energy*. 85(11): 2732–2740.

- Pérez–Moya, M., Graells, M., del Valle, L. J., Centelles, E., and Mansilla, H. D. (2007). Fenton and Photo–Fenton Degradation of 2–Chlorophenol: Multivariate Analysis and Toxicity Monitoring. *Catalysis Today*. 124(3–4): 163–171.
- Peter, O. I., Chidi, O., and Iheanacho, M. A. (2012). The Preparation and Application of Environmentally Benign Titanium Pillared Clay Catalyst for Esterification of Ethanol and Acetic Acid. *American Chemical Science Journal*. 2: 45–59.
- Peulon, S., Baraize, Q., and Chaussé, A. (2007). Iron Compounds Electrodeposited Onto a Transparent Semiconductor: Synthesis and Characterisation by UV–Vis Spectroscopy. *Electrochimica Acta*. 52: 7681–7688.
- Poerschmann, J., Trommler, U., Górecki, T., and Kopinke, F.–D. (2009). Formation of Chlorinated Biphenyls, Diphenyl Ethers and Benzofurans as a Result of Fenton–Driven Oxidation of 2–Chlorophenol. *Chemosphere*. 75(6): 772–780.
- Porta, F., Prati, L., Rossi, M., and Scar, G. (2002). Synthesis of Au(0) Nanoparticles from W/O Microemulsions. *Colloids and Surfaces A: Physicochemical and Engineering Aspects*. 211: 43–48.
- Poulopoulos, S. G., Nikolaki, M., Karampetsos, D., and Philippopoulos, C. J. (2008). Photochemical Treatment of 2–Chlorophenol Aqueous Solutions Using Ultraviolet Radiation, Hydrogen Peroxide and Photo–Fenton Reaction. *Journal of Hazardous Material*. 153(1–2): 582–587.
- Prasad, P. S. R., Shiva Prasad, K., Krishna Chaitanya, V., Babu, E. V. S. S. K., Sreedhar, B., and Ramana Murthy, S. (2006). In Situ FTIR Study on the Dehydration of Natural Goethite. *Journal of Asian Earth Sciences*. 27(4): 503–511.
- Prélot, B., Villieras, F., Pelletier, M., Gérard, G., Gaboriaud, F., and Ehrhardt, J.–J.(2003). Morphology and Surface Heterogeneities in Synthetic Goethites. *Journal of Colloid and Interface Science*. 261(2): 244–254
- Proverbio, Z. E., Messina, P. V., Ruso, J., Prieto, G., Schulz, P. C., Sarmiento, F., and Argent, J. (2006). Aggregation in Dodecyltrimethylammonium Bromide–Didodecyldimethylammonium Bromide Aqueous Mixtures. *Chemical Society*. 94(4–6): 19–30.
- Padhi, D.K., Parida, K. (2014). Facile Fabrication of α -FeOOH Nanorod/RGO Composite: A Robust Photocatalyst for Reduction of Cr(VI) Under Visible Light Irradiation. *Journal of Materials Chemistry A*. 2:10300–10312.

- Puangpetch, T., Sreethawong, T., and Chavadej, S. (2010). Hydrogen Production Over Metal-Loaded Mesoporous-Assembled SrTiO₃ Nanocrystal Photocatalysts: Effects of Metal Type and Loading. *International Journal of Hydrogen Energy*. 35(13): 6531–6540.
- Rădițoiu, V., Diamandescu, L., Corobea, M. C., Rădițoiu, A., Popescu-Pogrion, N., and Nicolae, C. A. (2012). A Facile Hydrothermal Route for the Synthesis of α -FeOOH with Controlled Morphology. *Journal of Crystal Growth*. 348(1): 40–46.
- Rashid, J., Barakat, M. A., Salah, N., and Habib, S. S. (2015). ZnO-Nanoparticles Thin Films Synthesized by RF Sputtering for Photocatalytic Degradation of 2-Chlorophenol in Synthetic Wastewater. *Journal of Industrial and Engineering Chemistry*. 23: 134–139.
- Rieger, P. (1998). *Electron Spin Resonance*, Brown University.
- Ristić, M., Musić, S., and Godec, M. (2006). Properties of γ -FeOOH, α -FeOOH and α -Fe₂O₃ Particles Precipitated by Hydrolysis of Fe³⁺ Ions in Perchlorate Containing Aqueous Solutions. *Journal of Alloys and Compounds*. 417(1–2): 292–299
- Santana, M. C.; Ferrera, S. Z.; Padrón, E. T. M.; and Rodríguez, J. S. J. (2009). Methodologies for the Extraction of Phenolic Compounds from Environmental Samples: New Approaches. *Molecules*. 14: 298–320.
- Sapawe, N., Jalil, A. A., Triwahyono, S., Adam, S. H., Jaafar, N. F., and Satar, M. A. H. (2012). Isomorphous Substitution of Zr in the Framework of Aluminosilicate HY by an Electrochemical Method: Evaluation by Methylene Blue Decolorization. *Applied Catalysis B: Environmental*. 125: 311–323.
- Sato, H., Ohtsu, T., Komasaawa, I. (2002). Preparation of Ultrafine Palladium Particles in Reverse Micelles and Application for Hydrogenation Catalysts. *Journal of chemical engineering of Japan*. 35(3): 255–262.
- Schellin, M., and Popp, P. (2005). Membrane-Assisted Solvent Extraction of Seven Phenols Combined with Large Volume Injection–Gas Chromatography–Mass Spectrometric Detection. *Journal of Chromatography A*. 1072(1): 37–43.
- Scherrer, P. (1981). Bestimmung der Grösse und der inneren Struktur von Kolloidteilchen mittels Röntgenstrahlen. *Nachrichten von der Gesellschaft der Wissenschaften zu Göttingen*. 26: 98–100.

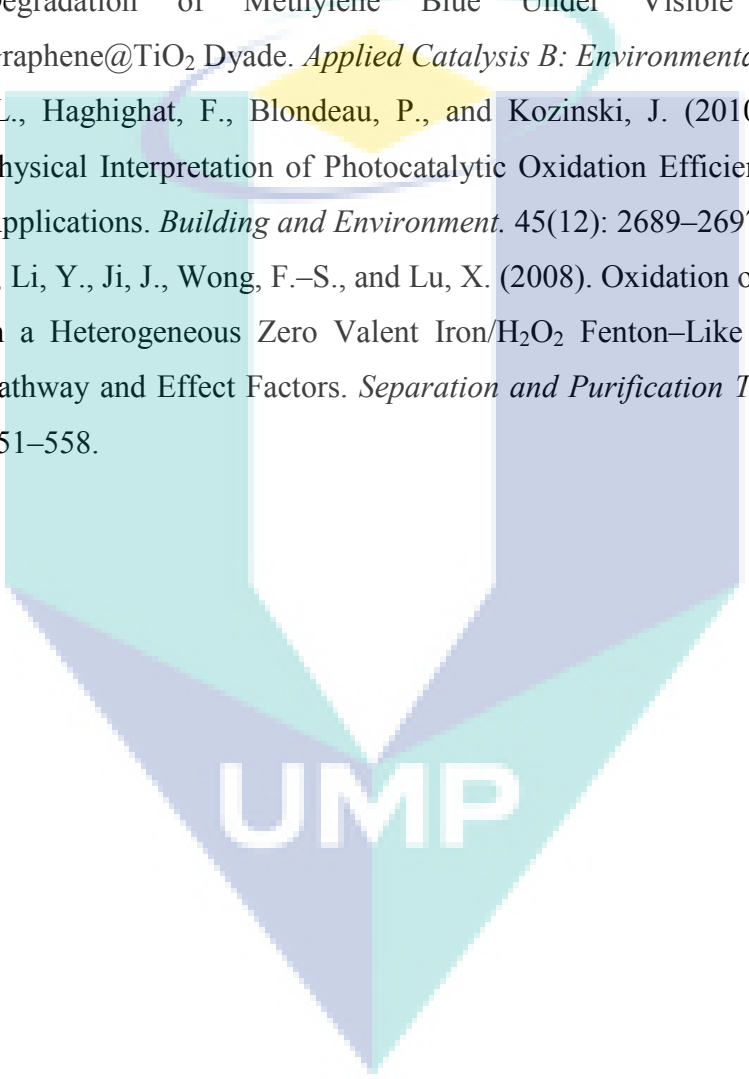
- Sen, R. K. and Swaminathan, T. (2004). Response Surface Modeling and Optimization to Elucidate and Analyze the Effects of Inoculum Age and Size on Surfactin Production. *Biochemical Engineering Journal*. 21: 141–148.
- Sepúlveda–Guzmán, S., Pérez–Camacho, O., Rodríguez–Fernández, O., and García–Zamora, M. (2005). In Situ Preparation of Magnetic Nanocomposites of Goethite in a Styrene–Maleimide Copolymer Template. *Journal of Magnetism and Magnetic Materials*. 294(2): 47–50.
- Setiabudi, H. D., Jalil, A. A., Triwahyono, S., Kamarudin, N. H. N., and Mukti, R. R. (2012). IR Study of Iridium Bonded to Perturbed Silanol Groups of Pt–HZSM5 for *n*–pentane Isomerization. *Applied Catalysis A: General*. 417: 190–199.
- Shao, M.–W., Ban, H.–Z., Tong, Y.–H., Hu, H., Niu, L.–L., and Gao, H.–Z. (2007). Synthesis of Single–Crystalline alpha–FeOOH Nanorods with Semi–Hard Magnetic Property. *Materials Letters*. 61(21): 4318–4320.
- Sheydaei, M., Aber, S. and Khataee, A. (2014). Preparation of a Novel γ –FeOOH–GAC Nano Composite for Decolorization of Textile Wastewater by Photo Fenton–like Process in a Continuous Reactor. *Journal of Molecular Catalysis A: Chemical Volume*. 392: 229–234.
- Shinde, S. S., Bhosale, C. H., and Rajpure, K. Y. (2011). Photocatalytic Oxidation of Salicylic Acid and 4–Chlorophenol in Aqueous Solutions Mediated by Modified AlFe₂O₃ Catalyst Under Sunlight. *Journal of Molecular Catalysis A: Chemical*. 347(1–2): 65–72.
- Simonsen, M. E., Sønderby, C., Li, Z., and Søgaard, E. G. (2009). XPS and FT–IR Investigation of Silicate Polymers. *Journal of Materials Science*. 44: 2079–2088.
- Singh, S. B., and Kulshrestha, G. (1997). Gas Chromatographic Analysis of Polychlorinated Dibenzo–P–Dioxins and Dibenzofurans. *Journal of Chromatography A*. 774(1–2): 97–109.
- Sleiman, M., Vildoza, D., Ferronato, C., and Chovelon, J.–M. (2007). Photocatalytic Degradation of Azo Dye Metanil Yellow: Optimization and Kinetic Modeling using a Chemometric Approach. *Applied Catalysis B: Environmental*. 77(1–2): 1–11.
- Song, L. and Zhang, S. (2009). Formation of α –Fe₂O₃/FeOOH Nanostructures with Various Morphologies by a Hydrothermal Route and Their Photocatalytic

- Properties. *Colloids and Surfaces A: Physicochemical and Engineering Aspects*. 348(1–3): 217–220.
- Srivastava, R., Fujita, S., and Arai, M. (2009). Synthesis and Adsorption Properties of Smectite-Like Materials Prepared using Ionic Liquids. *Applied Clay Science*. 43(1): 1–8.
- Sultan, S., and Tikoo, P. K. (1984). Hardness and Structure of Nickel Electrodeposited from a Nickel Acetate–N,N–Dimethylformamide–Water Bath. *Surface Technology*. 21(3): 239–244.
- Sun, J–H., Sun, S–P., Wang, G–L., and Qiao, L–P. (2007). Degradation of Azo Dye Amido Black 10B in Aqueous Solution by Fenton Oxidation Process. *Dyes and Pigments*. 74(3): 647–652.
- Taleb, M. F. A. (2014). Adsorption and Photocatalytic Degradation of 2-CP in Wastewater onto CS/CoFe₂O₄ Nanocomposite Synthesized using Gamma Radiation. *Carbohydrate Polymers*. 114: 65–72.
- Taranto, J., Frochet, D., and Pichat, P. (2007). Modeling and Optimizing Irradiance on Planar, Folded, and Honeycomb Shapes to Maximize Photocatalytic Air Purification. *Catalysis Today*. 122(1–2): 66–77.
- Tauc, J., Grigorovici, R., and Vancu, A. (1966). Optical Properties and Electronic Structure of Amorphous Germanium. *physica status solidi (b)*. 15(2): 627–637.
- Thomas, J. K. (1990). The Structure, Dynamic and Equilibrium Properties of Colloidal Systems. *Kluwer Dordrecht*. 759.
- Thomas, O. and Burgess, C. (2007). *UV–Visible Spectrophotometry of Water and Wastewater*: Amsterdam; Boston: Elsevier.
- Tokuda, M., Mimura, N., Karasawa, T., Fujita, H., and Suginome, H. (1993). The Effect of the Composition of Tri-Elemental Doping (K, Al, S) on the Photocatalytic Performance of Synthesized TiO₂ Nanoparticles in Oxidizing 2-Chlorophenol over Visible Light Illumination. *Applied Catalysis A: General*. 401(1–2): 233–238.
- Tolosa, N. C., Lu, M–C, Mendoza, H. D., and Rollon, A. P. (2011). New Preparation of Reactive Zinc Metal by Electrolysis and Its Use for a Facile Isoprenylation of Aldehydes and Ketones. *Tetrahedron Letters*. 34(47): 7607–7610.
- Tseng, R.–L., Wu, K.–T., Wu, F.–C., and Juang, R.–S. (2010). Kinetic Studies on the Adsorption of Phenol, 4–Chlorophenol, and 2,4–Dichlorophenol from Water

- Using Activated Carbons. *Journal of Environmental Management*. 91(11): 2208–2214.
- Ueno, K., Tokuda, H., and Watanabe, M. (2010). Ionicity in Ionic Liquids: Correlation with Ionic Structure and Physicochemical Properties. *Physical Chemistry Chemical Physics*. 12(8): 1649–1658.
- Ursachi, I., Stancu, A., and Vasile, A. (2012). Magnetic α -Fe₂O₃/MCM-41 Nanocomposites: Preparation, Characterization, and Catalytic Activity for Methylene Blue Degradation. *Journal of Colloid and Interface Science*. 377(1): 184–190.
- Vollmer, C., and Janiak, C. (2011). Naked Metal Nanoparticles from Metal Carbonyls in Ionic Liquids: Easy Synthesis and Stabilization. *Coordination Chemistry Reviews*. 255(17–18): 2039–2057
- Vollmer, C., Redel, E., Abu-Shandi, K., Thomann, R., Manyar, H., and Hardacre, C. (2010). Microwave Irradiation for the Facile Synthesis Of Transition-Metal Nanoparticles (NPs) in Ionic Liquids (ILs) from Metal-Carbonyl Precursors and Ru-, Rh-, and Ir-NP/IL Dispersions as Biphasic Liquid-Liquid Hydrogenation Nanocatalysts for Cyclohexene. *Chemistry – A European Journal*. 16(12): 3849–3858.
- Wang, Y., Deng, K., and Zhang, L. (2011a). Visible Light Photocatalysis of BiOI and Its Photocatalytic Activity Enhancement by In Situ Ionic Liquid Modification. *Journal of Physical Chemistry C*. 115(29): 14300–14308.
- Wang, C, Liu, H., Sun, Z., Huang, J., Liao, Y. (2012b). Supported Nanosized α -FeOOH Improves Efficiency of Photoelectro-Fenton Process with Reaction-Controlled pH Adjustment for Sustainable Water Treatment. *International Journal of Photoenergy*. 2012: 689807.
- Wei, M., Tian, D., Liu, S., Zheng, X., Duan, S., and Zhou, C. (2014). β -Cyclodextrin functionalized graphene material: A Novel Electrochemical Sensor for Simultaneous Determination of 2-Chlorophenol and 3-Chlorophenol. *Sensors and Actuators B: Chemical*. 195: 452–458.
- Wu, H., Dou, X., Deng, D., Guan, Y., Zhang, L., and He, G. (2011). Decolourization of the Azo Dye Orange G In Aqueous Solution via a Heterogeneous Fenton-Like Reaction Catalysed by Goethite. *Environmental Technology*. 1–8.

- Xia, M., Chen, C., Long, M., Chen, C., Cai, W., and Zhou, B. (2011). Magnetically Separable Mesoporous Silica Nanocomposite and Its Application In Fenton Catalysis. *Microporous and Mesoporous Materials*. 145(1–3): 217–223.
- Xu, B., Gao, N–Y., Cheng, H., Xia, S–J., Rui, M., and Zhao, D–D. (2009). Oxidative Degradation of Dimethyl Phthalate (DMP) by UV/H₂O₂ Process. *Journal of Hazardous Materials*. 162(2–3): 954–959.
- Xu, H–Y., Prasad, M., and Liu, Y. (2009). A Novel Catalyst in Mineral–Catalyzed Fenton–Like System for Dyeing Wastewater Discoloration. *Journal of Hazardous Materials*. 165(1–3): 1186–1192.
- Xue, Z., Ma, J., Hao, W., Bai, X., Kang, Y., Liu, J., and Li, R. (2012). Synthesis and Characterization of Ordered Mesoporous Zeolite LTA with High Ion Exchange Ability. *Journal of Material Chemistry*. 22: 2532–2538.
- Ye, F–X. And Shen, D–S. (2004). Acclimation of Anaerobic Sludge Degrading Chlorophenols and the Biodegradation Kinetics During Acclimation Period. *Chemosphere*. 54(10): 1573–1580.
- Yoneyama, H., Haga, S., and Yamanaka, S. (1989). Photocatalytic Activities of Microcrystalline Titania Incorporated In Sheet Silicates of Clay. *The Journal of Physical Chemistry*. 93(12): 4833–4837.
- Yoshikawa, N., Kimura, T., and Kawase, Y. (2003). Oxidative Degradation of Nonionic Surfactants with TiO₂ Photocatalyst in a Bubble Column Reactor. *The Canadian Journal of Chemical Engineering*. 81(3–4): 719–724.
- Zanjanchi, M. A., Golmojdeh, H., and Arvand, M. (2009a). Enhanced Adsorptive and Photocatalytic Achievements in Removal of Methylene Blue by Incorporating Tungstophosphoric Acid–TiO₂ into MCM–4. *Journal of Hazardous Materials*. 169(1–3): 233–239.
- Zanjanchi, M. A., Ebrahimian, A., and Arvand, M. (2010b). Sulphonated Cobalt Phthalocyanine–MCM–41: An Active Photocatalyst for Degradation of 2,4–Dichlorophenol. *Journal of Hazardous Materials*. 175(1–3): 992–1000.
- Zarei, M., Khataee, A. R., Ordikhani–Seyedlar, R., and Fathinia, M. (2010). Photoelectro–Fenton Combined with Photocatalytic Process for Degradation of an Azo Dye using Supported TiO₂ Nanoparticles and Carbon Nanotube Cathode: Neural Network Modeling. *Electrochimica Acta*. 55(24): 7259–7265.

- Zhang, H., Fu, H., and Zhang, D. (2009a). Degradation of C.I. Acid Orange 7 by Ultrasound Enhanced Heterogeneous Fenton-Like Process. *Journal of Hazardous Materials*. 172(2–3): 654–660.
- Zhang, J., Li, X., Rosenholm, J. M., and Gu, H-C. (2011b). Synthesis and Characterization of Pore Size-Tunable Magnetic Mesoporous Silica Nanoparticles. *Journal of Colloid and Interface Science*. 361(1): 16–24.
- Zhao, D., Sheng, G., Chen, C., Wang, X. (2012). Enhanced Photocatalytic Degradation of Methylene Blue Under Visible Irradiation on Graphene@TiO₂ Dyade. *Applied Catalysis B: Environmental*. 111: 303–308.
- Zhong, L., Haghghat, F., Blondeau, P., and Kozinski, J. (2010). Modeling and Physical Interpretation of Photocatalytic Oxidation Efficiency in Indoor Air Applications. *Building and Environment*. 45(12): 2689–2697.
- Zhou, T., Li, Y., Ji, J., Wong, F.-S., and Lu, X. (2008). Oxidation of 4-Chlorophenol in a Heterogeneous Zero Valent Iron/H₂O₂ Fenton-Like System: Kinetic, Pathway and Effect Factors. *Separation and Purification Technology*. 62(3): 551–558.

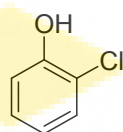
The logo for UMP (Université de Montpellier) is a large, stylized shield shape composed of several overlapping triangles in shades of teal and light blue. The letters 'UMP' are prominently displayed in white, bold, sans-serif font across the center of the shield.

UMP

APPENDIX A

The properties of 2-CP (Muller and Caillard, 2011)

2-CHLOROPHENOL



2-chlorophenol

Other name	ortho-chlorophenol, 2-Hydroxychlorobenzene,
Properties	
Molecular formula	C ₆ H ₅ ClO
Molar mass, g mol ⁻¹	128.56
Density, g cm ⁻³	1.2634
Melting point, °C	9.4
Boiling point, °C	174.9

UMP

APPENDIX B

Calculations of electrolysis time run for wt% loading

By taking the amount of MSN support as 1.5 g and 10 wt% desired amount of α -FeOOH, the calculations were made as follows:

Mass of α -FeOOH required,

$$10 \text{ wt}\% \alpha\text{-FeOOH} = \frac{x \text{ g Fe}}{1.5 \text{ g MSN} + x \text{ g Fe}}$$

$$x \text{ g Fe} = 0.1667 \text{ g}$$

Since molecular weight for Fe is $55.845 \text{ g mol}^{-1}$, the mol of Fe needed is calculated;

$$\text{Mol of Fe} = \frac{0.1667 \text{ g}}{55.845 \text{ g mol}^{-1}} \times 1000$$

$$= 2.985 \text{ mmol}$$

Electrolysis time run needed using 480 mA current density, with $F = 96,486 \text{ C mol}^{-1} = 96,486 \text{ A s mol}^{-1}$

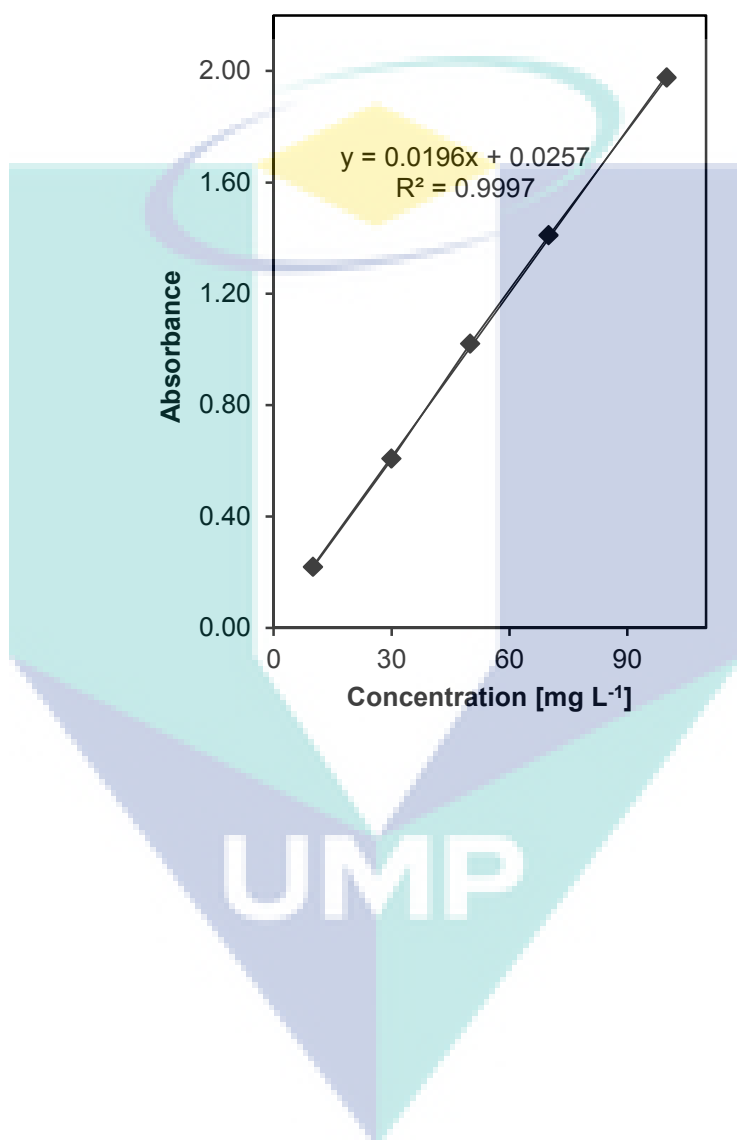
$$t = \left(\frac{F}{I} \right) (z \times n)$$

$$= \left(\frac{96486 \text{ A s mol}^{-1}}{480 \text{ mA}} \right) (3 \times 2.985 \text{ mmol})$$

$$= 1800 \text{ s}$$

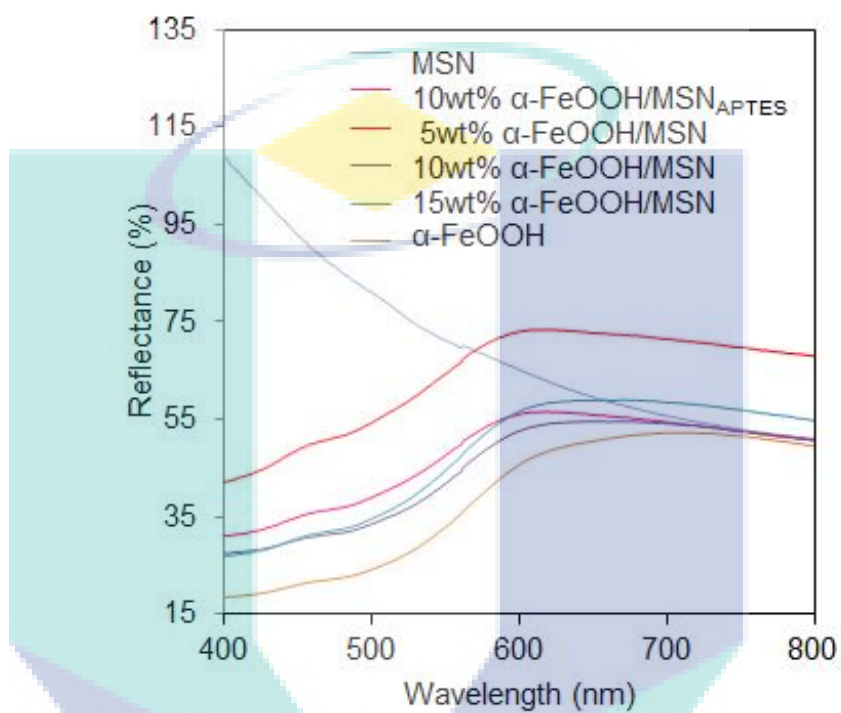
APPENDIX C

Standard calibration of 2-chlorophenol



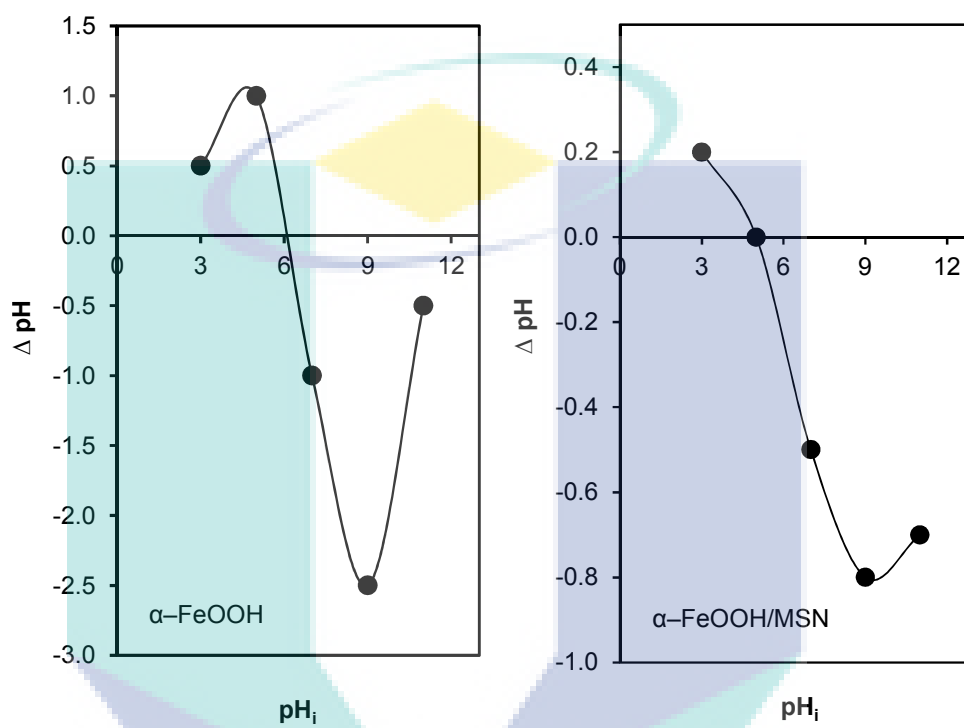
APPENDIX D

UV-vis reflectance spectrum of catalysts



UMP

APPENDIX E

The isoelectric points (pH_{PZC}) of photocatalysts

UMP

APPENDIX F
Calculation of ANOVA table

The analysis of variance (ANOVA) of regression parameters was calculated following the presented table as below:

Source	Sum of squares	Degree of freedom	Mean square	F-value
Regression	SSR	$p-1$	$SSR/(p-1)$	$[SSR/(p-1)] / [SSE/(N-p)]$
Residual	SSE	$N-p$	$SSE/(N-p)$	
Total	SST	$N-1$		

* $F(df_1, df_2, \alpha)$

* SSR = Sum of squares regression

* SSE = Sum of squares error (residual)

* SST = Sum of squares total

* p = Number of parameter

* N = Number of run

The model F -value obtained was compared to value from F -table to indicate the model was significant or not. For example, the obtained value $F = 50.34$ was exceeded the table value $F_{(14,11,0.05)} = 2.72$, demonstrated that the experimental results were fitted well and model was significant.

APPENDIX G

F-table

F Table for $\alpha = 0.05$																			
/	df ₁ =1	2	3	4	5	6	7	8	9	10	12	15	20	24	30	40	60	120	∞
df ₂ =1	161.4476	199.5000	215.7073	224.5832	230.1619	233.9860	236.7684	238.8827	240.5433	241.8817	243.9060	245.9499	248.0131	249.0518	250.0931	251.1432	252.1957	253.2529	254.3144
2	18.512	19.000	19.164	19.246	19.296	19.329	19.353	19.371	19.384	19.395	19.412	19.429	19.445	19.454	19.462	19.470	19.479	19.487	19.495
3	10.120	9.5521	9.2766	9.1172	9.0135	8.9406	8.8867	8.8452	8.8123	8.7855	8.7446	8.7029	8.6602	8.6385	8.6166	8.5944	8.5720	8.5494	8.5264
4	7.7086	6.9443	6.5914	6.3882	6.2561	6.1631	6.0942	6.0410	5.9988	5.9644	5.9117	5.8578	5.8025	5.7744	5.7459	5.7170	5.6877	5.6581	5.6281
5	6.6079	5.7861	5.4095	5.1922	5.0503	4.9503	4.8759	4.8183	4.7725	4.7351	4.6777	4.6188	4.5581	4.5272	4.4957	4.4638	4.4314	4.3985	4.3650
6	5.9874	5.1433	4.7571	4.5337	4.3874	4.2839	4.2067	4.1468	4.0990	4.0600	3.9999	3.9381	3.8742	3.8415	3.8082	3.7743	3.7398	3.7047	3.6689
7	5.5914	4.7374	4.3468	4.1203	3.9715	3.8660	3.7870	3.7257	3.6767	3.6365	3.5747	3.5107	3.4445	3.4105	3.3738	3.3404	3.3043	3.2674	3.2298
8	5.3177	4.4590	4.0662	3.8379	3.6875	3.5806	3.5005	3.4381	3.3881	3.3472	3.2839	3.2184	3.1503	3.1152	3.0794	3.0428	3.0053	2.9669	2.9276
9	5.1174	4.2565	3.8625	3.6331	3.4817	3.3738	3.2927	3.2296	3.1789	3.1373	3.0729	3.0061	2.9365	2.9005	2.8637	2.8259	2.7872	2.7475	2.7067
10	4.9646	4.1028	3.7083	3.4780	3.3258	3.2172	3.1355	3.0717	3.0204	2.9782	2.9130	2.8450	2.7740	2.7372	2.6996	2.6609	2.6211	2.5801	2.5379
11	4.8443	3.9823	3.5874	3.3567	3.2039	3.0946	3.0123	2.9480	2.8962	2.8536	2.7876	2.7186	2.6464	2.6090	2.5705	2.5309	2.4901	2.4480	2.4045
12	4.7472	3.8853	3.4903	3.2592	3.1059	2.9961	2.9134	2.8486	2.7964	2.7534	2.6866	2.6169	2.5436	2.5055	2.4663	2.4259	2.3842	2.3410	2.2962
13	4.6672	3.8056	3.4105	3.1791	3.0254	2.9153	2.8321	2.7669	2.7144	2.6710	2.6037	2.5331	2.4589	2.4202	2.3803	2.3392	2.2966	2.2524	2.2064
14	4.6001	3.7389	3.3439	3.1122	2.9582	2.8477	2.7642	2.6987	2.6458	2.6022	2.5342	2.4630	2.3879	2.3487	2.3082	2.2664	2.2229	2.1778	2.1307
15	4.5431	3.6823	3.2874	3.0556	2.9013	2.7905	2.7066	2.6408	2.5876	2.5437	2.4753	2.4034	2.3275	2.2878	2.2468	2.2043	2.1601	2.1141	2.0658
16	4.4940	3.6337	3.2389	3.0069	2.8524	2.7413	2.6572	2.5911	2.5377	2.4935	2.4247	2.3522	2.2756	2.2354	2.1938	2.1507	2.1058	2.0589	2.0096
17	4.4513	3.5915	3.1968	2.9647	2.8100	2.6987	2.6143	2.5480	2.4943	2.4499	2.3807	2.3077	2.2304	2.1898	2.1477	2.1040	2.0584	2.0107	1.9604
18	4.4139	3.5546	3.1599	2.9277	2.7729	2.6613	2.5767	2.5102	2.4563	2.4117	2.3421	2.2686	2.1906	2.1497	2.1071	2.0629	2.0166	1.9681	1.9168
19	4.3807	3.5219	3.1274	2.8951	2.7401	2.6283	2.5435	2.4768	2.4227	2.3779	2.3080	2.2341	2.1555	2.1141	2.0712	2.0264	1.9795	1.9302	1.8780
20	4.3512	3.4928	3.0984	2.8661	2.7109	2.5990	2.5140	2.4471	2.3928	2.3479	2.2776	2.2033	2.1242	2.0825	2.0391	1.9938	1.9464	1.8963	1.8432

